Dissertation zur Erlangung des Doktorgrades
der Fakultät für Chemie und Pharmazie
der Ludwig-Maximilians-Universität München

Coupling of Emitters to Surface Plasmons Investigated by Back Focal Plane Microscopy

von
Nicolai Friedrich Hartmann
aus
München

2013

Erklärung

Diese Dissertation wurde im Sinne von § 7 der Promotionsordnung vom 28. November 2011 von Herrn Prof. Dr. Achim Hartschuh betreut.

Eidesstattliche Versicherung

Diese Dissertation wurde eigenständig und ohne unerlaubte Hilfe erarbeitet.

München, den 02.01.2014

(Unterschrift des Autors)

Dissertation eingereicht am 18.10.2013

1. Gutachter: Prof. Dr. Achim Hartschuh

2. Gutachter: Dr. Alexandre Bouhelier

Mündliche Prüfung am 13.12.2013

Abstract

Current efforts in the field of plasmonics towards device integration and miniaturization require detailed knowledge about the coupling between surface plasmons and emitters. In this work coupling between surface plasmon polaritons and different emitter systems has been investigated by the technique of back focal plane imaging. To develop a deeper understanding of the interaction phenomena the studies focused on single emitters in elementary plasmonic configurations that allow for an analytical description.

The first part of the thesis reports on the successful demonstration of surface plasmon polaritons launched by a single dipolar carbon nanotube emitter on a metal thin film after local optical excitation. Leakage radiation microscopy images, recorded in the back focal plane of a microscope objective, could be modeled successfully and contained the propagation length and direction of surface plasmon polaritons. Corresponding real-space images revealed plasmon propagation away from the single dipolar plasmon source. The polarization behavior of surface plasmon polaritons launched by single carbon nanotubes was found to be radial as predicted by theoretical calculations.

Remote excitation of single walled carbon nanotube excitons via propagating surface plasmons is demonstrated in the second part. A scanning aperture probe was used as source for propagating surface plasmons with fine controllability over excitation position and propagation direction. It was raster scanned in close proximity over a single carbon nanotube located on a metal film while recording the emission response from the nanotube. The carbon nanotube showed an emission response while the aperture plasmon source was still far away from the nanotube position. Theoretical modeling of the excited surface plasmon fields confirmed that the nanotube maps the surface plasmons locally with sub-diffraction resolution.

In the last part, radiation channels in the vicinity of a plasmonic nanowire were investigated. Radiation patterns of a coupled system of rare earth nanocrystals and silver nanowires in the back focal plane revealed that the emission in the vicinity of a nanowire can be approximately described by two emission channels that can be calculated analytically: Dipolar emission, also observed in the absence of the nanowire, and leakage radiation from the nanowire. The latter can be calculated using an antenna-resonator model that considers the air-dielectric interface on which the nanowire is deposited and the position of excitation along the nanowire. Fitting of the experimentally observed patterns provides estimates for the branching ratio between the two emission channels and further enable the determination of the plasmon wave-vector supported by the nanowires.

Contents

1 Introduction **1**

2 Surface plasmon polaritons (SPPs) **5**
2.1 Fundamental SPP properties . . . 5
2.2 SPP dispersion relation in different geometries . . . 8
2.2.1 Dispersion relation in a multilayer structure . . . 8
2.2.2 SPP propagation length . . . 11
2.2.3 Dispersion relation in metal cylinders . . . 12
2.3 Excitation of SPPs . . . 14
2.4 Detection of SPPs . . . 17
2.4.1 Leakage radiation . . . 17
2.4.2 Near-field Microscopy . . . 18
2.4.3 Fluorescence detection . . . 19

3 Back focal plane (BFP) imaging **21**
3.1 Theoretical description of radiation patterns in the BFP . . . 21
3.1.1 Dipolar emission characteristics in the BFP . . . 23
Calculation of intensity distribution in the BFP . . . 23
Detection efficiency of dipoles . . . 25
3.2 SPP BFP imaging . . . 27
3.2.1 SPP signatures in the BFP . . . 27
3.2.2 Calculation of BFP patterns for propagating plasmons on a noble metal nanowire . . . 28

4 Emitter Systems **31**
4.1 Single-walled carbon nanotubes (SWCNTs) . . . 31
4.1.1 Structural properties . . . 31
4.1.2 Optical properties . . . 33
4.2 Photon upconverting lanthanide doped nanoparticles . . . 35
4.2.1 Structural properties . . . 36
4.2.2 Optical properties . . . 37

5 Experimental details **41**
5.1 Microscope setup . . . 41
5.1.1 Confocal microscope . . . 41
5.1.2 BFP imaging . . . 43
5.1.3 Aperture scanning optical near-field microscopy (SNOM) configuration 44
5.2 Sample preparation and configuration . . . 45
5.2.1 SWCNTs samples on multilayer thin films . . . 45
5.2.2 Silver nanowires and rare earth nanocrystals: sample preparation . . 46

6 Launching SPPs by SWCNT emission **49**
6.1 Emission characteristics of single SWCNTs on a thin gold film 50
6.2 Theoretical simulation of single dipole BFP and real space patterns on a metal film 53
6.3 Determination of the propagation length and plasmon wave-vector from leakage radiation BFP patterns 55
6.4 Polarization resolved BFP patterns 57

7 Remote excitation of SWCNTs by propagating SPPs **61**
7.1 Excitation of SPPs with an aperture SNOM probe 62
7.2 Remote excitation of SWCNTs by SPPs excited with an aperture SNOM probe 64
7.3 Theoretical modeling of the SPP fields generated by an aperture probe on a thin metal film 66

8 Radiation channels close to a plasmonic nanowire **71**
8.1 Transmission electron microscopy (TEM) characterization of plasmonic silver NWs 72
8.2 Optical investigation of different emission channels close to a plasmonic NW 75
8.3 Theoretical description of the BFP pattern from different emission channels 77
8.3.1 Theoretical modeling of the direct NC emission pattern 77
8.3.2 Theoretical modeling of the NW leakage radiation emission pattern 77
8.4 Discussion of parameters extracted from fitting BFP patterns 83

9 Summary and outlook **87**

Bibliography **91**

Acronyms **109**

List of Figures **113**

List of Publications **117**

List of Conferences **119**

Acknowledgements **121**

1 Introduction

Since the seminal publication from Ritchie [1] in 1957, the field of plasmonics has attracted increasing interest. The study of these surface bound electromagnetic waves, existing due to charge fluctuations on a metal surface, is especially appealing due to their confined nature, which enables the concentration of energy in a small sub-diffraction volume [2,3]. At the same time the propagation of surface plasmons (SPs) along the surface allows for the transport of this energy, in an optimized case, along a distance of several hundred micrometers [4]. The properties of SPs are determined by the dielectric functions of the metal, supporting the SPs and the surrounding dielectric materials. Recent advances in both, top-down and bottom-up fabrication methods, drastically increased the range of different materials supporting SPs, enabling new device configurations and expand accessible frequency ranges [5]. In the current effort driving the field of plasmonics towards device miniaturization and realization of plasmonic based interconnects [6] detailed knowledge about the interaction between SPs and emitter systems is crucial for the design and optimization of such plasmonic applications. Additionally, new plasmonic building blocks such as noble metal nanowires become more important and enable new possibilities for applications in plasmon based logic gates [7] and quantum plasmonics [8,9].

A strong focus in the field of plasmonics is on the coupling between light and SPs. If SPs are coupling to photons the combined state is typically referred to as surface plasmon polariton (SPP). The first experimental techniques to excite and detect SPPs with light were implemented by Otto [10] and Kretschmann [11], who managed to overcome the momentum mismatch between photons and SPPs by the use of evanescent fields created in a total internal reflection geometry. Propagating SPPs can be observed via the detection of leakage radiation [12] if the supporting metal structure is thin enough so that the field component perpendicular to the surface has not completely decayed within the material. Leakage radiation from SPPs can be detected with standard optical microscopes using index-matched immersion objectives, enabling the detection of wave-vectors $\frac{k}{k_0} > 1$.

The technique of back focal plane (BFP) imaging, which was also used to determine the orientation of single molecules [13], provides a useful method to detect SPP leakage radiation angularly or wave-vector resolved in Fourier space [12,14–17]. In general, all emitting systems exhibit a unique distribution of emission in the BFP, which represents an angularly resolved intensity map. Theoretical routines for calculating the radiation pattern of single dipolar emitters, optical antennas and nanowires have been presented in the literature [13,18–20], which allow the analysis and distinction of different radiation channels

by comparison with experimentally obtained BFP patterns. Additionally, BFP imaging has been used in the past to identify SPP propagation due to the specific distribution of leakage radiation in the BFP given by the SPP wave-vector spectrum[12,21,22].

For this thesis the technique of BFP imaging, and other optical methods, were applied to study the coupling between SPPs and different emitter systems. During these investigations a key focus was on the observation of single emitters in simple configurations that are accessible by analytical descriptions. The excitation of propagating SPPs by a single dipolar source placed on a metal thin film could be shown directly by the emission features in the BFP. The angular emission characteristics of a single single-walled carbon nanotube (SWCNT) emitter located on a thin metal film were considerably reshaped in comparison to a SWCNT emitting on a glass substrate. SPP-emitter coupling could also be achieved successfully in the reversed situation shown by the remote excitation of a single dipolar SWCNT emitter on a metal film via SPPs launched from a scanning aperture probe. In an approach to apply the previously achieved results in a basic plasmonic guiding element the coupling between nanocrystal emitters and silver nanowires as confined plasmonic waveguides was investigated. Recorded characteristic BFP patterns from this coupled emitter-nanowire geometry were modeled and thus enabled access to important parameters of the plasmonic system such as the branching ratio, the SPP wave-vector or the plasmonic active length of the nanowire waveguide.

The thesis is structured as follows. After this introduction, chapter 2 discusses the fundamental properties of SPPs. Commencing from an interface between two infinite half-spaces defined by a metal and a dielectric the conditions for the existence, fundamental wave properties and the dispersion relation of SPPs are introduced. Proceeding with an investigation of SPPs in more complex thin film and metal nanowire geometries, the implications of the geometry on the dispersion relation together with connected parameters such as the SPP propagation length, are reviewed. The second part of this chapter is concerned with experimental schemes able to excite and detect SPPs on metal films and structures.

Chapter 3 gives an introduction to the specifics and applications of BFP imaging, a method to obtain an angularly resolved emission pattern. Beginning with the image formation in the BFP of a microscope objective, it continues with a theoretical description of radiation patterns from point dipole emitters in the BFP. The second part of the chapter gives two examples for the application of BFP imaging in the context of SPPs. Firstly, BFP imaging can be used to investigate SPPs on a metal film in a reflection geometry. Secondly a model is introduced, based on the theoretical model for single dipole radiation, to describe the signature in the BFP originating from SPPs propagating along a noble metal nanowire.

The different emitter systems used in this work to investigate the emitter-SPP coupling are introduced in chapter 4. First the structural and optical properties of semiconducting SWCNTs are discussed. Following the conceptual formation of SWCNTs, starting from

a single graphene sheet, a short overview of the electronic energy landscape and the resulting possible optical transitions is given. The second part deals with rare earth doped nanocrystals. After a description of different host materials lanthanide doping of a $NaYF_4$ matrix is discussed from a structural point of view. It concludes with a description of the optical processes in such rare earth doped nanocrystals with a specific focus on the photon upconversion.

Chapter 5 begins with a description of the microscope setup utilized in the experiments presented in this thesis. The optical systems including details of excitation and detection pathways in the applied microscope as well as a description of the aperture scanning near-field optical microscopy (SNOM) configuration are introduced. The second part gives insight into the specific properties and preparation of the carbon nanotube, silver nanowire and rare earth doped nanocrystal samples used in the experiments.

All experimental results are presented and discussed starting from chapter 6. In this chapter the directional excitation of propagating SPPs on a thin metal film by individual SWCNTs is investigated. Photoluminescent SWCNTs were shown to launch SPPs in the near infrared (NIR) propagating for several micrometers predominately in the direction of the nanotube axis after laser excitation in the visible. SPP excitation and propagation are investigated by leakage radiation microscopy in real-space and in the BFP. Compared to the angular emission of SWCNTs on glass, polarization resolved radiation patterns recorded for single SWCNTs on gold films reveal an almost complete redistribution of the emission with a high directivity. The claim that SPP excitation results from a radiating point dipole source could be confirmed by rigorous model calculations of spatial intensity distributions and BFP patterns.

The opposite scheme, wherein transitions in a dipolar emitter are excited via propagating SPPs is investigated in chapter 7. Light coupled into a metal coated aperture probe was chosen as a nanoscale SPPs source, which enables the fine control of the excitation position and the SPP propagation direction. First, the SPP excitation behavior of the aperture probe on a thin gold film is characterized by analysis of real space and BFP images. This analysis is followed by a scan with the aperture probe over a deposited SWCNT while simultaneously detecting the emission signal from the SWCNT, characterized as leakage radiation. The image formation is reconstructed by theoretical calculations of SPP fields created by the aperture probe in the metal film, using an established model.

Chapter 8 is concerned with the coupling between SPPs and an emitter system using noble metal nanowires (NWs) as confined SPP waveguides. Rare earth doped nanocrystals, which show upconverted photoluminescence (PL) on the anti-Stokes side of the laser excitation energy were deposited in the vicinity of plasmonic silver nanowires. With a quantitative analysis of recorded BFP patterns of this coupled system contributions of two different radiation channels could be separated: The direct dipolar emission from nanocrystals in the absence of silver nanowires and leakage radiation from excited SPPs

propagating along the nanowires. Fitting of the recorded BFP patterns with the developed two channel model gives access to important system parameters such as the channel branching ratio, the SPP wave-vector and the plasmonic active length of the nanowires. All results obtained by optical measurements were supported by a thorough transmission electron microscopy (TEM) investigation.

Finally, a summary of the most important results achieved in this thesis will be given. An included outlook will provide interesting aspects of possible future experiments regarding coupling between emitter systems and SPPs and the use of BFP imaging in different applications.

2 Surface plasmon polaritons (SPPs)

The first appearance of electromagnetic waves at surfaces in the scientific literature was in the work of Zenneck [23] and Sommerfeld [24]. They derived theoretically that these surface waves exist only at the boundary between a dielectric or a metal and a loss free dielectric. In general, electrons at a metal-dielectric interface can perform coherent fluctuations which were named surface plasma oscillations by Ritchie [1]. The first experimental observation of these surface plasmons was demonstrated by Powell and Swan [25] through fast electron loss spectroscopy of metal thin films. Soon from the fundamental ideas of concentrating light energy on length scales smaller than the wavelength together with a high sensitivity of plasmon properties for the dielectric functions of the involved media, the field of plasmonics emerged [3,26]. Surface plasmons have found their way into many applications in the fields of solar cells [27], sensors [28,29], amplification and lasers [30].
The following chapter gives an introduction to the fundamental SPP properties and continues with a closer investigation of plasmon dispersion relations in different geometries. In the end an introduction into commonly used excitation and detection schemes is given.

2.1 Fundamental SPP properties

Surface plasmons, as a wave of fluctuating surface charges, are referred to as SPP if the surface wave is coupled with propagating light [31]. Although the nomenclature is not uniform across the literature this terminology is used in the following and for the rest of the thesis, if not stated otherwise. Additionally, the term SPP is used for propagating SPPs in contrast to non propagating localized surface plasmon polaritons (LSPPs) as e.g. in metallic nanoparticles.

Propagating SPP charge fluctuations can be described by a mixed transverse and longitudinal electromagnetic field which disappears at $|z| \to \infty$ and has a maximum directly at the interface $z = 0$ (fig. 2.1) [32]. Given a propagation direction along the X-axis, the field is expressed by

$$E_{\mathrm{SPP}} = E_0^{\pm} \mathrm{e}^{\mathrm{i}(k_x x \pm k_z z - \omega t)} \tag{2.1}$$

where $+$ is used for the field reaching into the dielectric ($z \geq 0$) and $-$ for the field reaching into the metal ($z \leq 0$). Both wave-vector components k_x and k_z are assumed to be complex valued.

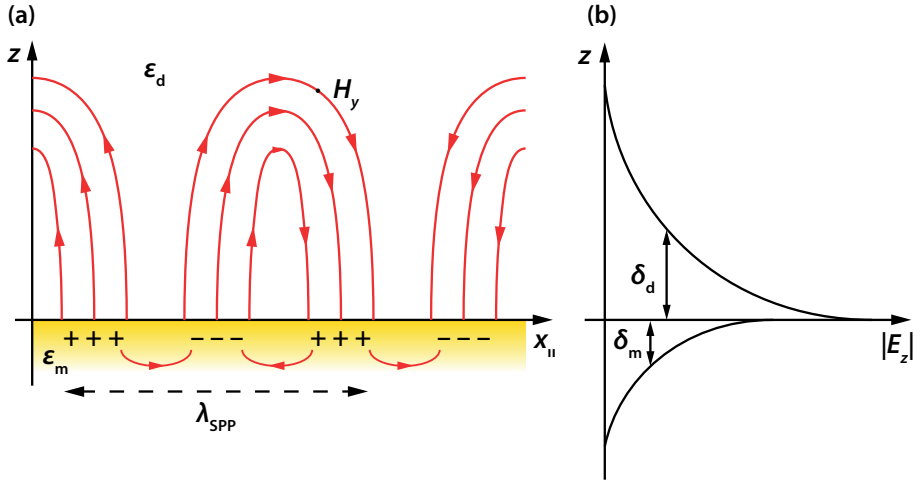

Figure 2.1: (a) Schematic of the charges and electromagnetic field lines of a SPP propagating on a metal/dielectric ($\varepsilon_\mathrm{m}/\varepsilon_\mathrm{d}$) interface along x. Additionally indicated are the magnetic field vector $\vec{H}_y$ perpendicular to the propagation direction x and the SPP wavelength λ_SPP. (b) shows the exponential dependence of the field amplitude $|E_z|$ in the direction of z into the two different media according to eq. 2.5. Adapted from [2].

After solving the Maxwell's equation for the system of a metal half-space with the complex dielectric function $\varepsilon_\mathrm{m} = \varepsilon'_\mathrm{m} + \mathrm{i}\varepsilon''_\mathrm{m}$ adjacent to a dielectric medium with a real ε_d the SPP dispersion relation can be written as

$$k_x = \frac{\omega}{c}\sqrt{\frac{\varepsilon_\mathrm{m}\varepsilon_\mathrm{d}}{\varepsilon_\mathrm{m}+\varepsilon_\mathrm{d}}}. \tag{2.2}$$

The wave-vector components normal to the propagation direction are also obtained [33]:

$$k_{j,z} = \frac{\omega}{c}\sqrt{\frac{\varepsilon_j^2}{\varepsilon_\mathrm{m}+\varepsilon_\mathrm{d}}}, \qquad j = \mathrm{d},\mathrm{m}. \tag{2.3}$$

In order to represent a propagating and surface bound wave, two conditions arise: k_z has to be purely imaginary to ensure the evanescent, surface bound character of the wave and k_x needs to contain a real part, which allows propagation. A still possible imaginary part of k_x describes the damping of the wave, due to ohmic losses in the metal [32]. Considering eq. 2.2 and eq. 2.3, these conditions are fulfilled if the sum and the product of the dielectric functions are either both positive or negative:

$$\begin{aligned} \varepsilon_\mathrm{m}(\omega)\cdot\varepsilon_\mathrm{d}(\omega) &< 0, \\ \varepsilon_\mathrm{m}(\omega)+\varepsilon_\mathrm{d}(\omega) &< 0. \end{aligned} \tag{2.4}$$

The conclusion from eq. 2.4 is, that one of the dielectric functions has to be negative with an absolute value larger than that of the other. In the case of many noble metals, having a large negative real part of the dielectric function together with a small imaginary part, adjacent to a dielectric such as glass or air, bound surface modes can exist.

Since the wave-vector components of the SPP wave perpendicular to the surface are purely imaginary the field amplitude of E_SPP decreases normal to the surface exponentially with

$-|k_{j,z}|\,|z|$. Thus the skin depth δ after which length the field is reduced to $\frac{1}{e}$ is expressed by[32]:

$$\delta_j = \frac{1}{|k_{j,z}|}, \qquad j = \mathrm{d}, \mathrm{m}. \tag{2.5}$$

This can also be examined for the two different involved media in the system:

$$\begin{aligned} \delta_\mathrm{m} &= \frac{\lambda}{2\pi}\sqrt{\frac{\varepsilon'_\mathrm{m}+\varepsilon_\mathrm{d}}{\varepsilon^2_\mathrm{m}}} \\ \delta_\mathrm{d} &= \frac{\lambda}{2\pi}\sqrt{\frac{\varepsilon'_\mathrm{m}+\varepsilon_\mathrm{d}}{\varepsilon^2_\mathrm{d}}}. \end{aligned} \tag{2.6}$$

Given the dielectric function for a noble metal and a typical dielectric it is evident, that the field reaches further into the dielectric than the metal (see also fig. 2.1 (b)). Typical penetration depths into the metal δ_m at $\lambda = 600\,nm$ are 24 nm for silver and 31 nm for gold, further decreasing with increasing wavelength[32]. The penetration depth of the field into the dielectric δ_d is on the order of half the wavelength of the incident light[2] and was experimentally observed by scanning tunneling optical microscopy (STOM)[34] (section 2.4).

Fig. 2.2 shows a typical SPP dispersion relation for a silver/air interface calculated according to eq. 2.2 using the complex dielectric function of silver from Johnson and Christy[35]. If ω values are taken to be real k_x becomes complex and the dispersion relation exhibits a back bending in the vicinity of the asymptote of the lower branch[18] before it continues in the high energy branch. The back bending has been also investigated experimentally

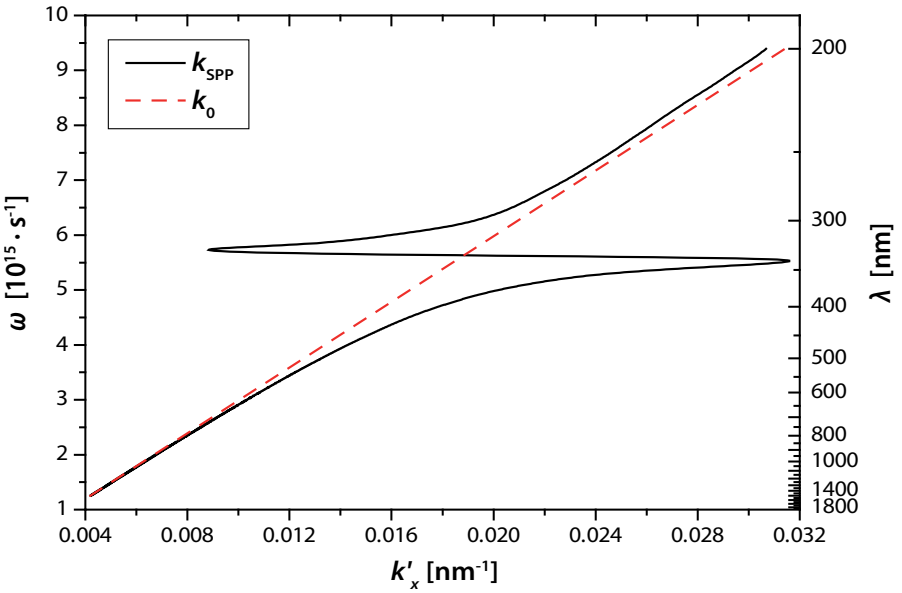

Figure 2.2: Real part of the SPP dispersion relation for a silver/air interface calculated according to eq. 2.2 (black solid line). The dashed red line represents the light line $k_0 = ck'_x$

by Arakawa et al.[36] and occurs due to strong localization of the SPP mode in the metal which is the reason for the large losses[33]. According to eq. 2.3 the high energy branch is

not considered as a surface wave since the z component of the wave-vector in the metal is no longer purely imaginary anymore. Also plotted in fig. 2.2 as red dashed line is the air dispersion, known as the light line $k_0 = ck'_x$ which asymptotically approaches the SPP dispersion relation at lower frequencies but never intersects with it. This shows that it is not possible to directly excite SPPs with free propagating light or to couple SPPs directly out as propagating radiation due to the momentum mismatch.

2.2 SPP dispersion relation in different geometries

2.2.1 Dispersion relation in a multilayer structure

For the application of plasmonics in real devices and for the sake of device miniaturization it is often desirable to reduce the thickness of the metal and place the metal on different substrates. Since SPPs as surface waves are very sensitive towards the properties of their immediate environment the effect of a finite metal layer or different dielectric surrounding media upon the dispersion relations needs to be considered. Pockrand[37] theoretically described in 1978 a multilayer system which can be applied with high concordance to a lot of device geometries involving thin metal films. The Schematic in fig. 2.3 shows the multilayer system configuration used in the theoretical description. The dielectric

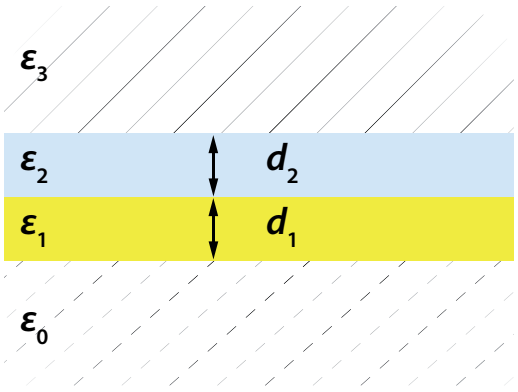

Figure 2.3: Schematic of a metal/dielectric multilayer system considered for the calculation of the SPP dispersion relation in eq. 2.7. The dielectric constants of the material are ε_i and d_i the thicknesses of the metal and the dielectric layer. The light interaction is determined to progress in the direction from material 0 to material 3

constants of the materials are ε_j and d_j the thicknesses of the metal and the dielectric layer. The light interaction is determined to progress in the direction from material 0 to material 3. This configuration is suitable for the description of the sample geometry used in the chapters 6 where a thin metal film (d_1 and a complex ε_1) is placed on a microscope cover glass (real ε_0) and covered with a protective layer of SiO_x (d_2 and real ε_2) surrounded by air (ε_3).

If Maxwell's equations are applied to this geometry restricted to p-polarized transvere magnetic (TM) fields, the dispersion relation of the eigenmodes are obtained from the eigenvalue equation $D_{0123} = 0$ with D_{0123} given as:

$$\begin{aligned} D_{0123} = \frac{k_{3z}}{\varepsilon_3} + \frac{k_{1z}}{\varepsilon_1} - \mathrm{i}\tan\left(k_{2z}d_2\right)\left(\frac{k_{3z}k_{1z}}{k_{2z}}\frac{\varepsilon_2}{\varepsilon_1\varepsilon_3} + \frac{k_{2z}}{\varepsilon_2}\right) \\ + r_{01}\mathrm{e}^{2\mathrm{i}k_{1z}d_1}\left[\frac{k_{1z}}{\varepsilon_1} - \frac{k_{3z}}{\varepsilon_3} - \mathrm{i}\tan\left(k_{2z}d_2\right)\left(\frac{k_{3z}k_{1z}}{k_{2z}}\frac{\varepsilon_2}{\varepsilon_1\varepsilon_3} - \frac{k_{2z}}{\varepsilon_2}\right)\right] \end{aligned} \tag{2.7}$$

with

$$k_{jz} = \sqrt{\varepsilon_j\left(\frac{\omega}{c}\right)^2 - k_{\mathrm{SPP}}^2} \quad , \qquad r_{01} = \left(\frac{k_{1z}}{\varepsilon_1} - \frac{k_{0z}}{\varepsilon_0}\right)\left(\frac{k_{1z}}{\varepsilon_1} + \frac{k_{0z}}{\varepsilon_0}\right)^{-1} \tag{2.8}$$

where k_{jz} is the wave vector component perpendicular and k_{SPP} parallel to the surface in the respective medium j. If real frequencies ω are considered the eigenvalue equation leads again to complex solutions for k_{SPP} where the real part of k_{SPP} describes the propagation and the imaginary part the damping of the eigenmodes. The first term of eq. 2.7 stands for the dispersion of SPPs propagating along the interface between two half-spaces ε_1 and ε_3 equivalent to eq. 2.2. The second term reflects the influence of the dielectric coating ε_2 and the third term considers the finite thickness d_1 of the metal film ε_1.

In the case of a transparent dielectric coating with a purely real dielectric function ($\varepsilon_2 \equiv \varepsilon'$) eq. 2.7 can be approximated by

$$k_{\mathrm{SPP}} = k_{\mathrm{SPP}}^{(0)} + k_{\mathrm{SPP}}^{(1)C} + k_{\mathrm{SPP}}^{(1)R} + k_{\mathrm{SPP}}^{(2)C} + k_{\mathrm{SPP}}^{(2)R} + k_{\mathrm{SPP}}^{(2)CR} \tag{2.9}$$

with

$$k_{\mathrm{SPP}}^{(0)} = \frac{\omega}{c}\sqrt{\frac{\varepsilon_1\varepsilon_3}{\varepsilon_1+\varepsilon_3}}, \tag{2.10}$$

already implemented as the dispersion of SPPs at the interface between to half-spaces (eq. 2.2). Additionally used are the correction terms

$$k_{\mathrm{SPP}}^{(1)C} = \frac{\omega}{c}\left(\frac{\varepsilon_2' - \varepsilon_3}{\varepsilon_2'}\right)\left(\frac{\varepsilon_1'\varepsilon_3}{\varepsilon' + \varepsilon_3}\right)^2\left(\frac{\varepsilon_2' - \varepsilon_1'}{\varepsilon_3 - \varepsilon_1'}\right)\left(-\varepsilon_1'\varepsilon_3\right)^{-\frac{1}{2}}\left(\frac{2\pi d_2}{\lambda}\right), \tag{2.11}$$

and

$$k_{\mathrm{SPP}}^{(2)C} = k_{\mathrm{SPP}}^{(1)C}\left[\frac{1}{2}\frac{k_{\mathrm{SPP}}^{(1)C}}{\mathrm{Re}\left(k_{\mathrm{SPP}}^{(0)}\right)}\left(2\frac{2\varepsilon_3^2 - \varepsilon_2'^2}{\varepsilon_3\left(\varepsilon_3 - \varepsilon_2'\right)} + \frac{\varepsilon_1' + \varepsilon_3}{-\varepsilon_3}\right) - \mathrm{i}\frac{1}{2}\frac{\varepsilon_1''}{\varepsilon_1'}\right], \tag{2.12}$$

which are considering the influence of the dielectric coating on the metal layer. The first order term (eq. 2.11) is real and therefore causes a shift of the SPP wave-vector proportional to $\frac{d_2}{\lambda}$ [11]. Meanwhile, the complex second order term (eq. 2.12) describes an increase in the inner damping in the case of $\varepsilon_2 > \varepsilon_3$. With growing thickness of the coating layer the power flow in the lossy metal increases which results in an increase of damping by a larger imaginary part of k_{SPP} [37]. The influence of the finite metal thickness d_1 is considered by

$$k_{\mathrm{SPP}}^{(1)R} = \frac{\omega}{c}r_{01}\left(\frac{2}{\varepsilon_3 - \varepsilon_1'}\right)\left(\frac{\varepsilon_1'\varepsilon_3}{\varepsilon_1' + \varepsilon_3}^{\frac{3}{2}}\right)\mathrm{e}^{-2\frac{2\pi d_1}{\lambda}\frac{-\varepsilon_1'}{\sqrt{-\varepsilon_1' - \varepsilon_3}}}, \tag{2.13}$$

and

$$k_{\mathrm{SPP}}^{(2)R} = k_{\mathrm{SPP}}^{(1)R}\left[\frac{1}{2}\frac{k_{\mathrm{SPP}}^{(1)R}}{\mathrm{Re}\left(k_{\mathrm{SPP}}^{(0)}\right)}\left(\frac{2\varepsilon_1' + \varepsilon_3}{-\varepsilon_3}\right) - \mathrm{i}\frac{\varepsilon_1''}{\varepsilon_1' - \varepsilon_3}\right], \tag{2.14}$$

with the correction term

$$k_{\mathrm{SPP}}^{(2)CR} = \frac{k_{\mathrm{SPP}}^{(1)R} k_{\mathrm{SPP}}^{(2)C}}{\mathrm{Re}\left(k_{\mathrm{SPP}}^{(0)}\right)}\left(-\frac{\varepsilon_1'}{\varepsilon_3} + \frac{2\varepsilon_3}{\varepsilon_3 - \varepsilon_2'} + \frac{\varepsilon_2'}{2\varepsilon_3}\right). \tag{2.15}$$

A small thickness of the metal film d_1 is mainly causing radiation damping of the SPP due to coupling to propagating waves in the half-space ε_0 also know as leakage radiation further described in section 2.4.1. Fig. 2.4 (a) compares the dispersion for the gold/air half-space

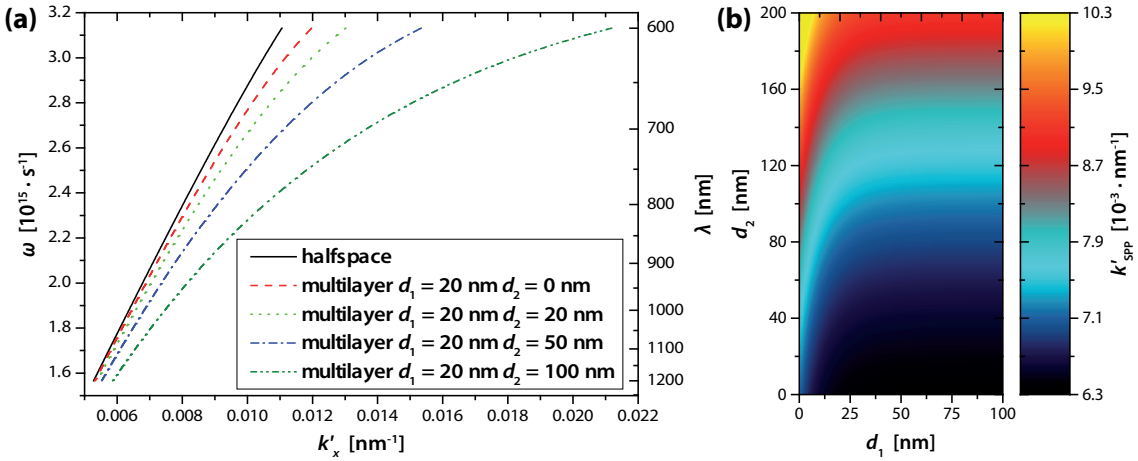

Figure 2.4: (a) SPP dispersion relations comparing the solution for a gold/air interface (according to eq. 2.2, black solid line) with the multilayer solutions for different glass coating thicknesses d_2, calculated according to eq. 2.7. (b) Correlation of the real part of the plasmon wave-vector k'_{SPP} with the thicknesses of a gold film d_1 and the glass coating d_2 at a wavelength of 1000 nm.

system (eq. 2.2, black solid line), with the dispersions calculated for a multilayer system (eq. 2.9, red dashed to dark green dashed double dotted line) consisting of glass as bottom half-space ($\varepsilon_0 = 2.25$), a 20 nm gold film (ε_1 according to Johnson and Christy[35]), glass with varying thicknesses as dielectric coating ($\varepsilon_2 = 2.25$) and air as top half-space ($\varepsilon_3 = 1$). The shift to higher wave vectors with increasing thickness of the glass coating d_2 reflects directly the influence of the term in eq. 2.11. Fig. 2.4 (b) depicts the correlation of the real part of the wave-vector with varying thickness of the glass coating d_2 and the gold film thickness d_1 at a wavelength of 1000 nm. The influence of the metal thickness on the real part of the wave-vector is small compared to the influence of the coating thickness. Only for small metal thicknesses ($\approx$ 1–25 nm in the illustrated case of gold) eq. 2.13 and 2.14 produce a significant change in the real part of the wave-vector.

2.2.2 SPP propagation length

Another important quantity for the description of SPPs which can be extracted from the dispersion relation is the propagation length L_D which is connected to the plasmon wave vector by

$$L_D = \left(k''_{SPP}\right)^{-1}. \tag{2.16}$$

This defines the propagation length L_D as length after which the initial amplitude of the SPP field has decayed to $\frac{1}{e}$. This damping is caused by ohmic losses of the electrons involved in the SPP oscillation and results finally in heating of the metal. If intensities are observed the propagation length is used as follows[33]:

$$L_D = \left(2k''_{SPP}\right)^{-1}. \tag{2.17}$$

The propagation length is of special interest in the design of plasmonic devices in order to consider an appropriate length scale of the involved structures. Fig. 2.5 (a) shows calculated propagation lengths L_D in the wavelength range from 400 to 1600 nm for the three metals silver, gold and copper according to eq. 2.16. The values for k''_{SPP} were calculated with the formula for a metal and dielectric half-space (eq. 2.2) using the values for the dielectric function of the three metals measured by Johnson and Christy[35]. A

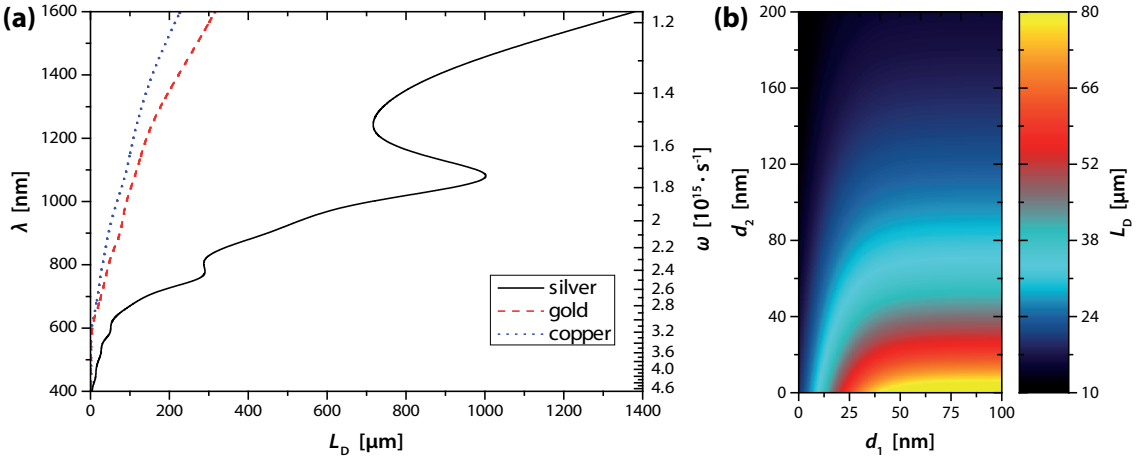

Figure 2.5: (a) Calculated propagation length L_D over a range of wavelengths/frequencies for silver (black solid line), gold (red dashed line) and copper (blue dotted line) according to eq. 2.16 using the k''_{SPP} values from eq. 2.2. (b) Dependency of the propagation length L_D at 1000 nm on the thickness of a gold film d_1 and the thickness of a glass cover layer ($\varepsilon_2 = 2.25$) d_2.

first general observation from fig. 2.5 (a) is an increase of the propagation length in all three metals with increasing wavelength. This is due to the fact, that the real part of the dielectric function of the metals decreases for higher wavelengths. Due to the decreasing penetration depth of the SPP into the metal with increasing wavelength, as described in section 2.1, the ohmic losses in the metal are reduced, which increases the propagation

length. The different propagation lengths for the different metals can be understood by the differences in the complex part of the metal dielectric function, which describes the losses upon interaction of the wave with the metal. Thus the imaginary part of the dielectric function increases from silver, to gold and to copper in the examined wavelength range of fig. 2.5.

Fig. 2.5 (b) shows the correlation between the propagation length L_{D} and the thicknesses of the metal film d_1 and the dielectric coating d_2. The results are obtained with the multilayer system (eq. 2.9) at a wavelength of 1000 nm for a gold film and a glass coating ($\varepsilon_2 = 2.25$) with glass as underlying half-space ($\varepsilon_2 = 2.25$) and air as covering half-space ($\varepsilon_3 = 1$). As the metal thickness exceeds the skin depth δ_1 of the SPP into the metal, radiation damping through coupling to propagating modes in the dielectric ε_0 ceases to play a role. This can be seen in the fast increase of the propagation length moving along the x coordinate in fig. 2.5 (b) from lower to higher d_1 values. The decrease of the propagation length with increasing thickness of the dielectric coating illustrates the behavior mentioned in section 2.2.1 (eq. 2.12). A larger amount of dielectric subjects more of the SPP to the inner damping in the metal for the case $\varepsilon_2 > \varepsilon_3$.

2.2.3 Dispersion relation in metal cylinders

Since the first characterization of propagating modes along a surface of a metal wire[38], noble metal nanowires caught increased attention in the literature because of their potential application as plasmonic building blocks[7]. Contrary to the case in a thin metal film, the SPP field in a wire is not only strongly confined in one dimension (z-axis) but in two dimensions, namely the z-axis and the axis perpendicular to the wire axis. This additional localization has a strong effect on the dispersion relation of SPPs in such wires, as shown in experiments with metal antennas, which resonances were shifted from the external wavelength, depending on the material properties[39] to λ_{eff}. Given the wire ge-

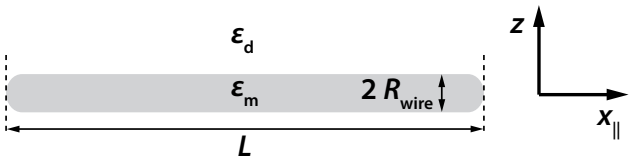

Figure 2.6: Schematic of the metal wire used for the calculation of the dispersion relation in eq. 2.19 denoting the wire length L, the radius R_{wire}, the dielectric function of the wire ε_{m} and the dielectric function of the surrounding medium ε_{d} .

ometry depicted in fig. 2.6 with the wire of a length L, the radius R_{wire}, consisting of the material ε_{m} and surrounded by the medium ε_{d}, the effective wavelength can be derived by[40]:

$$\lambda_{\mathrm{eff}} = \lambda_{\mathrm{exc}} \frac{k_0}{k_{\mathrm{SPP}}} - \frac{4R_{\mathrm{wire}}}{m}, \quad m \in \mathbb{N}. \tag{2.18}$$

Subtraction of the relation between the wire radius R_{wire} and the order of the resonance m pose a justified approximation due to the virtual increase of the wire length through the influence of the wire ends [40].

To investigate SPP propagation along a metal nanowire an analysis of the full vector wave equation [41] is necessary. Using waveguide theory the TM_0 modes of a cylindrical waveguide can be derived by solving the following equation [40]:

$$\frac{\varepsilon_{\mathrm{m}}(\lambda)}{\kappa_1 R_{\mathrm{wire}}} \frac{J_1(\kappa_1 R_{\mathrm{wire}})}{J_0(\kappa_1 R_{\mathrm{wire}})} - \frac{\varepsilon_{\mathrm{d}}}{\kappa_2 R_{\mathrm{wire}}} \frac{H_1^{(1)}(\kappa_1 R_{\mathrm{wire}})}{H_0^{(1)}(\kappa_1 R_{\mathrm{wire}})} = 0 \tag{2.19}$$

with

$$\begin{aligned} \kappa_1 &= k_0 \left[\varepsilon_{\mathrm{m}} - \left(\frac{k'_{\mathrm{SPP}}}{k_0} \right)^2 \right]^{\frac{1}{2}} \\ \kappa_2 &= k_0 \left[\varepsilon_{\mathrm{d}} - \left(\frac{k'_{\mathrm{SPP}}}{k_0} \right)^2 \right]^{\frac{1}{2}} \end{aligned} \tag{2.20}$$

Exemplary results from eq. 2.19 for a silver wire with the radius $R_{\mathrm{wire}} = 5\,\mathrm{nm}$ (black solid line) and $R_{\mathrm{wire}} = 10\,\mathrm{nm}$ (dark blue dotted line) are shown in fig. 2.7. In contrast to

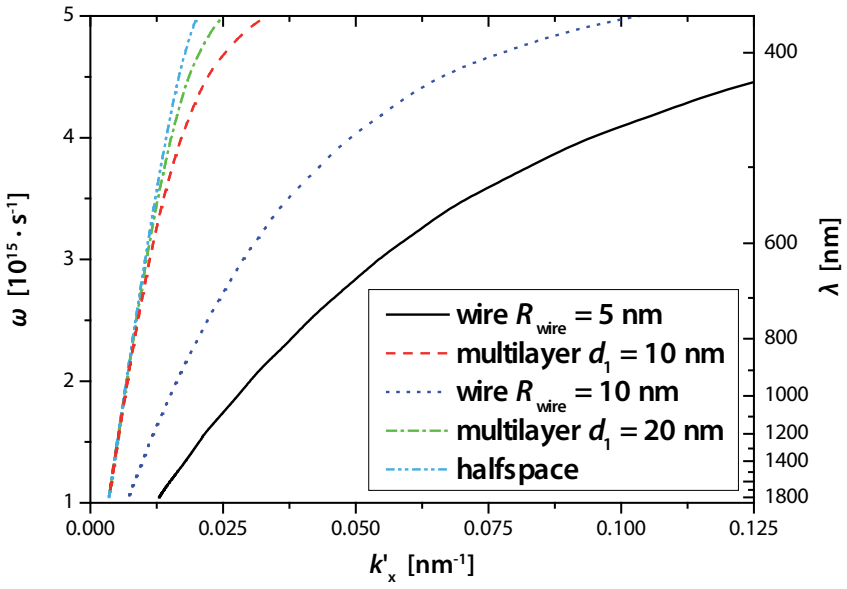

Figure 2.7: Comparison of SPP dispersion relations calculated according to the formula for metal cylinders eq. 2.19 with a wire radius R_{wire} of 5 (black solid line) and 10 nm (dark blue dotted line), calculated for a multilayer geometry (eq. 2.9) with a metal thickness d_1 of 10 (red dashed line) and 20 nm (green dash dotted line) and the half-space formula eq. 2.2 (light blue dash double dotted line).

that, dispersion relations for the corresponding film thicknesses in a multilayer geometry ($d_1 = 10$ and 20 nm, red dashed and green dash dotted line) according to eq. 2.9 and the half-space dispersion (eq. 2.2, bright blue dash double dotted line) are also shown. The surrounding medium for all calculations in fig. 2.7 was assumed as air ($\varepsilon_{\mathrm{d}} = 1$, $\varepsilon_0/\varepsilon_2 = 1$)

For the dispersion relations of wires a clear trend is seen towards higher wave-vectors as compared to extended metal films that can be seen as the result of the additional confinement.

2.3 Excitation of SPPs

In order to excite SPPs energy and momentum conservation have to be fulfilled. As mentioned before in section 2.1 the plasmon wave-vector k_{SPP} exceeds always the wave-vector for light in free space and it is therefore not possible to excite a SPP directly by light propagating in free space. This is illustrated in fig. 2.8 with the dispersion of a silver/air interface (black solid line) and the light line k_0 (red dashed line). An indirect method for

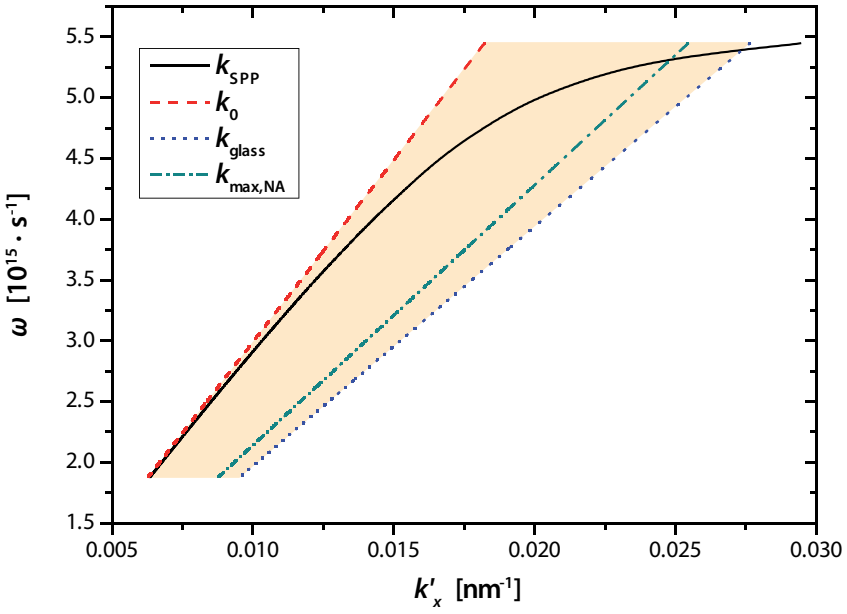

Figure 2.8: Illustration of the SPP dispersion for a silver/air interface (black solid line), the light line k_0 (red dashed line), the dispersion for light in glass k_{glass} (blue dotted line) and the maximum dispersion accessible with a high NA oil immersion objective $k_{\mathrm{max,\,NA}}$ (NA = 1.4, green dashed dotted line). The orange shaded area indicates the range of possible resonance between light propagating in a glass prism/objective and a SPP by adjusting the angle θ (see fig. 2.9 (a), (b) and (c)).

launching SPPs using freely propagating waves employs the Otto configuration, where an evanescent wave, formed at a glass/air interface in a total internal reflection geometry, excites SPPs at a metal/air interface between a prism and a metal film (see schematic fig. 2.9 (a))[10]. By adjusting the angle of incidence of the totally reflected beam inside the prism the resonance can be tuned over a range of energies:

$$k_{\mathrm{SPP}} = k_{\mathrm{glass}} = \frac{\omega}{c} n_{\mathrm{glass/obj}} \sin\theta. \tag{2.21}$$

The tuning behavior is indicated in fig. 2.8 by the orange shaded area from the maximum dispersion k_{glass} ($\theta = 90°$, green dashed dotted line) towards the light line k_0 ($\theta = 0°$). SPPs with a dispersion within this region are also called leaky modes since coupling to free propagating wave is possible, whereas modes with a dispersion shifted to higher k_{SPP} values are referred to as bound modes[42].

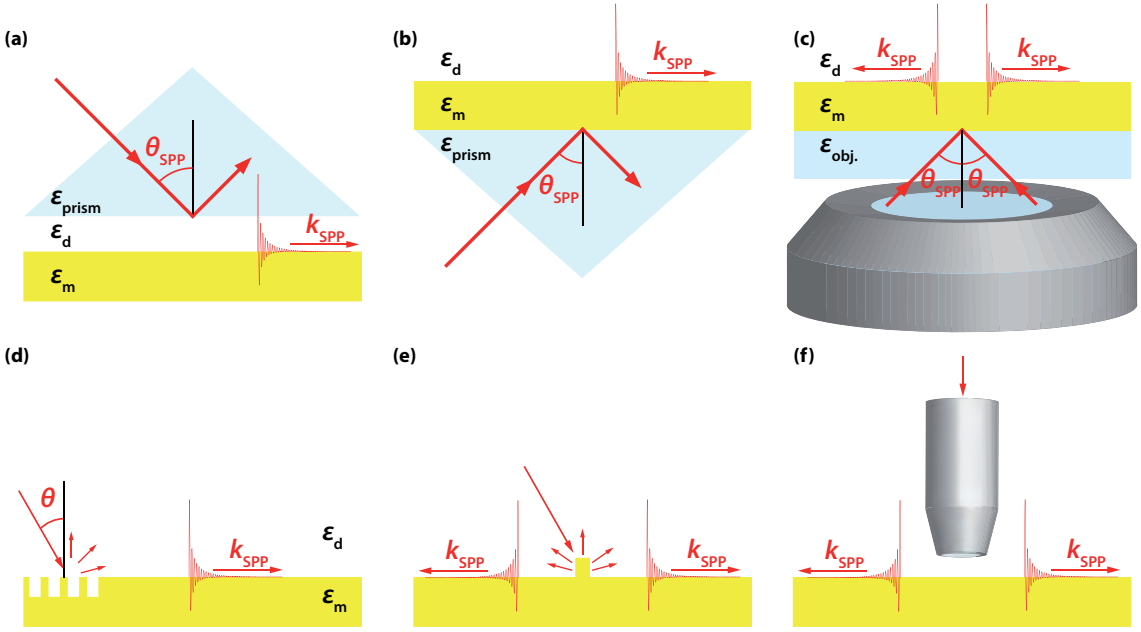

Figure 2.9: Different SPP excitation schemes. (a) Otto configuration. (b) Kretschmann configuration. (c) Kretschmann like excitation with a high NA microscope oil immersion objective. (d) excitation with an aperture SNOM probe. (e) excitation with a surface defect. (f) excitation with a grating. Adapted from[43]

Fine control of the small gap of air between the prism and the metal film proposes an experimental challenge, using the Otto configuration. This problem was solved by the Kretschmann configuration where the metal film is deposited directly onto the prism (fig. 2.9 (b))[11]. Excitation of SPPs can be monitored for both, the Otto and the Kretschmann configuration, by measuring the amount of reflected light while tuning the angle of incidence into the prism (see fig. 2.10). The SPP resonance condition according to eq. 2.21 appears as a minimum in the reflection. These reflection measurements are often called in the literature attenuated total reflection (ATR) method. Fig. 2.10 shows the results of typical reflection measurements for the (a) Otto and (b) Kretschmann configuration. The origin of the minimum in the ATR reflectivity curves can be interpreted in two ways: First it can be seen as destructive interference between directly reflected light at the interface and light emitted by the SPP after its excitation due to radiation damping through coupling back to propagating waves. This can be seen in the reduction of the reflectivity contrast for increasing metal film thicknesses in fig. 2.10 (b). Secondly, to excite SPPs the incident propagating light at the specific angles θ is converted into the

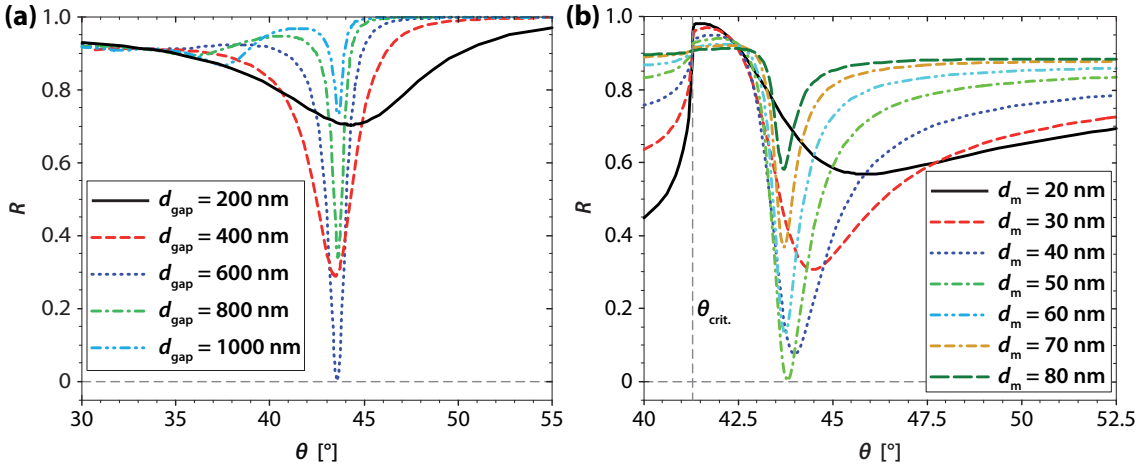

Figure 2.10: (a) ATR measurement in the Otto configuration for a gold film. The reflection is plotted against the incident angle into the prism θ showing reflection curves for different gap sizes d_{gap} between the prism and the metal film ranging from 200 to 1000 nm. (b) ATR measurement in the Kretschmann configuration plotted as reflection R against the incident angle into the prism θ for a gold film with thicknesses d_{m} of 20 to 80 nm. Indicated is also the critical angle $\theta_{\mathrm{crit.}}$ for the prism glass/air interface (gray dashed vertical line). Adapted from [33].

surface bound wave which is not accessible for the detector and appears as a reduction in the reflection signal.

An adaption of the Kretschmann configuration is the use of a high numerical oil immersion objective as a substitute for the prism (fig. 2.9 (c)) [31,44–46]. This method provides a further step forward in flexibility regarding the choice of investigated samples, since any sample fabricated on a microscope cover glass can be measured. One drawback of this method compared to the initial use of a prism is the smaller range of accessible angles due to the limited NA. of the objective (see $k_{\mathrm{max,\,NA}}$ in fig. 2.8).

Another method to overcome the mismatch of the free-space wave-vector k_0 and the SPP wave-vector k_{SPP} is the use of diffraction gratings [32,47]. The diffraction grating is able to overcome the momentum mismatch by adding an additional wave-vector component connected to the grating constant g as follows:

$$k_{\mathrm{SPP}} = k_0 \sqrt{\varepsilon_{\mathrm{d}}} \sin(\theta) + m \frac{2\pi}{g}, \quad m \in \mathbb{N} \tag{2.22}$$

Suitable values for the angle of incidence θ, the lattice constant g and order of refraction m for each excitation wavelength need to be chosen [48] in order to achieve the resonance condition with the SPP and the grating coupler fig. 2.9 (d). Such grating couplers have been used to launch SPPs on metallic tips for the application in apertureless SNOM techniques [49] or on plasmonic waveguides [16]. Not only linear gratings, but any regular sub-wavelength patterned structure such as nanohole or slit arrays can be used to couple to SPPs [50]. From optical gratings the concept of adding a wave-vector component can be expanded to scattering at surface defects such as nanoparticle arrays [51], rough surfaces [32],

few metal ridges[52] down to single metal particles[12,53], single holes[54] and single slits[55] (fig. 2.9 (e)). These single particles or holes behave like a dipolar SPP source when excited with linearly polarized light. This situation can be also achieved by coupling excitons in molecular films[56–61] and single quantum dots[62–64], excited by laser irradiation, to SPPs. These excitons can also be electrically generated in an inorganic semiconductor based light emitting diode (LED)[65,66], organic light emitting diode (OLED)[67] or a SWCNT field effect transistor (FET)[68] configuration .

A further approach to excite SPPs in a more localized manner is the use of sub-wavelength light sources such as aperture probes[53,69–71] or nanodiamonds at the end of a near field probe[72]. In addition to the aforementioned optical approaches, SPPs can be also excited by high[73] and low energy electrons in the method of electron energy loss spectroscopy (EELS)[74]. But also a scanning tunneling microscopy (STM) tip[21,22,75] can be used as a localized, electron based SPP source.

2.4 Detection of SPPs

All schemes presented before to excite SPPs enable in reverse also their detection. This is for example seen by the minimum in ATR measurements or in EELS (sec. 2.3). But a few concepts are worth mentioning, regardless, since they enable to detect SPPs without the detection method being involved in the SPP excitation.

2.4.1 Leakage radiation

One frequently used concept is the detection of leakage radiation which was first experimentally observed for SPPs excited on rough metal films[73,76]. For a sufficiently thin metal film the SPP can couple propagating radiation into the underlying glass substrate since for gold and silver the SPP wave-vector k'_{SPP} lies within the accessible wave-vector range for a glass substrate (see orange shaded are in fig. 2.8):

$$k_0 < k'_{\mathrm{SPP}} < k_0\sqrt{\varepsilon_0} \tag{2.23}$$

As depicted in fig. 2.11 the leakage radiation is emitted at the plasmon resonance angle θ_{SPP} which is the same angle at which in an ATR measurement the minimum of reflection appears. This range of angles is connected to the k-space by:

$$k'_x = 2\pi\frac{\sqrt{\varepsilon_0}}{\lambda}\sin(\theta). \tag{2.24}$$

In k-space the intensity of leakage radiation can be described by the following Lorentzian distribution[12]:

$$I\left(k_x\right) \propto \frac{1}{\left(k_x - k'_{\mathrm{SPP}}\right)^2 + \left(k''_{\mathrm{SPP}}\right)^2} \tag{2.25}$$

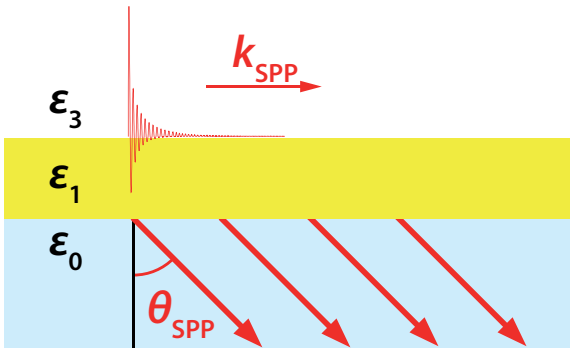

Figure 2.11: Schematic of leakage radiation emission from a propagating SPP on a metal film (ε_1) into the underlying glass substrate ε_0. The angle of emission is θ_{SPP}, which is equal to the angle of the minimum reflection in the ATR measurements.

Thus, by measuring the full width at half maximum (FWHM) of the detected angular distribution of leakage radiation intensity, the propagation length L_D of the SPP can be determined according to eq. 2.17. The direct imaging via leakage radiation microscopy e.g. of structured metal films[77], metal stripes and wires[78] was reported in the literature. Detection of leakage radiation was also applied in the realization of a SPP beam profiler[79] and a SPP beam splitter based on metal particles[80]. A useful technique to detect the angular distribution of leakage radiation emission is the method of Fourier plane imaging described in more detail in chapter 3.

2.4.2 Near-field Microscopy

The technique to detect propagating SPPs with sub-wavelength resolution with a near-field optical microscope is often called photon scanning tunneling microscopy (PSTM) or STOM[34,81]. Tunneling refers here to the similarity to STM, that the evanescent SPP collected by the aperture are converted to propagating modes guiding along the fiber to the detector (fig. 2.12). Usually pulled or etched glass fibers are used for this technique which are additionally coated at the tip end with a metal film in order to prevent radiation losses out of the fiber[82]. The lateral resolution is determined by the actual shape and size of the tip apex and can go down to 50 nm[31]. A feedback mechanism acting on either a STM signal[83] or the frequency of a piezoelectric tuning folk[84] controls the tip sample distance and enables the approach up to several nm. Thus the core of the fiber tip is in direct contact with the evanescent tail of the SPP wave. In varying the distance in the z direction Adam et al.[85] were able to confirm the spatial extent of the SPP fields into the surrounding air above a silver film (eq. 2.6, sec. 2.1). Lateral maps of the SPP field amplitude can be also measured and at the same time the feedback mechanism gives access to the topographic information on the sample. This has been used to study the SPP propagation on structured metal films[81,86], silver nanowires[87,88], chains of metal nanoparticles[89], nanoantennas[90] and metal waveguides[16,83]. It is also possible to investigate the interference pattern of

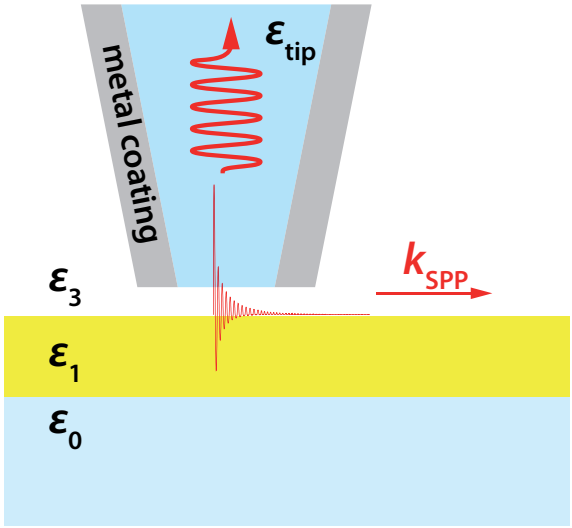

Figure 2.12: Schematic of SPP detection via PSTM/STOM. The aperture tip is able to collect the evanescent SPP waves and guide them as propagating waves along the fiber to the detector.

several SPPs since a complete map of the fields is obtained, which has been shown for SPP scattering and self interference at nanoparticles on metal films[53], plasmonic Bragg gratings[91] and the standing wave pattern of two counter-propagating SPP waves[92].

2.4.3 Fluorescence detection

SPP as oscillating charges on a metal surfaces are also known to be able to excite emitters such as quantum dots or fluorescent molecules situated in the vicinity of the evanescent fields. One condition for this excitation is the spectral overlap of the SPP and the absorption spectrum of the emitter. The intensity of emission is proportional to the intensity of the local SPP field at the emitter position[93]. This concept was used by Ditlbacher et al.[94] to image the SPP fields excited by surface defects and ridges in metal films[52]. Successful imaging of SPP fields is possible if the direct non-radiative quenching of fluorescence by close presence of the metal[95] is prevented through introducing a transparent dielectric spacer layer between the metal and the emitters. Under the influence of the high electrical field strengths of the SPP the irreversible alteration in the molecular structure of the emitters needs to be considered which in consequence results in bleaching of the fluorescence[94]. This bleaching was deliberately used to image SPPs propagating along a gold nanowire[96].

3 Back focal plane (BFP) imaging

Optical microscopy is a long established powerful tool to investigate objects with sizes that cannot be seen by the human eye. In the case of confocal microscopy the optical resolution can be as small as the diffraction limit [97]. The optical resolution determines the minimum distance between two objects at which their signatures still can be distinguished. This limit was pushed even further with new high resolution methods such as tip-enhanced microscopy [98–100] or super-resolution techniques [97,101,102].

In all these techniques a microscope objective is involved in the imaging process. Through the objective it is possible, not only to determine the information on the position, size and wavelength of the investigated object, but also to extract the information in which angles the light from the object is emitted or scattered. This can be achieved by observing the Fourier plane of the imaging lens with a method called BFP imaging [17] or recording of radiation patterns [103,104]. BFP imaging enables access to additional information of the observed emitter such as identification of different radiation channels [105], changes in the emission characteristics due to coupling effects [106] or material properties [107]. The distribution of radiation in the BFP can also be used in the context of ellipsometry [108] and to determine SPP propagation properties [19].
In the following chapter an overview of the image formation in the BFP is given followed by a theoretical description of the Fourier pattern from single and random dipoles on an interface. The chapter concludes with an introduction to BFP imaging applied in the context of SPPs.

3.1 Theoretical description of radiation patterns in the BFP

An emitter in a uniform medium exhibits a radiation behavior only determined by the inherent emitter properties while the surrounding medium does not favor or hinder emission into certain angles. For example a point dipole in a uniform medium with the refractive index n_1 emits according to the model of a Hertzian dipole, radially symmetric with respect to the axis parallel to the dipole moment, with the highest intensity into angles perpendicular to the dipole axis. Placing this emitter on an dielectric medium with n_2 surrounded by a dielectric with $n_1 < n_2$ changes the fractions of radiation emitting into different angles and angular regions defined in fig. 3.1 (a). The total radiated power can be divided into emission into the upper half-space P_{u}, the forbidden zone of the lower

half-space P_f for angles larger than the critical angle $\theta_\mathrm{crit.}$, the allowed zone P_a for angles smaller than $\theta_\mathrm{crit.}$ and power dissipated into the surface P_n[109]:

$$P = P_\mathrm{u} + P_\mathrm{f} + P_\mathrm{a} + P_\mathrm{n} \tag{3.1}$$

This geometry can be applied to a typical microscopy situation: An emitter, situated on

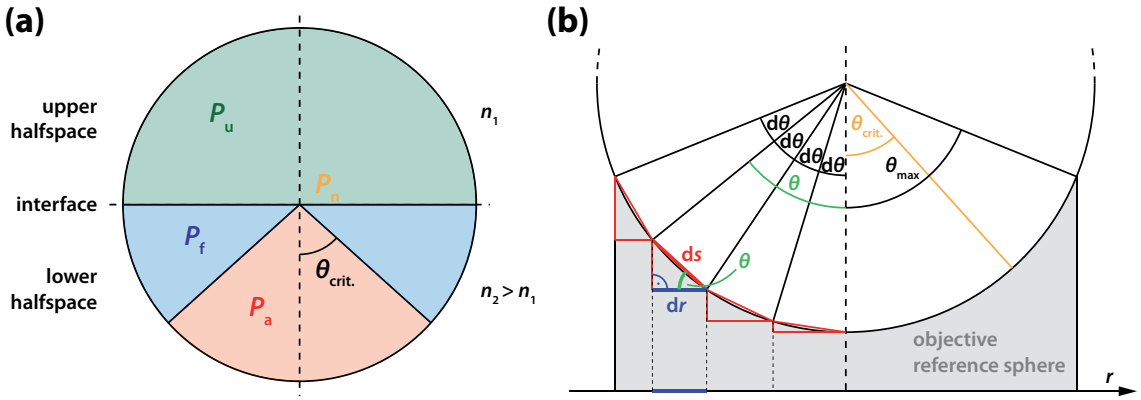

Figure 3.1: (a) Schematic of radiated power by an emitter on an interface, in the center of the circle, into different angular zones: Into the upper half-space P_u, the forbidden zone of the lower half-space P_f for angles larger than the critical angle $\theta_\mathrm{crit.}$ and the allowed zone P_a for angles smaller than $\theta_\mathrm{crit.}$. Also indicated is the power dissipated into the surface P_n. Adapted from[110]. (b) Shows a schematic of the projection of the angular emission in the allowed zone by an imaging lens onto the BFP. The emitter is situated in the center of the emission sphere. Also indicated are the critical angle $\theta_\mathrm{crit.}$ and maximum collected angle by the lens θ_max. Adapted from[111].

a microscope cover glass, is placed into the focus of a high NA oil immersion objective. Thus the light emitted into the lower half-space medium in the allowed light P_a and parts of the forbidden light P_f can be collected. In order to calculate the intensity distribution in the BFP of an objective as a function of the emission angle θ (fig. 3.1 (b)) the Weyl representation can be applied. It uses the decomposition of the spherical wave started by the emitter into planar waves and evanescent waves[112]. This approximation is well suited for modern plan microscope objectives[13] which are corrected for the curvature of field on the Petzval surface[113]. With this the intensity distribution in the Fourier plane of an objective lens can in general be expressed by the fields generated by the emitter E_emit:

$$I_\mathrm{BFP} \propto \frac{1}{\cos\theta} \left|E_\mathrm{emit}\right|^2 . \tag{3.2}$$

This includes the factor $\frac{1}{\cos\theta}$, considering the conservation of energy for the projection onto the BFP[13] illustrated in fig. 3.1 (b). The same amount of power radiating from the emitter along each equally sized angular section $\mathrm{d}\theta$ is captured on $\mathrm{d}s$. However, for increasing angles θ this equal amount of power is projected onto a decreasing section $\mathrm{d}r$. This can be corrected by introducing the factor $\frac{1}{\cos\theta}$ originating from the relation $\mathrm{d}r = \cos\theta \mathrm{d}s$ (fig. 3.1 (b)). For the experimental application of BFP imaging it has to be noted that most objectives are subdue to attenuation of the marginal rays which results in an apparent reduction of the NA[114,115].

3.1.1 Dipolar emission characteristics in the BFP

Calculation of intensity distribution in the BFP

If a point dipole is placed on a dielectric interface and brought into the focus of a high NA objective the fraction of power emitted into the different zones is altered compared to the free space Hertzian model. The geometry of this system and all necessary parameters for the theoretical calculation are shown in fig. 3.2 as published by Lieb et al. [13]. Φ and Θ are

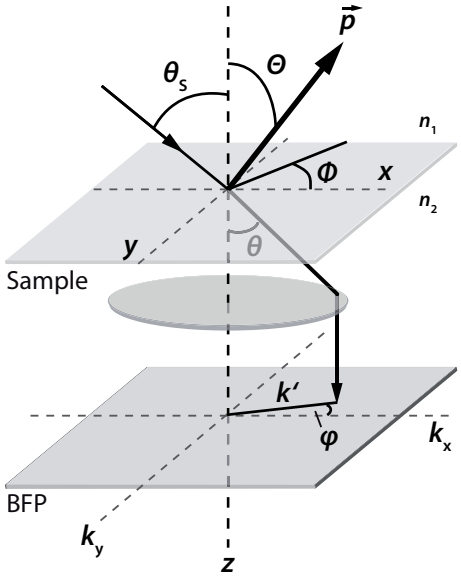

Figure 3.2: Schematic of the geometry used for the calculation of Fourier patterns from dipoles on an interface. A dipole $\vec{p}$ with the orientation angles Φ and Θ is situated on an interface with the refractive indices n_1 and n_2. The emission of the dipole into different angles θ is mapped onto the BFP in dependence of k_x and k_y. Adapted from [111].

the orientation angles for the dipole $\vec{p}$, and θ_{S} denotes the incident angle complementary to the emission angle θ according to Snell's law:

$$\theta_S = \arcsin\left(\frac{n_2 \sin\theta}{n_1}\right). \tag{3.3}$$

This allows for complex valued incident angles θ_{S}. The relation between the emission angle θ and the k-vector coordinate system in the BFP can be expressed as the following:

$$\begin{aligned} \left|k'\right| &= 2\pi\frac{n_2}{\lambda}\sin(\theta) = k_0 n_2 \sin(\theta), \\ \begin{pmatrix} k'_x \\ k'_y \end{pmatrix} &= \begin{pmatrix} \cos\varphi \\ -\sin\varphi \end{pmatrix} \cdot \left|k'\right|. \end{aligned} \tag{3.4}$$

For the calculation of the intensity distribution of a single dipole in the BFP according to eq. 3.2:

$$I_{\mathrm{dipole}}(\theta,\varphi) \propto \frac{1}{\cos\theta}\left(E_p E_p^* + E_s E_s^*\right), \tag{3.5}$$

the parallel and perpendicular field components E_p and E_s can be written as:

$$\begin{aligned} E_p &= c_1(\theta)\cos\Theta\sin\theta + c_2(\theta)\sin\Theta\cos\theta\cos(\varphi-\Phi), \\ E_s &= c_3(\theta)\cos\Theta\sin(\varphi-\Phi). \end{aligned} \tag{3.6}$$

The c coefficients are

$$\begin{aligned} c_1(\theta) &= n^2\frac{\cos\theta}{\cos\theta_S}t^p(\theta_S)\,\Pi(\theta_S), \\ c_2(\theta) &= nt^p(\theta_S)\,\Pi(\theta_S), \\ c_3(\theta) &= -n\frac{\cos\theta}{\cos\theta_S}t^s(\theta_S)\,\Pi(\theta_S), \end{aligned} \tag{3.7}$$

with

$$\Pi(\theta) = \mathrm{e}^{-\mathrm{i}k_0 n_1\cos(\theta_S)\delta}. \tag{3.8}$$

using the relative refractive index $n = \frac{n_2}{n_1}$. In this case the Fresnel transmission coefficients for p- and s-polarized light are expressed by[48,113]:

$$\begin{aligned} t^p &= \frac{2n_1\cos\theta_S}{n_1\cos\theta + n_2\cos\theta_S}, \\ t^s &= \frac{2n_1\cos\theta_S}{n_1\cos\theta_S + n_2\cos\theta}. \end{aligned} \tag{3.9}$$

Π in eq. 3.8 denotes a propagation factor for the light traveling through the upper half-space if the emitter is placed at a distance δ from the interface. Fig. 3.3 (a)-(d) shows the results of this calculation for dipoles with different orientations (a)-(c), as well as for several dipoles with random orientation (d), verified for the first time experimentally by Fattinger and Lukosz[116]. For the calculation dipoles were placed on a glass cover-slide ($n_2 = 1.5$) in the focus of an oil immersion objective with NA = 1.4 surrounded by air ($n_1 = 1$). The pattern for a vertical dipole (fig. 3.3 (a)) shows a rotationally symmetric intensity distribution with a maximum situated in the area of angles slightly larger than the critical angle $\theta_{\mathrm{crit.}}$. This is also indicated in the figure by the black dashed circle to mark the radius for $\frac{|k'|}{k_0}$ = NA = 1. No light is emitted in the central region of the pattern. The two BFP patterns for the in-plane dipoles (fig: 3.3 (b) and (c)) exhibit axial symmetry with the symmetry axis oriented parallel to the dipole axis. Again the main fraction of the radiation is concentrated in two lobes in the ring between the critical angle $\theta_{\mathrm{crit.}}$ and the maximum angle collected by the objective $\theta_{\max}$. Due to the symmetry of the field functions in eq. 3.6 the BFP intensity for dipoles with random orientation can be calculated by the sum of the patterns from three individual dipoles oriented along the major axes x, y and z (fig. 3.3 (a)-(c)). The radiation pattern for randomly oriented dipoles (fig. 3.3 (d)) is again rotationally symmetric with a high similarity to the pattern of a vertical dipole (fig. 3.3 (a)). Although, the main differences are the increased intensity in the central region as well as a broader intensity distribution in the ring of the forbidden zone due to the contribution of the two in-plane dipole components.

From the patterns in fig. 3.3 it can be also seen, that for all dipole orientations the majority of the intensity is emitted in the forbidden region P_{f}. This indicates that for the detection

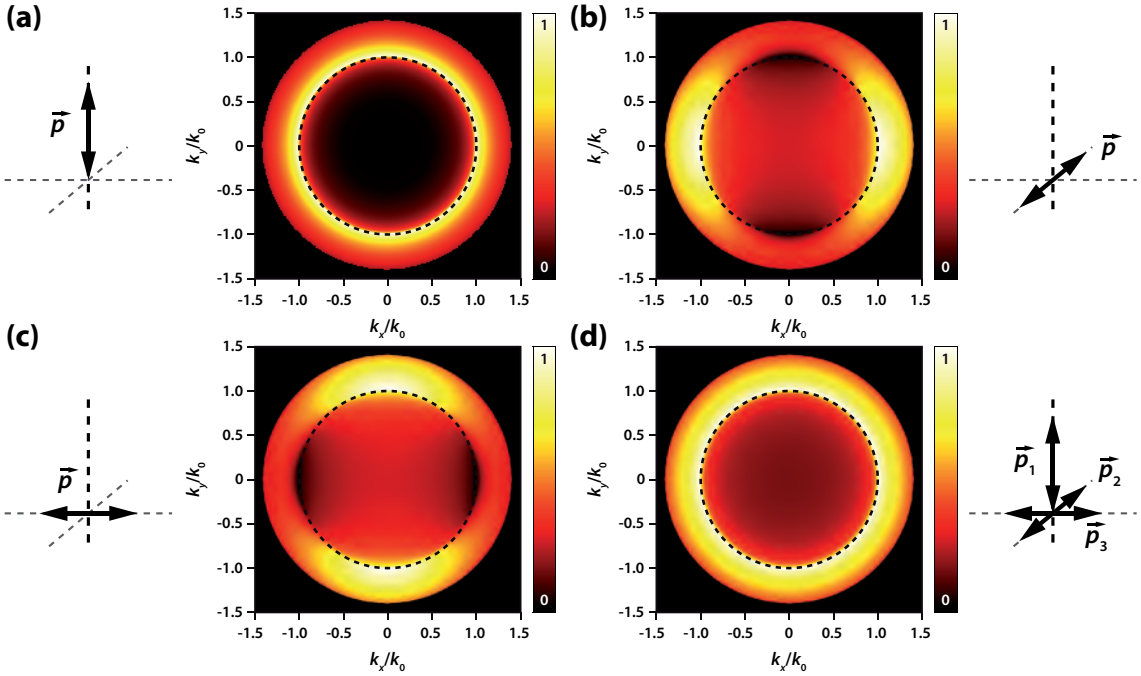

Figure 3.3: Calculated BFP patterns for dipoles on a glass/air interface with different orientations according to fig. 3.2. In (a) $\Phi = 0°$ and $\Theta = 0°$, in (b) $\Phi = 0°$ and $\Theta = 90°$, in (c) $\Phi = 90°$ and $\Theta = 90°$ and in (d) the pattern for dipoles with random orientation. In all images the k values corresponding to the critical angle $\theta_{\text{crit.}}$ are indicated by a black dashed circle. Adapted from [110].

of single dipole emitters with a microscope it is favorable to use an objective with a NA larger than 1 for increased detection efficiency.

Detection efficiency of dipoles

As shown in the previous section the fraction of emission radiation into the different angular zones changes with the dipole orientation. This makes the distinction between contributions from differently oriented dipoles possible. By comparing the BFP patterns for a vertical (fig. 3.3 (a)) and an in-plane dipole (fig. 3.3 (b), (c)) it is already evident, that the central part of the pattern without intensity for the vertical dipole enables the quantitative analysis of the two contributions [105]. Also the collection angle is an important factor to determine how much radiation can be detected with the given microscope objective. This can be summarized by introducing a measure for the detection efficiency γ which puts the detected power P_{det} in the allowed zone and a part of the forbidden zone in relation with the total radiated power by the emitter P:

$$\gamma = \frac{P_{\text{det}}}{P} \tag{3.10}$$

with the detected power P_{det} given by:

$$\begin{aligned} P_{\mathrm{det}} &= \int_0^{\theta_{\mathrm{max}}} P_{\mathrm{a}}\,\mathrm{d}\theta, \quad \text{for NA} \leq 1 \\ P_{\mathrm{det}} &= P_{\mathrm{a}} + \int_{\theta_{\mathrm{crit.}}}^{\theta_{\mathrm{max}}} P_{\mathrm{f}}\,\mathrm{d}\theta, \quad \text{for NA} > 1. \end{aligned} \tag{3.11}$$

Fig. 3.4 shows a plot of the detection efficiencies of a vertical ($\gamma_{\perp}$, black solid line) and an in-plane dipole ($\gamma_{||}$, red dashed line), as well as for randomly oriented dipoles (γ_{random}, blue dotted line) radiating at 670 nm as a function of the maximum detected angle θ_{max}. The

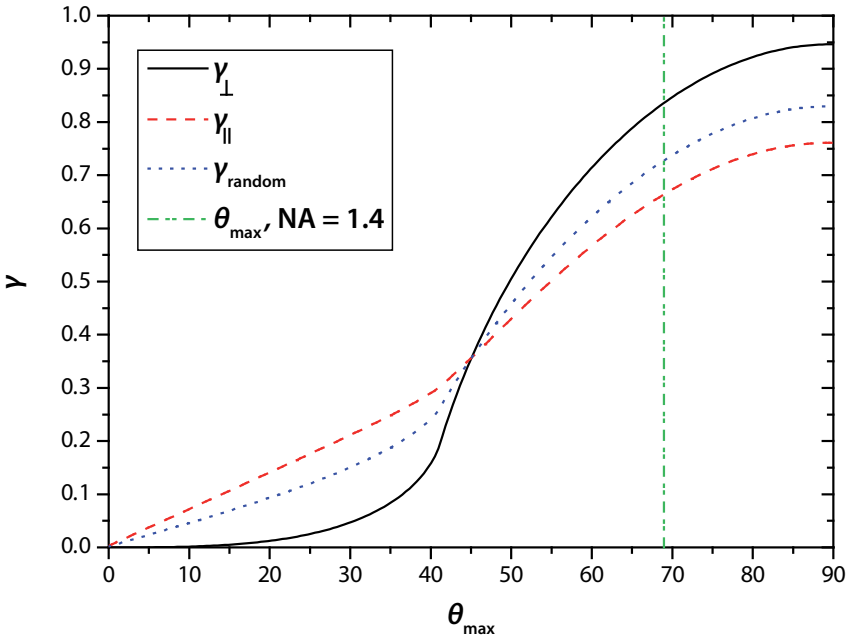

Figure 3.4: Plot of the detection efficiency γ for a vertical ($\gamma_{\perp}$, black solid line) and an in-plane dipole ($\gamma_{||}$, red dashed line), as well as randomly oriented dipoles (γ_{random}, blue dotted line) on a glass substrate ($n_2 = 1.51$) detected with an index matched oil immersion microscope objective as a function of the maximum detected angle θ_{max}. The green vertical dash dotted line indicates the maximum collected angle for an objective with a NA = 1.4.

green, vertical dash dotted line indicates the detection efficiencies $\gamma_{\perp} = 0.82$, $\gamma_{||} = 0.65$ and $\gamma_{\mathrm{random}} = 0.71$ for an objective with NA = 1.4, $\theta_{\mathrm{max}} = 68.96°$ as in all optical setups used for this work (see section 5.1). Again, from fig. 3.4 it is evident, that for single molecule detection an objective with NA > 1 is favorable. In comparison, the detection efficiencies for the investigated dipoles for a common air objective (NA = 0.95, $\theta_{\mathrm{max}} = 39.30°$) are much lower: $\gamma_{\perp} = 0.14$, $\gamma_{||} = 0.30$ and $\gamma_{\mathrm{random}} = 0.24$.

3.2 SPP BFP imaging

3.2.1 SPP signatures in the BFP

As described in the previous chapter in section 2.3, SPPs exhibit a distinct reflection minimum in a specific angular range when excited in the Kretschmann configuration. This concept can be transferred to the Kretschmann-like configuration if the prism is replaced by a high NA microscope objective. By detecting the reflected light in the BFP all accessible angles can be observed at the same time[15,117–120]. Fig. 3.5 (a) shows a representative experimental pattern for a reflected, linearly polarized (white double arrow) beam at 900 nm, from a 20 nm gold film coated with 20 nm SiO_x ($n_2 = 1.5$) in the BFP. The used objective had a NA of 1.4 defining the limiting radius of the pattern. Clearly

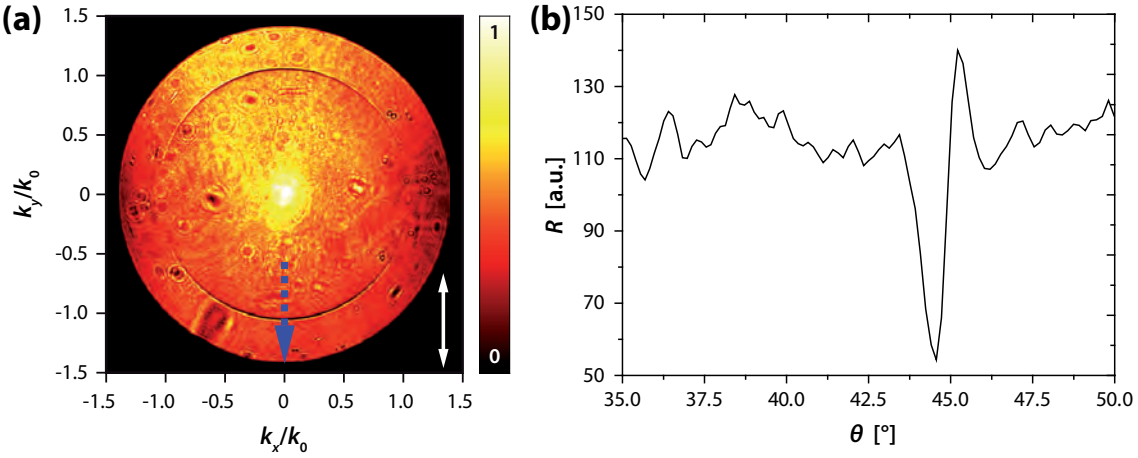

Figure 3.5: (a) Reflection BFP pattern from a 20 nm gold film coated with 20 nm SiO_x ($n_2 = 1.5$) and excited at 900 nm with a linearly polarized laser source. The polarization direction is indicated by the white double arrow. (b) Shows a magnified cross section of the reflection pattern along the blue dashed arrow revealing the ATR minimum.

the two dark arcs[15,118–120] can be seen at the angle with the highest contrast in direction of the incident polarization of the laser source. A magnified part of the cross section along the blue indicated arrow is shown in fig. 3.5 (b). The angle with the smallest reflection is at 44.6°, which corresponds to a k_{SPP} according to eq. 2.24 of $7.44 \cdot 10^6\,\mathrm{m}^{-1}$. A theoretical value of $k_{SPP} = 7.38 \cdot 10^6\,\mathrm{m}^{-1}$ calculated with the multilayer formula (eq. 2.9) for the given geometry shows good agreement. For slightly larger angles a weak increased signal occurs. This is due to the constructive interference of directly reflected light with the leakage radiation emitted by the launched SPPs. The exact position of this increased contribution differs in the literature from angles smaller than the ATR minimum[118,121] and larger[14].

Again, the same concepts for excitation of SPPs can be applied to the detection of launched plasmons as shown in section 2.4. Detection of angular resolved leakage radiation in the BFP has been applied to SPPs propagating along waveguides[122], nanowires[123] and launched by aperture[53] and STM tips[21,22]. Also SPPs launched by a thin film of randomly

oriented dye molecules on a metal film, mentioned in the literature as surface plasmon coupled emission (SPCE)[57,124–127] were investigated by BFP imaging.

3.2.2 Calculation of BFP patterns for propagating plasmons on a noble metal nanowire

Shegai et al.[19] expanded the calculation of Lieb et al.[13] from a single dipole to a chain of dipoles connected by a phase in order to describe SPP propagation along a plasmonic NW. The resulting BFP pattern shows the SPP signature through leakage radiation. This theoretical description can be achieved by multiplying a single dipole pattern with a structure factor S, which contains the phase correlation between the different dipoles (fig. 3.6 (a)):

$$I_{\mathrm{NW}}(\theta,\varphi) = I_{\mathrm{dipole}} \left| S(\theta,\varphi) \right|, \tag{3.12}$$

with

$$S(\theta,\varphi) = \sum_{m=1}^{N} \mathrm{e}^{\mathrm{i}(k_{\mathrm{SPP}} - n_2 k_0 \sin\theta\cos\varphi) x_m}. \tag{3.13}$$

The refractive index of the cover glass/objective is n_2, k_{SPP} the plasmon wave-vector, k_0 the vacuum wave-vector, N the number of dipoles and x_m is the spatial coordinate of each dipole along the wire length L . Fig. 3.6 shows calculated BFP patterns for silver

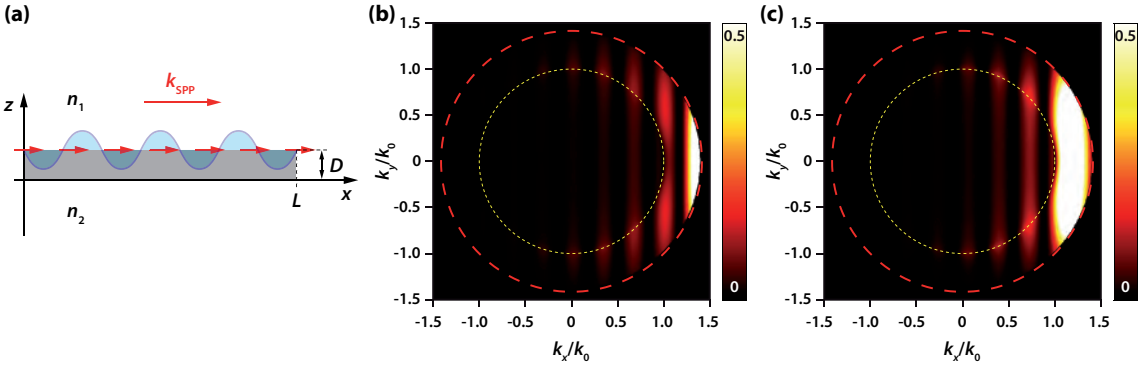

Figure 3.6: (a) Schematic of a single dipole chain connected with a phase (blue indicated wave) for the simulation of SPP propagation along a plasmonic nanowire (k_{SPP}), following the discussion in[19]. (b) Calculated BFP pattern for a 2 µm long silver NW on glass ($n_2 = 1.5$) with a diameter of $D = 50$ nm and (c) $D = 100$ nm. The red dashed circle indicates the maximum collectable angle for a NA = 1.4 objective and the yellow dotted circle the critical angle.

NWs with a length of 2 µm on glass ($n_2 = 1.5$) with a diameter of (b) $D = 50$ nm and (c) $D = 100$ nm. k_{SPP} was calculated according to the diameters with the equation for metal cylinders (eq. 2.19) with air as surrounding medium, using the experimental values for the dielectric function of silver from Johnson and Christy[35]. The main apparent feature of the BFP images is the fringe pattern which results from the dependence of S on the wire length L through the dipole component coordinates x_m and the fact that the NW is a finite

emitter. Since k_{SPP} for thinner wires is larger the maximum of the fringes in fig. 3.6 (b) lies beyond the detectable k-vector range and only higher order fringes are visible. Due to the confinement of the wave-vector into one direction the fringes show no dependency on the coordinate k_y perpendicular to the propagation direction. For the calculation the distance from the interface δ due to the NW diameter D was also considered. The described model was used by Shegai et al. [19] to approximate the SPPs launched by a focused laser on one end of the NW, propagating along to the other end and the experimentally obtained BFP pattern.

4 Emitter Systems

This chapter gives insight into the emitter systems used for emitter-plasmon coupling studied in this thesis. It starts with a description of the structural properties of SWCNTs as rolled up cylinders from a single layer of sp^2 hybridized carbon atoms. Followed up by an introduction of the most important optical properties, resulting from the unique structure of carbon nanotubes, which play a role in the conducted experiments. The second part is dedicated to the structural and optical properties of rare earth doped nanocrystals. Their multitude of accessible electronic states enable particular excitation pathways, such as photon upconversion.

4.1 Single-walled carbon nanotubes (SWCNTs)

SWCNTs are hollow cylinders built up exclusively from sp^2 hybridized carbon atoms. They have a small diameter of down to 0.5 nm, but can be as long as centimeters. Due to the extreme aspect ratio they are often regarded as a quasi one-dimensional (1D) model system. Unique optical and electronic properties resulting from this 1D confinement made applications such as transparent thin-film transistors[128], sensors[129] and photo detectors[130], energy converters and storage[131], LEDs[132–134] among many others, possible.

4.1.1 Structural properties

The unit cell of SWCNTs can be understood as a seamless cylinder rolled up starting from a single graphene sheet. Different nanotube structures are obtained due to different roll up directions of the graphene sheet and are identified by their chirality. Two numbers n and m with $n, m \in \mathbb{N}_0$ are defined as the chiral index usually written as (n, m). The chiral index determines the composition of the circumferential vector $\vec{C}_\mathrm{h}$ out of the graphene lattice vectors $\vec{a}_1$ and $\vec{a}_2$ as indicated in fig. 4.1 for representative examples of a (4,4), (6,0) and (6,5) SWCNTs. The vector addition is expressed by

$$\vec{C}_\mathrm{h} = n \cdot \vec{a}_1 + m \cdot \vec{a}_2 \tag{4.1}$$

while $\vec{C}_\mathrm{h}$ is connected with the SWCNT diameter by

$$d = \frac{|\vec{C}_h|}{\pi} = a\frac{\sqrt{n^2 + m^2 + nm}}{\pi}. \tag{4.2}$$

Three different groups of nanotubes can be distinguished by their chirality: In armchair nanotubes $n = m$, in zig-zag nanotubes one of the two indices equals zero and in chiral SWCNTs $m \neq n$ and $n, m \neq 0$. The length of the unit cell is defined by the translational vector $\vec{T}$

$$\vec{T} = \frac{2m+n}{d_r}\vec{a}_1 - \frac{2n+m}{d_r}\vec{a}_2. \tag{4.3}$$

with d_r as greatest common divisor of $(2m+n)$ and $(2n+m)$[135]. Chiral SWCNTs exist in

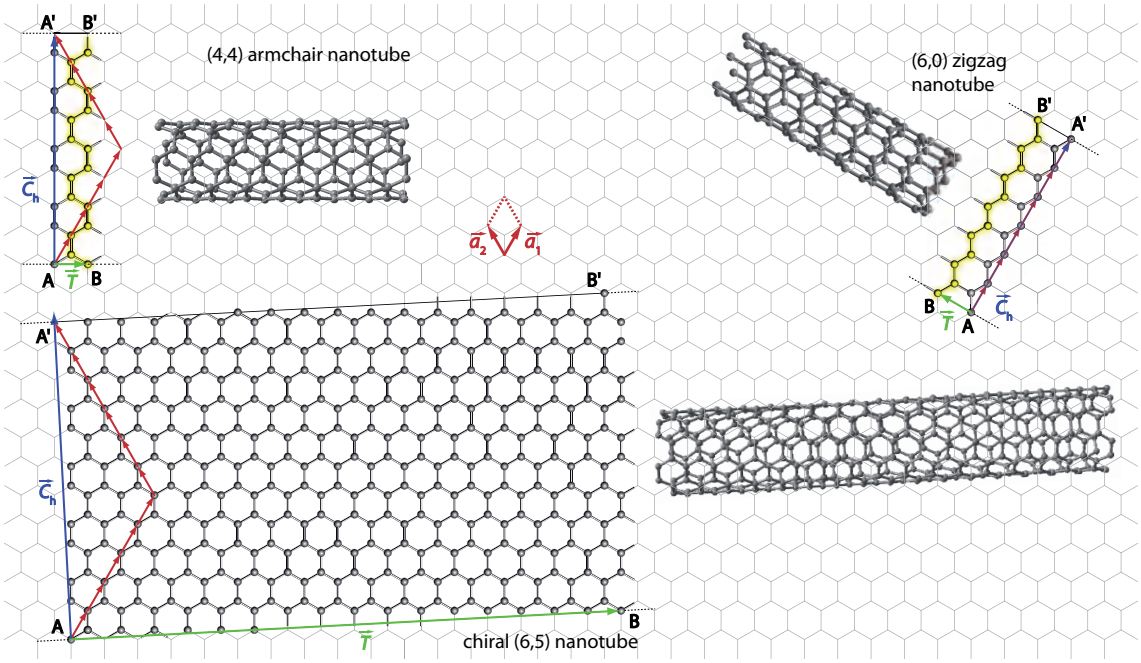

Figure 4.1: Schematic of the unit cell in the graphene lattice for the three different types of SWCNTs: *Armchair* nanotubes with $n = m$, *zig-zag* tubes where $n = 0$ or $m = 0$ and chiral SWCNTs with $n \neq m$ and $n, m \neq 0$. A (4,4), (6,0) and (6,5) nanotube is shown as representative examples. The origin of the name *zigzag* and *armchair* is indicated by the yellow shaded structures. The graphene lattice vectors $\vec{a}_1$ and $\vec{a}_2$, as well as the circumference $\vec{C}_h$ and translation vector $\vec{T}$ are indicated. Adapted from[136].

a right-handed and mirrored left-handed form which are distinguishable by measuring the circular dichroism and separable with different chiral wrapping agents[137,138]. Classification of SWCNTs by the chiral index enables also an easy assignment of their conductance behavior since there are metallic nanotubes with $(n-m)\,mod3 = 0$ and semiconducting nanotubes for any other combination of n and m. In the following, all discussions regarding carbon nanotubes are referring to semiconducting SWCNTs since only photoluminescent semiconducting nanotubes were studied in this work. Apart from this short overview more details can be found in the literature[135,136,139–142].

4.1.2 Optical properties

Due to their direct band gap, semiconducting carbon nanotubes exhibit photoluminescence emission in the NIR to infrared (IR) region. Also strong Raman scattering is observed due to resonance enhancement, comparable to other related carbon materials such as graphene[143] or fullerenes[144].

The basic emission and absorption properties of SWCNTs can be very well approximated by zone-folding the graphene band structure in the context of a free carrier model[142]. The result can be seen in the schematic band structure in fig. 4.2. Transitions over the

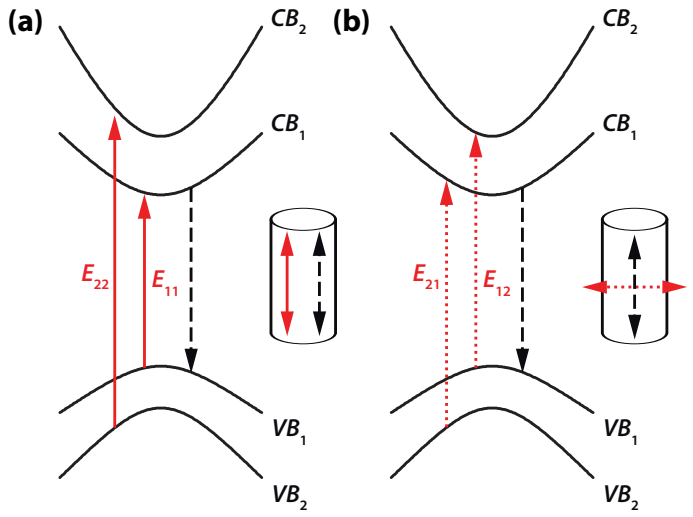

Figure 4.2: Schematics of the SWCNT band structure with a band gap between the highest valence band VB_1 and the lowest conduction band CB_1.(a) shows the dominant transitions E_{11} and E_{22} (red solid arrows) polarized parallel to the nanotube axis together with the emission (black dashed arrow). (b) depicts the less prominent transitions E_{12} and E_{21} polarized perpendicular. The insets illustrate the orientation of the excitation (red arrows) and emission (black dashed arrows) dipole moments and their orientation with respect to the nanotube axis. Adapted from[145]

band gap between the highest valence band VB_1 and the lowest conduction band CB_1, which connect bands with equal indices E_{ii} are polarized parallel to the nanotube axis as shown by the red solid arrows in fig. 4.2 (a). They are the predominant transitions in SWCNTs. Less prominent are the transitions between bands of unequal indices E_{ij} and are polarized perpendicular to the nanotube long axis (fig. 4.2 (b))[145,146]. Relaxation after optical excitation occurs mainly from the lowest conduction band CB_1 into the highest valence band VB_1 and the resulting emitted photon is again polarized parallel to the SWCNT axis (fig. 4.2 (a), (b) black dashed arrows).

Due to the 1D nature of carbon nanotubes the Coulomb interaction between charge carriers can not be neglected. Thus the before mentioned free carrier model needs to be refined by a model of excitons in order to describe the electronic system in more detail. The en-

ergy minimization by the attractive electron-hole interaction results in a bright excitonic state E_{11}^{bright} 300 to 400 meV below the continuum state E_{11}^{∞} [147]. This lowering of the energy is strongly dependent on the magnitude of the exciton binding energy E_{bind} and the counteracting band-gap renormalization energy E_{BGR}. Because of the high surface area of SWCNTs both, the exciton binding energy E_{bind} and the band-gap renormalization energy E_{BGR} are influenced by the dielectric constant of the surrounding environment [148]. Therefore a shift in the PL emission energy can be used to determine the dielectric surroundings of SWCNTs [149–151]. The strongly bound excitons exhibit an exciton Bohr radius on the order of few nanometers and are delocalized along the circumference of the nanotube, but also mobile along its long axis with a diffusion length of about 100 nm [152,153].

A very small Stokes-shift makes it experimentally challenging to separate emitted light and reflected light from the excitation, thus for optical investigations the E_{22} transition is excited. Excess energy between the E_{11}^{bright} state and higher energy states after excitation is rapidly converted non-radiatively and PL emission occurs through relaxation from the E_{11}^{bright} into the ground state [154,155]. Next to radiative recombination of excitons, non-radiative recombination through dark states [156,157] and other decay channels [158] influence the relaxation dynamics, which results in radiative lifetimes of E_{11} states in SWCNTs on the order of several tens or hundreds of ps [159–161]. Thus the resulting quantum yield is in the range of up to 7% for suspended SWCNTs [162] but often lower and is further reduced by quenching through defect sites [163–165].

The energy of the band gap is roughly inversely proportional to the nanotube diameter d. Thus an assignment of the chirality can be conducted upon the analysis of the PL energy. Representative PL spectra for a (6,5), (8,3) and (8,3) SWCNT with emission maxima at about 980 nm, 960 nm and 880 nm [166] are shown in fig. 4.3 (a). The FWHM of the presented emission peaks are between 10 and 30 nm.

Raman spectroscopy provides a well established tool for the investigation of graphitic materials giving access to information on the degree of doping and functionalization [167] but also nanotube specific parameters such as the phonon dispersion [168], length, type and chirality [139]. The resonant Raman condition can be achieved if the excitation wavelength matches a transition energy $E_{ii} = \omega_{\text{ex}}$ or the scattered Raman photon energy matches a transition energy $E_{ii} = \omega_{\text{ex}} - \omega_{\text{phonon}}$. Both, or one of these conditions need to be met to enhance the signal in case of single nanotube detection. Usually the most prominent Raman features are the G band observed between 1500 and 1600 cm^{-1}, a graphite-like band common to all graphitic materials, and the G' band usually located between 2600 and 2700 cm^{-1}. Splitting of the G band into two sub-bands (G^+ and G^-) allows the determination of semiconducting behavior [169]. Another important SWCNT Raman signal is the radial breathing mode (RBM) in the range of 100–400 cm^{-1}, a mode associated with the vibration of carbon atoms in radial direction in relation to the nanotube axis. The RBM shows inverse proportionality to the diameter, the frequency ω_{RBM} is dependent on the direct environment and enables a chirality assignment [170]. The defect-induced D band

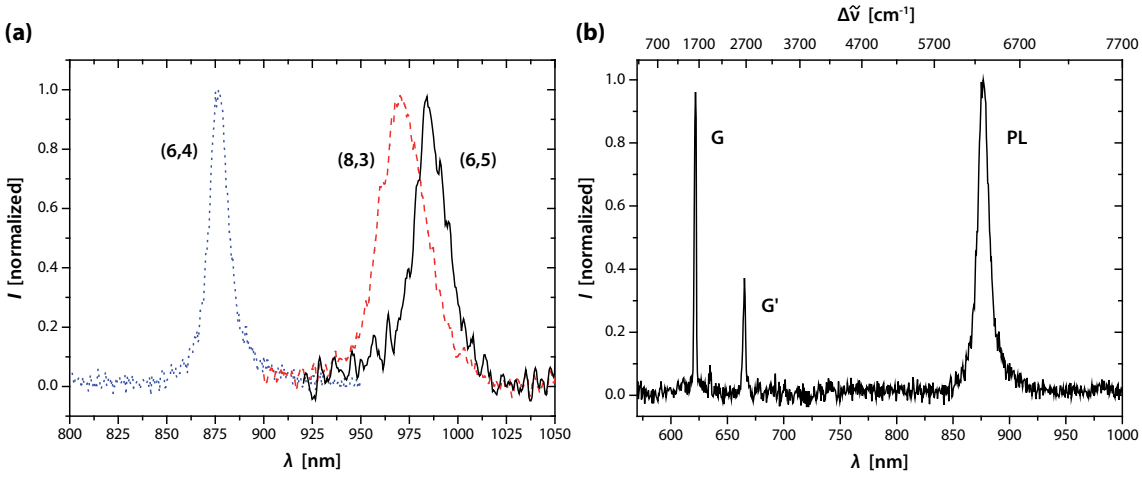

Figure 4.3: (a) PL spectra from three different individual SWCNTs after optical excitation at 565 nm. The emission maximum is situated at about 980 nm for the (6,5) chirality (black solid line), at 960 nm for (8,3) (red dashed line) and at 880 nm for (6,4) SWCNTs (blue dotted line). (b) shows a combined Raman and PL spectrum from an individual (6,4) nanotube. Next to the PL maximum at about 880 nm the prominent G ($\approx 1540\,\mathrm{cm}^{-1}$) and G' ($\approx 2570\,\mathrm{cm}^{-1}$) Raman lines are visible.

at approximately $1300\,\mathrm{cm}^{-1}$ allows for the determination of the defect concentration[171]. A representative combined Raman and PL spectrum of a (6,4) SWCNT is depicted in fig. 4.3 (b) for an excitation wavelength of 565 nm showing the G and G' Raman bands together with the PL signal peaking at 880 nm. There is no obvious D band contribution visible and RBM peaks are not within the detected spectral range.

A more detailed description of the different Raman processes can be found in references[136] and[140].

4.2 Photon upconverting lanthanide doped nanoparticles

The process of photon upconversion is a method to convert long-wavelength excitation light into output radiation at shorter wavelengths. Next to second harmonic generation and two photon absorption[172], upconversion is among the most investigated processes to achieve this phenomenon. Many applications of photon upconversion, such as in lasers[173,174], lighting or displays[175,176] and in labeling and bioimaging[177,178] have been proposed and realized. Advances in the synthesis of monodisperse colloidal nanocrystals, especially for lanthanide doped nanophosphors[179,180], and the ability to control size and shape have made these material systems even more attractive for the investigation and application of upconversion processes.

4.2.1 Structural properties

Upconverted PL could be observed in $NaYF_4$, YF_3[181], $SrCl_2$[182], different ceramic materials[183,184] and fluorohafnate glasses[185] as host materials doped with lanthanide ions such as Yb^{3+}, Er^{3+}, Tm^{3+} and Ho^{3+} or combinations of these. The most efficient upconversion (UC) materials known today are based on fluorides doped with Yb^{3+} and Er^{3+} or Yb^{3+} and Tm^{3+}[186–188]. An important criterion for efficient UC host materials are low phonon energies to minimize the chances for non-radiative multiphonon relaxation processes[187,189]. Lanthanide-doping in these matrices is always accompanied by the formation of crystal defects such as interstitial anions and cation vacancies to maintain charge neutrality. To sustain a single crystal phase of the host for efficient UC, the dopant concentration needs to be rigorously controlled. In order to minimize crystal defects and lattice stress, which further promote non-radiative relaxation processes, host lattices based on cations like Na^+, Ca^{2+} and Y^{3+} with ionic radii close to those of the lanthanide dopant ions, appear to be superior[190]. $NaYF_4$ proved to be the most efficient UC host material and crystallizes in a cubic (α-$NaYF_4$) and a hexagonal (β-$NaYF_4$) structure. Cubic α-$NaYF_4$ crystallizes in the CaF_2 structure type[191] with Na and Y creating a cubic closest packing (ccp) Bravais lattice and F filling all the eight tetrahedral positions as can be seen in fig. 4.4 (a). Thus Na and Y are coordinated by eight F atoms, respectively and F by four Na/Y atoms (gray shaded cube and yellow shaded tetrahedron in fig. 4.4 (a)). The hexagonal phase of

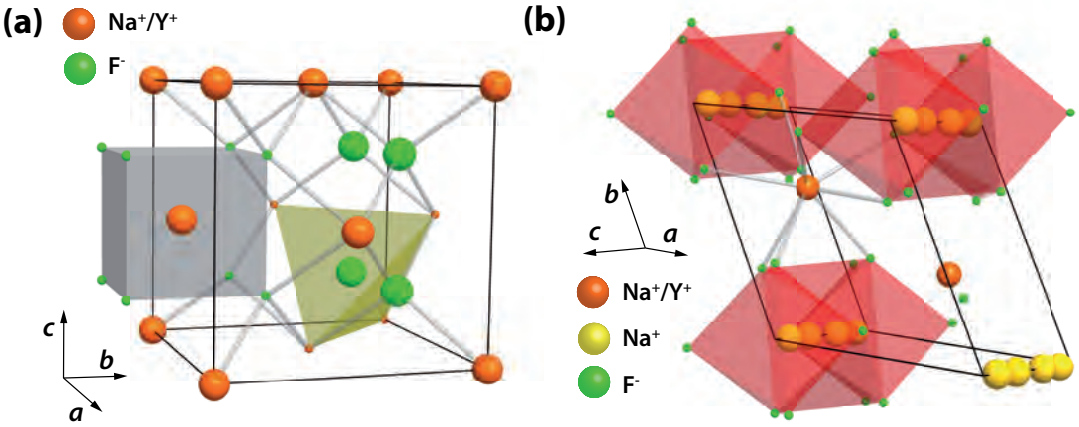

Figure 4.4: (a) Crystal structure of cubic α-$NaYF_4$ with the space group $Fm\bar{3}m$. The structure is based in the CaF_2 structure typ with a ccp Na/Y lattice and F situated in the tetrahedral sites (yellow shaded tetrahedron). Na and Y are coordinated by eight F atoms (gray shaded cube). (b) Crystal structure of hexagonal β-$NaYF_4$ in the space group $P6_3/m$. Sodium ions are situated along the unit cell edges in direction of the c-axis. They are coordinated by eight F atoms which leads to chains of surface connected, distorted octahedra (red shaded octahedra). The coordination octahedra for the lower right Na atoms were omitted to improve the visibility of the structure. Central Na and Y ions are coordinated by nine F atoms.

$NaYF_4$ crystallizes in a structure derivative of the UCl_3 structure with the space group

$P6_3/m$[192] as depicted in fig. 4.4 (b)[193]. In this structure Na ions are situated along the unit cell edges in direction of the c-axis. The coordination by eight F atoms leads to chains of face connected, distorted coordination octahedra (red shaded octahedra in fig. 4.4 (b)). Na and Y ions situated in the center of the unit cell are coordinated by nine F atoms, respectively. For highly efficient UC nanocrystals the dopant concentration of Er should not exceed 3%.

Recent progress in the synthesis of lanthanide doped $NaYF_4$ has made it possible to create colloidal solutions of doped $NaYF_4$ nanocrystals with diameters down to several tens of nanometers. Adjustment of the synthesis conditions leads also to good control of the nanocrystal morphology, which appears in form of spheres, rods, hexagonal prisms and plates[180].

4.2.2 Optical properties

The nonlinear PL phenomena known in the literature as UC[194] in these materials is characterized by subsequent absorption of two or more photons via long-lived intermediate energy states followed by the emission of photons at a shorter wavelength than the initial pump wavelength. The UC process can be divided into three general mechanisms: excited state absorption (ESA), energy transfer upconversion (ETU) and photon avalanche (PA).

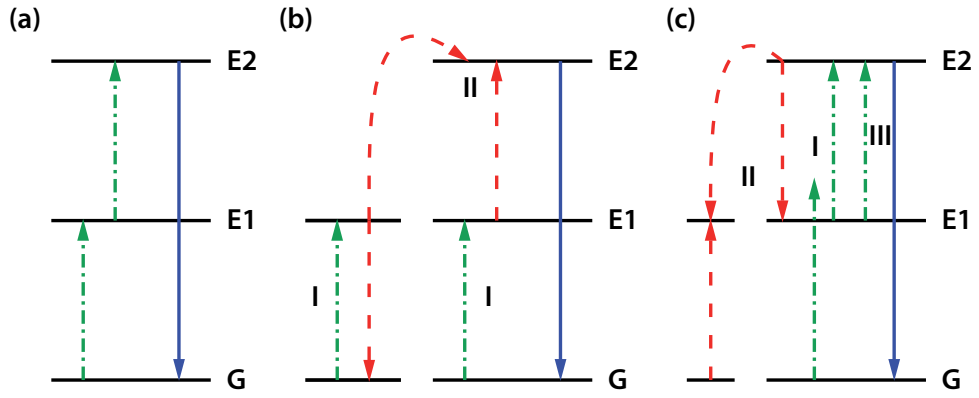

Figure 4.5: Energy diagram of a simplified three level system to visualize three possible UC mechanisms:(a) ESA, (b) ETU and (c) PA. The green dashed dotted, the red dashed and the blue full arrows represent photon excitation, energy transfer and emission processes, respectively. Adapted from[179]

In the case of ESA the absorption of successive photons occurs in a single ion. A schematic energy diagram for a simplified three level system is shown in fig. 4.5 (a). Resonant excitation promotes the ion from the ground level G to the excited metastable level E1 in a process called ground state absorption (GSA). After a second pump photon is absorbed, further excitation from E1 to E2 occurs which results in UC emission according to the $E2 \rightarrow G$ optical transition[179]. Also the process of ETU utilizes the sequential absorption of two photons but the essential difference to ESA is that the second excitation is realized

through energy transfer between two adjacent ions. Each of the two neighboring ions can absorb a pump photon of the same energy, populating in both the metastable level E1 (fig. 4.5 (b) step I). Following a non-radiative energy transfer, one of the ions is promoted to the upper emitting state E2 while the other ion relaxes into the ground state G (fig. 4.5 (b) step II). The efficiency of this mechanism is strongly dependent on the average distance between the neighboring ions and can be influenced by the dopant concentration [179]. PA UC features an unusual pump mechanism requiring a pump intensity above a certain threshold [195]. The first excitation populates E1 by weak non-resonant GSA followed by resonant ESA resulting in the population of the higher excited state E2 (fig. 4.5 (c) step I). Besides relaxing back into the ground state G a cross relaxation to a neighboring ion can occur which results in both ions being in the first excited state E1 (fig. 4.5 (c) step II). If the rate of cross relaxation exceeds the rate for relaxation directly into the ground state G the available number of ions in the excited state for subsequent ESA increases (fig. 4.5 (c) step III) [196]. Fig. 4.6 illustrates the involved optical processes in the example of Yb and Er doped $NaYF_4$ upon excitation in the NIR. ESA occurs in the Er system

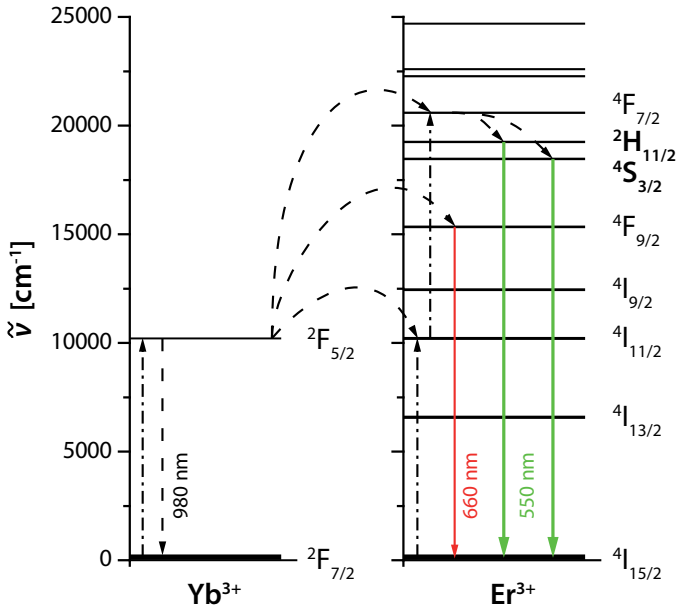

Figure 4.6: Energy diagram for ytterbium and erbium in Yb and Er doped $NaYF_4$ and the involved excitation (dotted/dashed arrows), energy transfer (dashed arrows) and emission processes (solid arrows). Next to the direct excitation of Er in an subsequent two photon process Yb^{3+} can act as an energy transmitter and populate higher excited states in Er^{3+} due to the close proximity in the crystal matrix

after subsequent absorption of two photons with the wavelength of ≈980 nm into the $^4F_{7/2}$ state and is followed by emission from the $^2H_{11/2}$ and $^4S_{3/2}$ levels in the visible (VIS) range (≈550 nm) after internal non-radiative relaxation. The Yb dopant, which is introduced in excess compared to Er, can assist the population of the first excitation in Er ($^4I_{11/2}$) for subsequent ESA by energy transfer but mainly contributes to the ETU process. ETU occurs in this system by energy transfer from the excited state in Yb into either the $^4F_{7/2}$

state of Er connected to the green emission or the $^4F_{9/2}$ level for subsequent relaxation through emission of a red (≈650 nm) photon. The efficiency of all UC processes can be improved by using emitters with a long lifetime of the first excited state. Although, the use of smaller particles makes it necessary to consider additional non-radiative pathways due to the higher fraction of ions in close proximity to the surface[197], common lifetimes are reported on the order of several milliseconds[198].

By selecting suitable dopants and dopant combinations the UC-emission can be tuned from the VIS to the NIR spectral region[199]. A low autofluorescence background, non blinking emission and a very high photostablity[200,201] together with the highly controllable morphology make them useful emitters with a broad range of applications.

5 Experimental details

This chapter is giving an overview of the experimental setups used for the experiments presented in this work, the investigated sample materials and their preparation. The first part gives insight into the optical systems including details of excitation and detection pathways in the utilized microscope as well as a description of the aperture SNOM configuration. The preparation of carbon nanotube, silver nanowire and rare earth doped nanocrystal samples are described in the second part.

5.1 Microscope setup

5.1.1 Confocal microscope

The basis for all used optical setups was an inverted optical microscope (Nikon Eclipse TE2000) equipped with an oil immersion objective featuring a NA of 1.4 (Nikon CFI Planapochromat VC 60x). To allow confocal raster scanning the sample is mounted on a closed loop x,y-piezo stage (Physik Instrumente PI–527). The laser sources used for excitation were semiconductor diode lasers with $\lambda_{ex} = 565\,nm$ (Coherent Sapphire) and $\lambda_{ex} = 980\,nm$ (custom made Spectra-Laser). In order to ensure excitation with only one laser line and to suppress any fluorescence from the laser gain material a narrow bandpass filter (FWHM of 10 nm) with the corresponding central wavelength was placed after each laser source. Confocal excitation was achieved after consecutive beam expansion to a beam diameter of $\approx 10\,mm$ by placing a pinhole with a diameter of 25 µm in the focal spot of the second beam expansion for spatial filtering. The beam diameter was chosen to ensure a slight overfilling of the objective back aperture in order to make use of the full NA of the microscope objective.

Fig. 5.1 (a) and (b) shows a schematic beam path of the available detection methods after confocal excitation. The beam splitter separates the excitation from the detection and needs to be selected according to the excitation wavelength λ_{ex} (dichroic 568 nm from Melles Griot or pellicle 33:67 from Thorlabs). The beam needs to be collimated again by L1 after the intermediate image, which is created by the tube lens integrated in the microscope body, and can be focused subsequently (L2) on the pixel array of a charge coupled device (CCD) camera (Andor Newton or Andor iDus) for wide-field real-space imaging. Focusing (L2) on the chip of an avalanche photo diode (APD) (Laser Components COUNT 100 or

COUNT 200) and simultaneous raster scanning of the sample enables the detection of confocal scanning images. As a third alternative detection mode a spectrometer can be used by focusing into the entrance slit of a compact optical spectrometer (Andor Shamrock 303i). The fourth detection method is the imaging of BFP patterns as shown in fig. 5.1 (b),

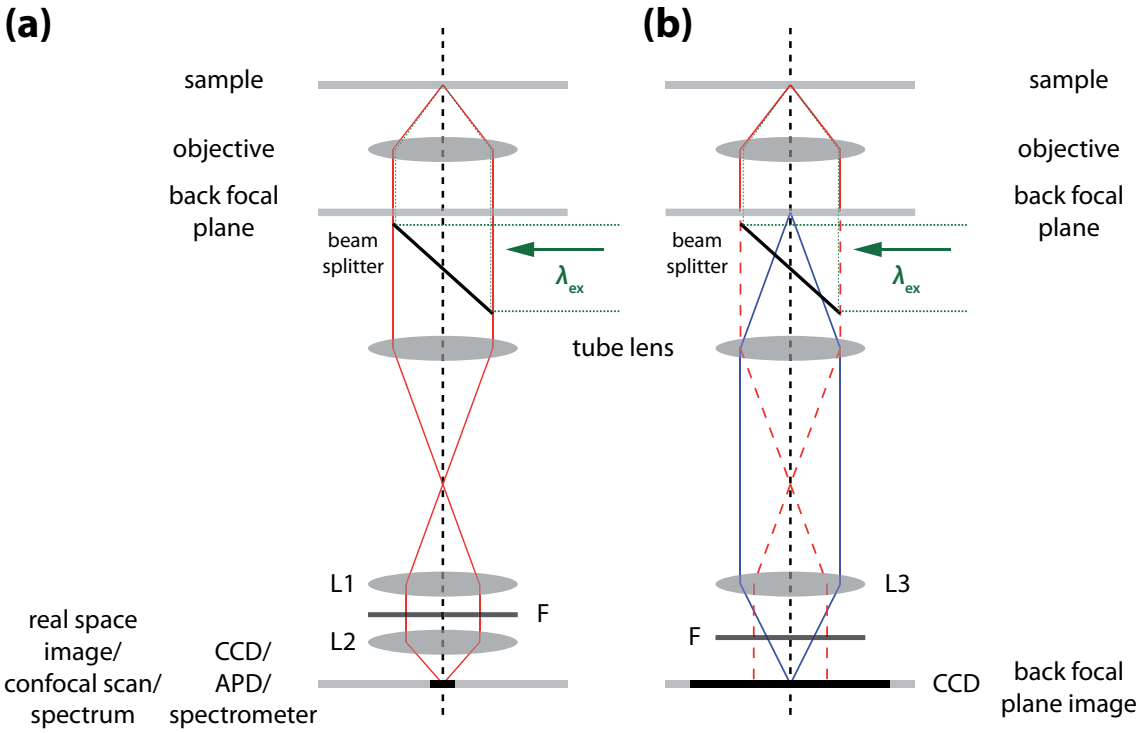

Figure 5.1: Schematic of the optical setup. Four different imaging and detection methods are available after confocal laser excitation at $\lambda_{ex} = 565$ or 980 nm: (a) Real space imaging by a CCD camera, scanning confocal detection using an avalanche photo diode (APD) and spectroscopy at the current position. After collimation (L1) the lens L2 focuses the signal onto the CCD array, APD chip or the spectrometer entrance slit. (b) Fourier (BFP) imaging by a CCD camera. Together with the tube lens, the lens L3 projects the BFP onto the detector array. An optical filter F can be placed optionally in all detection methods to filter the desired spectral region.

where the lens L3, together with the tube lens, project the Fourier plane onto the CCD camera. Details of the Fourier plane imaging can be found in section 5.1.2

In the case of real-space imaging, BFP imaging or confocal scanning the desired detected spectral range can be chosen by the placement of different optical filters F: For the investigation of SPPs launched by SWCNT emission in chapter 6 a 950 nm long-pass was chosen. To filter for a broader selection of chiralities a 860 nm long-pass was used for the plasmon excitation of SWCNT emission in chapter 7. One distinct emission band of the rare earth doped nanocrystals (NCs) was selected by a band-pass filter centered at 670 nm with a FWHM of 10 nm in the experiments presented in chapter 8.

5.1.2 BFP imaging

As described in chapter 3 a map of the angular distribution of emission created in the BFP of a lens contains a lot of information on the emission characteristics of the observed object. In order to record this BFP pattern in the case of a microscope one can use the fact that every lens creates a Fourier transformation of the image in the focal plane behind the lens, again with the distance of the focal length[113,202]. It has to be noted that the limited lens diameter corresponds to a filtering of k-vectors larger than $k_{\max}$. Although this leads to image distortions, which influence the exact image, they do not contradict the demonstrated principle of the image formation. Usually, the first Fourier plane of the objective lens (OL in fig. 5.2) is not directly accessible since it is situated inside the objective barrel in the case of most commercially available objectives. The used microscope contains a tube lens (TL) inside the microscope body which creates an intermediate image (image plane') for access through the oculars. This intermediate image can be used to

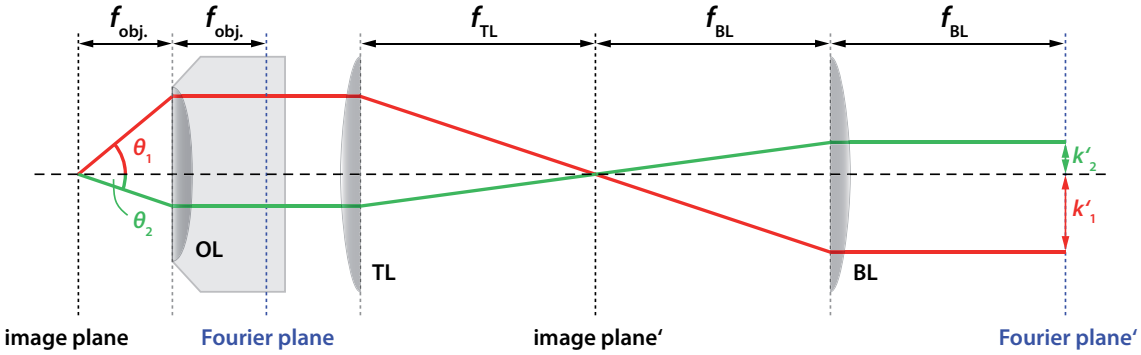

Figure 5.2: Schematic of the beam path in order to image the BFP of a microscope objective. The two rays with different radiation angles θ_1/θ_2 are collected by the objective lens (OL, focal length $f_{\text{obj.}}$) and are projected onto the Fourier plane inside the objective barrel. After the image plane' is recreated by the tube lens (TL, focal length f_{TL}) the Bertrand lens (BL, focal length f_{BL}) forms again the Fourier image' which can be recorded by a detector. The emission angles θ_1/θ_2 are connected with the wave-vectors k'_1/k'_2 in Fourier space according to eq. 3.4.

create a second Fourier image by positioning a Bertrand lens[13] (BL) at the exact distance of its focal length to the intermediate image. Thus a detector placed at the distance of the focal length f_{BL} to the Bertrand lens is able to record the BFP of the initial image in the focal plane of the microscope objective. The setup of the tube lens together with the Bertrand lens is also called in the literature $4f$-configuration or -correlator[203]. By using two consecutive $4f$-configurations it is possible to create an intermediate Fourier plane which is accessible to place adequate beam stops and masks for Fourier filtering or selection of specific spatial frequencies[204]. This is conceptually comparable to dark-field imaging in TEM[205] or Fourier filtering in the context of image or signal processing[206]. It is important to note that the here described and used configuration is creating the BFP image out of all collected light in the field of view of the objective. In order to limit the

pattern to a confocal detection volume a pinhole can be placed in the intermediate image plane between tube lens and Bertrand lens (fig. 5.2).

5.1.3 Aperture scanning optical near-field microscopy (SNOM) configuration

Aperture SNOM is a near-field microscopy technique which enables optical excitation and collection from a confined region at the end of an aperture fiber tip. Usually, the fiber is coated with a metal film in order to prevent light from leaking out of the fiber. The aperture SNOM can be used in collection mode, excitation mode or a combination of both[33]. In excitation mode the tapered fiber is used to channel down the light coupled into the fiber at the long end and confine it to a small excitation volume where evanescent waves reach only a few nanometers beyond the tip end.

The before described confocal system can be equipped with a home built head for shear-force detection used for atomic force microscopy (AFM), which gives the possibility to keep an aperture tip or glass tip within a constant distance of only several nanometers from the sample surface. Commercial aluminum coated aperture probes (Lovalite) with a

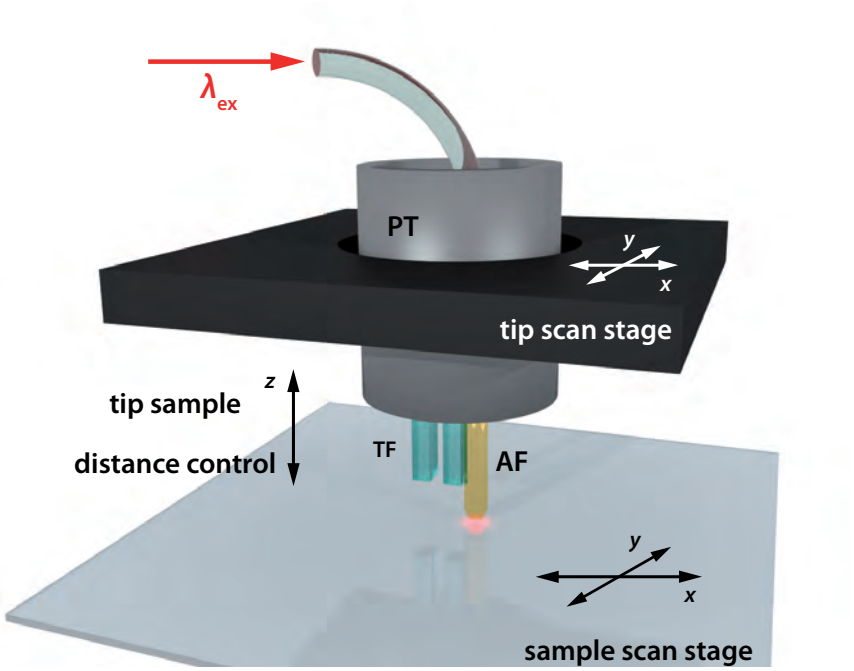

Figure 5.3: Schematic of the aperture SNOM configuration. The aperture fiber (AF) is mounted to the tuning fork (TF) and excited with a HeNe laser at $\lambda_{ex} = 633\,\text{nm}$. Besides the scan motion from the basic confocal setup the tip scan stage can move the tip position relative to the sample. The tip sample distance control is enabled by a SPM controller regulating upon the frequency shift of the tuning fork together z-piezo tube (PZ).

nominal aperture diameter of 70 nm for aperture SNOM measurements and home etched

glass fiber tips for AFM investigations were mounted to a quartz tuning fork (TF) at the end of a z-piezo tube (PT), as depicted in fig. 5.3. The tip sample distance control is regulated by a commercially available SPM controller (attocube ASC500) using a phase-locked-loop (PLL), constantly monitoring the resonance frequency of the tuning fork. To ensure a constant oscillation, the tuning fork is driven by a dither piezo, mounted in close range, with a variable frequency f. Three feedback loops are applied to keep the tip at a constant distance with respect to the sample surface: The amplitude of the tuning fork resonance maximum is held constant by a first proportional-integral (PI) feedback loop which regulates the driving amplitude of the dither piezo. A second PI loop is controlling the driving frequency f_{d} of the dither piezo in order to keep the phase of the resonance at a constant value. The actual distance between tip and sample surface is then controlled by a third PI loop which regulates the voltages leading to the z-piezo tube by comparing the frequency shift between the undisturbed system and the system under the influence of forces originating from the surface in close range. A more detailed description of the distance control can be found in the reference by Georgi [136]. In contrast to the system described by [136] the lateral displacement of the tip was achieved by mounting the z-piezo tube inside a x/y-scan stage similar to the sample scan stage in fig. 5.3. Using aperture SNOM tips as probes requires much more attention to the mechanical stability of the fiber end reaching out of the scan head. Every mechanical contact has a large influence on the resonance frequency of the tuning fork, hence the lateral tip displacement by a x/y-piezo tube was not applicable.

5.2 Sample preparation and configuration

5.2.1 SWCNTs samples on multilayer thin films

Samples of SWCNTs were prepared from raw commercially available powder, produced using cobalt-molybdenum catalyst (CoMoCat) particles [207,208] and the high pressure carbon monoxide (HiPCO) method [209,210]. Besides the presence of many different chiralities upon synthesis [211] CoMoCat material shows an excess of (6,5) SWCNTs, next to smaller amounts of (6,4), (8,3) and (9,1) SWCNTs. Whereas HiPCO SWCNTs exhibit a rather uniform distribution of these chiralities and in general a larger diameter and chirality distribution. The interest in these specific chiralities is their emission wavelengths which are situated in the still detectable range of the used silicon detectors and the excitation with the used laser sources is readily possible (see section 5.1). Since raw SWCNTs are not soluble in water and are forming bundles due to the strong van der Waals forces interacting between the nanotube sidewalls, they are brought into solution with the aid of surfactants. These surfactants enclose the nanotubes in a micelle due to the non-polar part and arrange the contact with the surrounding solvent through their polar part. Frequently

used surfactants for dissolving SWCNT are e.g. sodium dodecyl sulfate (SDS)[163], sodium cholate (SC)[212] and sodium deoxycholate (SDC)[213] among many others[214].

One milligram of raw HiPCO (Unidym Inc.) and one milligram CoMoCat (Sigma-Aldrich Inc.) SWCNTs per mL wt% SDC solution in water were each dispersed by sonication over 3 h (Bandelin Sonopuls HD2200/UW2200) at the lowest power setting and constant ice cooling. After subsequent centrifugation to remove remaining bundles, the supernatant solutions were used to be spin-coated on top of multilayer metal/dielectric sample substrates.

All the experiments in chapter 6 were conducted with HiPCO SWCNTs spin-coated onto metal/dielectric multilayer samples provided by the group of Dr. Alexandre Bouhelier (Universiteé de Bourgogne, Dijon, France). The samples consisted of a 25 nm gold film evaporated on standard microscope cover slides (borosilicate glass D 263^{TM}, Marienfeld GmbH). The thickness of the cover glasses was between 130 and 160 µm and they feature a refractive index of $n_D = 1.52$ at 589 nm. On top of the gold film SiO_x spacer layers with different thicknesses of 8, 10, 15, 28 and 35 nm were evaporated.

The multilayer sample substrate used in the experiments presented in chapter 7 were provided by the group of Prof. Ulf Kleineberg (Ludwig-Maximilians-Universität München, Germany). Featuring a 20 nm gold film evaporated on top of the same microscope cover glasses with an additional 20 nm SiO_x spacer layer. Solutions of CoMoCat SWCNTs were spin-coated on top.

5.2.2 Silver nanowires and rare earth nanocrystals: sample preparation

Silver nanowire material was synthesized in the group of Prof. Sebastian Mackowski (Nikolaus Copernikus University, Torun, Poland) using a solution based polyol process[215,216]. $AgNO_3$ is reduced by ethylene glycol in the presence of copper nanoparticles and polyvinylpyrrolidone (PVP) in heated solution at 160°C. The copper nanoparticles act as growth seeds and the PVP is channeling the growth along one direction by stopping the nanowire to grow in diameter through creation of micelles. At the same time aggregation of several NWs is prevented by the PVP. With this method silver NWs up to 50 µm in length and a rather broad diameter distribution from 20 nm to 300 nm[217] are obtained. Fig. 5.4 (a) shows a representative SEM image of a silver NWs together with a more detailed micrograph of two inter-crossing NWs in fig. 5.4 (b).

Rare earth doped NCs were synthesized in the group of Prof. Paras N. Prasad (State University of New York, Buffalo, NY, United States of America). The used NCs consisted of $NaYF_4$ doped with 20 wt% ytterbium and 2 wt% erbium. $NaYF_4$ NCs were obtained by thermolysis of yttrium-tri fluor acetate (TFA), ytterbium-TFA, erbium-TFA and sodium-TFA precursors[218,219]. With this method doped NCs with a size distribution of 25-30 nm were obtained[178]. Fig. 5.5 shows a representative emission spectrum of a single NC after

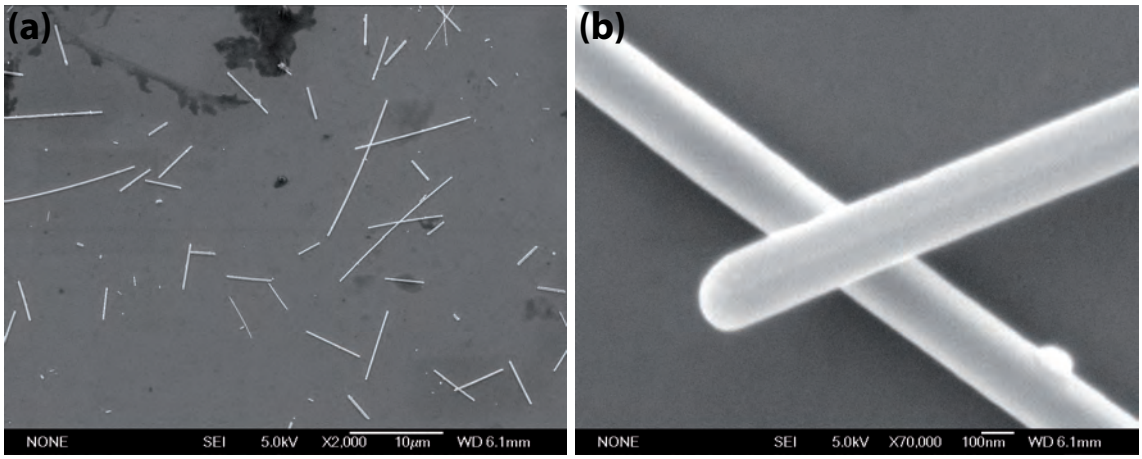

Figure 5.4: (a) SEM micrograph of silver NWs. The scale bar represents 10 µm. (b). Detailed SEM micrograph with larger magnification of two silver NWs inter-crossing. The scale bar represents 100 nm.

excitation with 980 nm, featuring two distinct emission bands with maxima around 550 and 660 nm. These main emission bands can be assigned to relaxations in the doped Er ions after UC excitation indicated in fig. 4.6 in section 4.2.2 as green and red solid arrows. Several electronic levels contribute to the emission bands resulting in several visible sub-peaks. Based on the cubic lattice structure of the used $NaYF_4$ host crystal, as shown in fig. 4.4 (a) in section 4.2.1, and the dopant concentration of 2 wt% emitting Er ions the

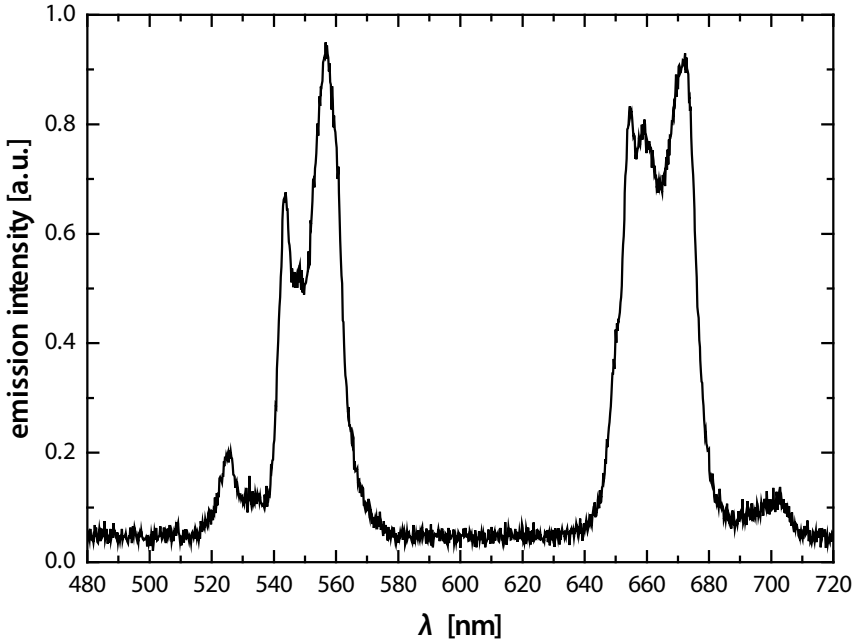

Figure 5.5: Emission spectrum of $NaYF_4$ doped with 20 wt% yttrium and 2 wt% erbium. Two emission bands at about 660 and 550 nm are visible. The sub-peaks are caused by several energetic closely situated bands contributing to the emission (see also section 4.2.2)

number of emission centers in a single crystal, with a diameter of 20 nm (50 nm), can be estimated to be about $\approx$ 600 (9200).

To prepare combined samples, a droplet of the silver NW solution was spin-coated on a standard microscope cover glass (Marienfeld GmbH). Doped NCs were spin-coated in a second step on top of the nanowire sample.

6 Launching SPPs by SWCNT emission

This chapter is based on the article "Launching Propagating Surface Plasmon Polaritons by a Single Carbon Nanotube Dipolar Emitter" which was published in *Nano Lett.* **2012**, *12*, 177.

As presented in chapter 2, direct excitation of SPPs with propagating light is not possible and different schemes coupling laser light to SPPs have been developed. Since for nanophotonic applications device miniaturization and integration of optics and electronics on a single chip is desirable, different methods were proposed to excite SPPs through emission from dye molecules[56–61] or semiconductor nanocrystals[62–64]. Despite the possible integration into circuitry, electrical contacting and excitation of such single SPP sources, however, would be extremely challenging and external optical pumping would still be required. Ideally, SPP sources would operate in the NIR spectral region to exploit the long propagation length of plasmons in this regime and to minimize losses as described in section 2.2. Moreover, efficient coupling of SPPs to functional elements, for example for focusing[91,220] refraction[221] and guiding[26] requires the directional excitation of plasmons.

In the following the description of directional excitation of propagating surface plasmon polaritons on a thin metal film by individual single-walled carbon nanotubes is investigated. Upon laser excitation in the visible photoluminescent SWCNTs launch SPPs in the NIR propagating for several micrometers predominately in the direction of the nanotube axis. SPP excitation and propagation are investigated by leakage radiation microscopy, introduced in section 2.4.1, in real and Fourier space. Polarized radiation patterns recorded for single SWCNTs on gold films reveal an almost complete redistribution of the angular emission with respect to SWCNTs on glass, resulting in highly directive PL emission lobes. The observed emission characteristics of the nanotubes are also in marked difference to the case of coupling to localized radiating surface plasmons in a sharp metal tip antenna[105]. Rigorous model calculations of spatial intensity distributions and radiation patterns show that plasmon excitation results from radiating point dipole sources. The observed directionality and long propagation length together with the well-controlled emission spectra of SWCNTs and the possibility of electrical excitation of emission[222,223] makes them promising candidates as functional elements in nanophotonic devices.

6.1 Emission characteristics of single SWCNTs on a thin gold film

A solution of dispersed HiPCO nanotubes prepared as described in section 5.2.1 was spin-coated onto a 25 nm gold film evaporated on a microscope cover glass, with an additional 35±5 nm SiO_x spacer layer on top. The dielectric spacer layer was introduced to prevent quenching of the SWCNT PL via coupling to non-radiative lossy modes in the metal [93,224]. The used microscope and detection methods of scanning confocal, real space and back focal plane detection are described in section 5.1 (fig. 5.1). For all detection methods in this chapter a 950 nm longpass was chosen which, together with the diminishing detection efficiency of the CCD camera and APD above 1010 nm, limits the detected spectral window to select the emission of (6,5) SWCNTs.

As a first step the samples were imaged by scanning confocal PL microscopy to locate (6,5) SWCNTs. A representative PL image is shown in fig. 6.1 (a). The SWCNTs appear in the confocal image as diffraction-limited luminescent spots. This is expected since the raw

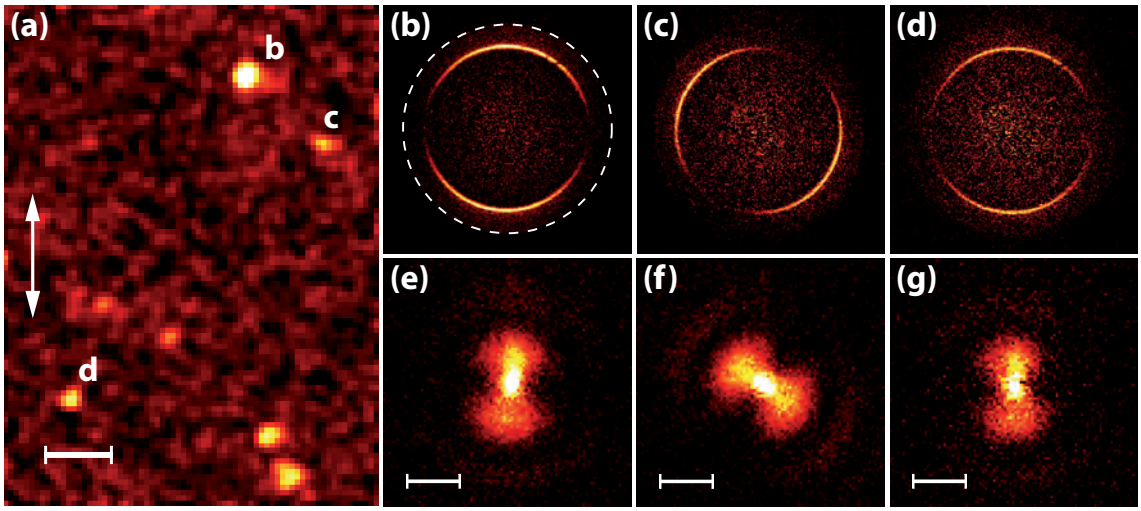

Figure 6.1: (a) Confocal PL image of single SWCNTs on a 35 nm SiO_x spacer layer on top of a 25 nm gold film. The scale bar represents 2.0 µm. The laser polarization, indicated by the white arrow, selects mainly nanotubes with vertical orientation. Launching of SPPs upon local laser excitation is shown for three SWCNTs marked in (a) by b, c and d. In the Fourier (k-) space images of these nanotubes ((b)-(d)) SPP excitation renders sharp arcs formed by photons with in-plane momentum k_x matching the plasmon momentum k_{SPP}. In the corresponding real space images ((e)-(g)) SPPs propagation leads to a double lobe structure extending several microns away from the central excitation spot. The scale bar represents 4.0 µm. The same directivity of plasmon excitation is seen in the corresponding Fourier and real space images ((b) and (e), (c) and (f), (d) and (g), respectively). Plasmons are launched predominately in the direction of the SWCNTs.

material contains rather short nanotubes that are cut further by sonication [225–227] with typical lengths in the range of 500 nm [157]. Next, BFP radiation patterns (fig. 6.1 (b)-(d))

and real space image (fig. 6.1 (e)-(g)) of each SWCNT, identified in the PL image, were recorded . The most prominent characteristic of the Fourier plane images (fig. 6.1 (b)-(d)) is the confinement of the emission to a very narrow angular range. The observed rings are the signatures of plasmons radiating into the substrate[228]: The radius of the rings is determined by the resonance condition between SPPs bound to the SiO_x-gold interface and photons in the lower half-space with higher refractive index ($n_{\mathrm{oil/glass}}$). Due to momentum conservation plasmons can only couple to photons with equal in-plane momentum $k_{\mathrm{SPP}} = k_x$. The fact that the rings are not continuous and only bright arcs are observed originates from a polarized excitation source, demonstrating the directional excitation and propagation of the SPPs. Directional propagation of the SPPs is even more evident in the corresponding real space images (fig. 6.1 (e)-(g)) recorded at the same positions which show elongated spatial distribution of the emission indicating a propagation length of several micrometers. For nanotubes the strongest optical transitions as well as the PL are polarized along the nanotube axis, as discussed in section 4.1.2. Since the polarization of the exciting laser was vertical, as indicated by the arrow in fig. 6.1 (a), mainly SWCNTs oriented parallel to this direction could be excited efficiently and are observed. From both real and Fourier space images in fig. 6.1 we can thus conclude that SPPs are launched mainly in the direction of the SWCNT axis. In addition, no horizontally oriented real and Fourier space patterns could be detected which is a clear indication that nanotube orientation and plasmon propagation direction coincide.

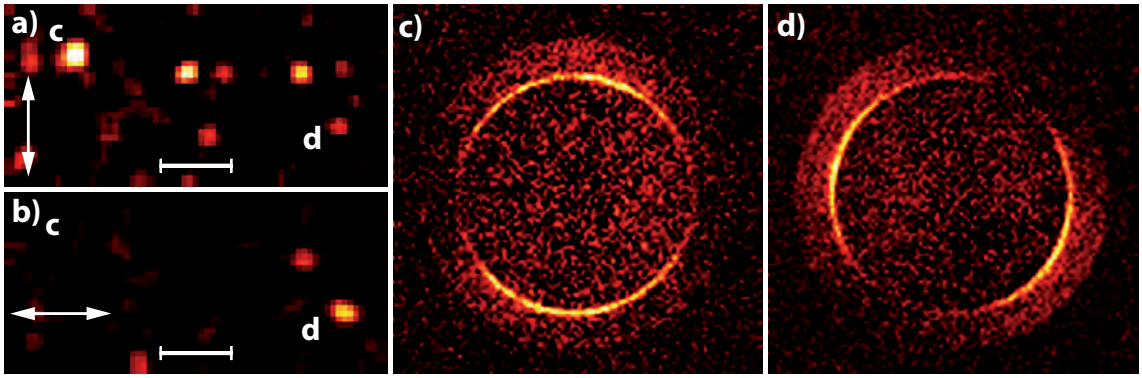

Figure 6.2: Confocal PL images of randomly oriented nanotubes on a dielectric/gold substrate recorded for vertical (a) and horizontal excitation polarization (b) as indicated by the direction of the arrows (scale bar 2 µm, same intensity scaling).(c) and (d) show the radiation patterns detected at the respective positions c and d marked in (a) and (b). The nanotube at position c that is excited only for vertical polarization is seen to launch propagating surface plasmons mainly in the same direction. In contrast, the nanotube at position d shows a stronger PL response for horizontal polarization and correspondingly, plasmon excitation occurs mainly in horizontal direction. The lower polarization contrast observed in the confocal images at position d results from the non perfect horizontal orientation of this nanotube.

To further confirm the relative orientation between a nanotube and the SPP propagation direction confocal scans and subsequent BFP patterns with two perpendicular excitation

polarizations were measured. Two confocal PL scans on the same sample area are shown, recorded with vertical excitation polarization in fig. 6.2 (a) and horizontal excitation polarization in fig. 6.2 (b). Two selected SWCNTs marked with c and d in both images are compared. At position c the nanotube is efficiently excited by light with vertical polarization (fig. 6.2 (a)) and shows no emission after excitation with horizontally polarized light (fig. 6.2 (b)). Nanotube d is visible in both images but with much higher signal to noise ratio after excitation with horizontally polarized light, which is evidence for a slightly rotated orientation of the nanotube with respect to the horizontal axis. The different emission contrast is due to the before mentioned orientation of the main contributing optical transitions in SWCNTs. BFP images recorded at both positions confirm these findings and show a pattern oriented with the two bright arcs in the direction of the vertical axis in the case of nanotube c (fig. 6.2 (c)) and a by ≈85° rotated pattern in the case of nanotube d (fig. 6.2 (d)). Again, this supports the assumption that SPPs launched by the SWCNT emission are propagating in the direction parallel to the nanotube axis.

Another method to confirm the relative orientation of the SWCNTs with respect to the SPP propagation direction is the comparison of BFP patterns with the actual SWCNT orientation measured by AFM. On top of the confocal microscope a home built shear-force AFM head equipped with an etched glass fiber tip ,as described in section 2.4.2, was placed. After overlapping the glass tip with the confocal laser spot the system is able to record AFM topography information in the same sample area mapped confocally. Fig. 6.3 (a) Depicts a confocal PL map together with a magnified topography scan (b) showing the two luminescent SWCNTs at the positions c and d. The identification of

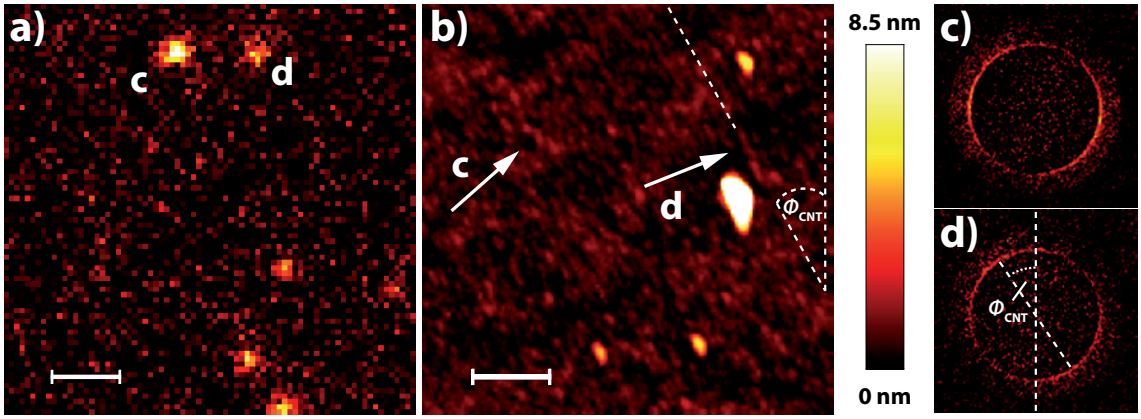

Figure 6.3: (a) Confocal PL image of nanotubes on a dielectric/gold substrate (scale bar 1 µm). (b) Atomic force microscopy topography image showing the two photoluminescent nanotubes at positions c and d marked by arrows in (a) (scale bar 300 nm). The identification of the thin nanotubes with diameter of around 0.8 nm is somewhat hindered by the surface roughness of the SiO_x spacer layer. In the present case the identification is supported by the comparable nanotube position and separation seen in the PL and the AFM image. The radiation patterns recorded for the two differently oriented nanotubes at position c and d are shown in (c) and (d). The orientation of the nanotubes Φ_{CNT} coincides with the direction of the plasmon excitation seen in (c) and (d).

the thin nanotubes with diameters of around 0.8 nm is somewhat hindered by the surface roughness of the SiO_x spacer layer but is supported by the comparable nanotube position and separation seen in the PL and the AFM image. Subsequently, BFP patterns were measured at the same positions (fig. 6.3 (c) and (d)), which show the direction of plasmon propagation coinciding with the nanotube orientation Φ_{CNT}.

6.2 Theoretical simulation of single dipole BFP and real space patterns on a metal film

In order to quantify the plasmon propagation length L_{D}, the plasmon wave-vector k_{SPP} as well as to examine the mechanism of plasmon excitation BFP patterns and real-space images were modeled theoretically. Fig. 6.4 illustrates the geometry applied in the theoretical calculations. The SWCNT, treated as a single dipolar emitter $\vec{p}_{\mathrm{CNT}}$ [105,111], is situated

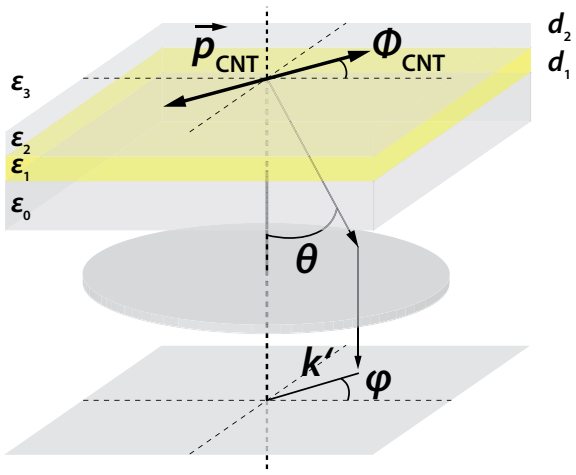

Figure 6.4: Schematic of the sample geometry and coordinate system for the calculation of real and Fourier space images from a SWCNT single dipole situated on a spacer/gold film (ε_2, d_2 and ε_1, d_1). The nanotube is surrounded by a dielectric medium (ε_3) and the gold film is connected to the coverglass/objective (ε_0).

on top of the SiO_x layer (ε_3) with the thickness d_2 surrounded by air (ε_3). Underneath the spacer layer the gold film (ε_1) with a thickness of d_1=25 nm is located, connected to the half-space made up by the microscope cover glass, the immersion oil and the objective lens (ε_0). An asymptotic expression for the surface plasmon fields for a single in-plane dipole is given in [15,18,229] as

$$E\left(\left|k'\right|,\varphi\right) \propto \cos(\varphi)\frac{1}{\sqrt{r}}E_0 e^{\mathrm{i}\left(k_{\mathrm{SPP}}+\mathrm{i}\frac{1}{2L_{\mathrm{SPP}}}\right)|k'|}. \tag{6.1}$$

The Fourier pattern rendered by a single dipole can then be calculated directly as the modulus square of the Fourier transform of eq. 6.1. Since no analytical expression for the

Fourier transform of eq. 6.1 is available, a Lorentzian line shape function can be used as an approximation for fitting of the experimental data[230]:

$$I\left(\left|k'\right|,\varphi\right) = y_0 + I_0 \frac{\cos^2\left(\varphi - \Phi\right)}{\left(\left|k'\right| - k'_{SPP}\right)^2 + \left(2L_{\mathrm{SPP}}\right)^{-2}} \tag{6.2}$$

Here y_0 denotes the contribution of a potential background, I_0 is the amplitude, Φ is the in-plane orientational angle of the dipole corresponding to the direction of the SWCNT, k'_{SPP} determines the position of the maximum of the emission ring corresponding to the plasmon resonance condition $k'_{\mathrm{SPP}} = k'_x$ and L_{SPP} is the propagation length of the SPPs. Fig. 6.5 shows a comparison between cross-sections from the intensity of the numerical Fourier transform of the asymptotic expression (eq. 6.1) and the Lorentzian approximation (eq. 6.2), both calculated in the direction along the nanotube long axis ($\varphi = \Phi$). For

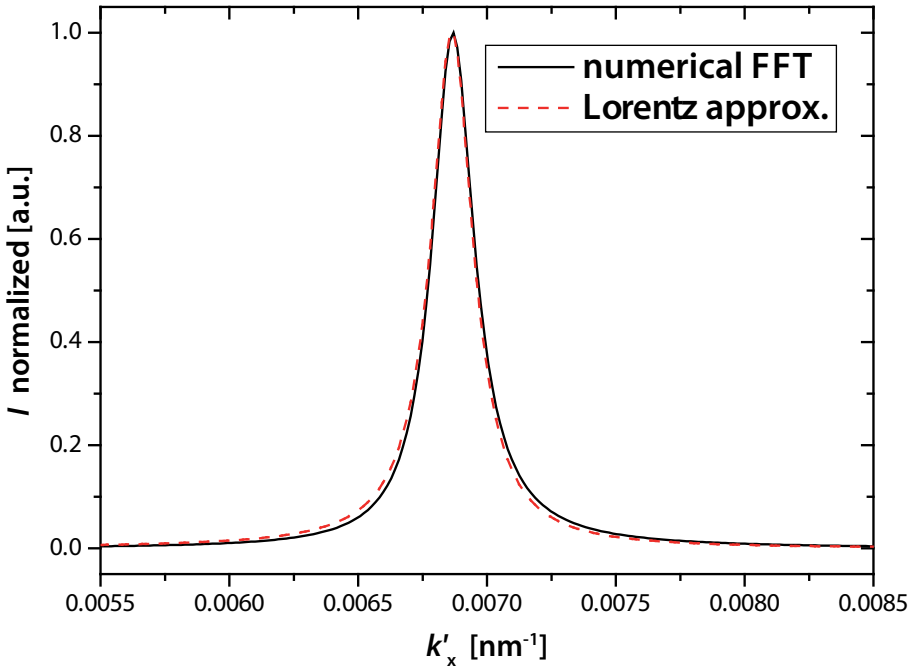

Figure 6.5: Comparison of the modulus square of the numerical Fourier transform of the asymptotic plasmon field (eq. 6.1) according to[18] and a Lorentzian line shape function (eq. 6.2) using the same plasmon propagation length L_{D}. The curves represent cross-sections obtained for $\varphi = 0$ and $\Phi = 0$. The Lorentzian line shape function represents a good approximation regarding both peak position and peak width.

the simulation in fig. 6.5 k'_{SPP} was calculated for the given sample geometry according to the formula for a multilayer geometry with a transparent coating (eq. 2.9) and L_{D}. Despite small differences at the base of the peaks the Lorentzian line shape function represents a good approximation for the intensity distribution of a single dipole in the BFP. Especially the peak maximum and the FWHM, which are important for the determination of $k'_{\mathrm{SPP}}/\theta_{\mathrm{SPP}}$ and L_{D} are very well reproduced.

Real space images of single dipole emitters were calculated by Fourier transformation of the angular spectrum of the electromagnetic field at the gold/glass interface created by

a single in-plane dipole considering the imaging properties of the used microscope. First, the electric fields from a single dipole propagating through the multilayer geometry is considered by a plane wave expansion across the different interfaces including evanescent waves which are converted into propagating waves for angles larger than the critical angle[231]. The fields are split up into *s*- and *p*- components to be treated by a multilayer Fresnel transmission coefficient. Further propagation into the far field and the creation of the image by a focusing lens onto the detector was calculated according to Tang et al. [115]. To obtain the good agreement between calculated and experimental image a defocus of

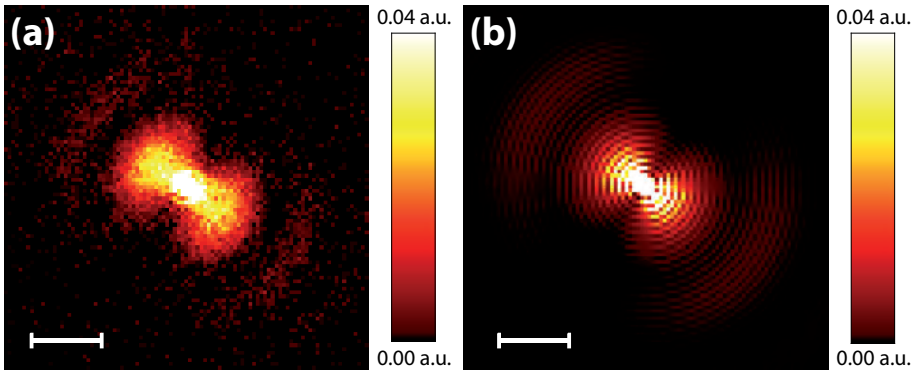

Figure 6.6: Experimental (a) and theoretical (b) real space image rendered by a single in-plane dipole and dected by the CCD camera. The scale bar represents 4.0 µm in both images.

the imaging system corresponding to a shift of 130 µm of the CCD camera needed to be included. This positioning error is within the mechanical and optical tolerances of the used alignment procedure, wile the focusing of the microscope objective on the sample surface is, on the opposite, much more precise. In general the calculation reproduces all of the features of the experimental image. Imprecisions in the background correction, needed to remove residual laser light passing through the spectral filter, can explain the fact that a strong central peak is observed in the experiment that does not appear in the calculation. Importantly, in real space images contributions from emission channels other than those mediated by SPPs such as direct emission through the layer structure appear at the same central location and thus cannot be distinguished clearly. This underlines the advantages of BFP imaging in which SPPs appear as characteristic narrow arcs in fig. 6.7.

6.3 Determination of the propagation length and plasmon wave-vector from leakage radiation BFP patterns

BFP patterns from nanotubes on samples with different spacer thicknesses of $d_2 = 8$, 10, 15, 28 and 35 nm and constant metal thickness ($d_1 = 25$ nm) were measured. Fitting the experimentally obtained BFP patterns enables the determination of k'_{SPP} and L_{D} with the orientation of the nanotube Φ_{CNT} as only additional fit parameter. Fig. 6.7 depicts

a representative example where the experimentally obtained Fourier pattern (fig. 6.7 (a)) was fitted according to eq. 6.2 (fig. 6.7 (b)) with the resulting residuum after subtracting the experimental from the best-fit pattern (fig. 6.7). To compare the experimental

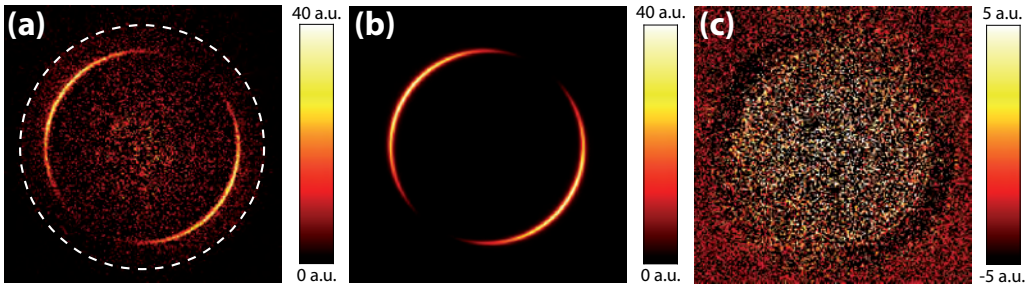

Figure 6.7: (a) Experimentally obtained Fourier plane pattern. (b) Fit of (a) according to eq. 6.2. (c) Residuum after subtraction (b)-(a)

results with theoretical predictions θ_{SPP} and L_{SPP} were calculated numerically using the plasmon dispersion relation for a multilayer system discussed in section 2.2.1. For the calculation the dielectric constant of gold ε_1 at 980 nm from Johnson and Christy [35] and the measured thicknesses of the gold and the SiO_x layers were used. Refractive indices of SiO_x were adjusted to $\varepsilon_1 = n_{SiO_x} = 1.5$ (a physically reasonable choice) and of the upper medium to $\varepsilon_3 = n_{\mathrm{air}} = 1.037$, to reproduce better the experimental values. The increased refractive index for the air-filled half-space is representing the presence of residual SDC surfactant around the SWCNTs. Fig. 6.8 (a) shows the results for the plasmon emission an-

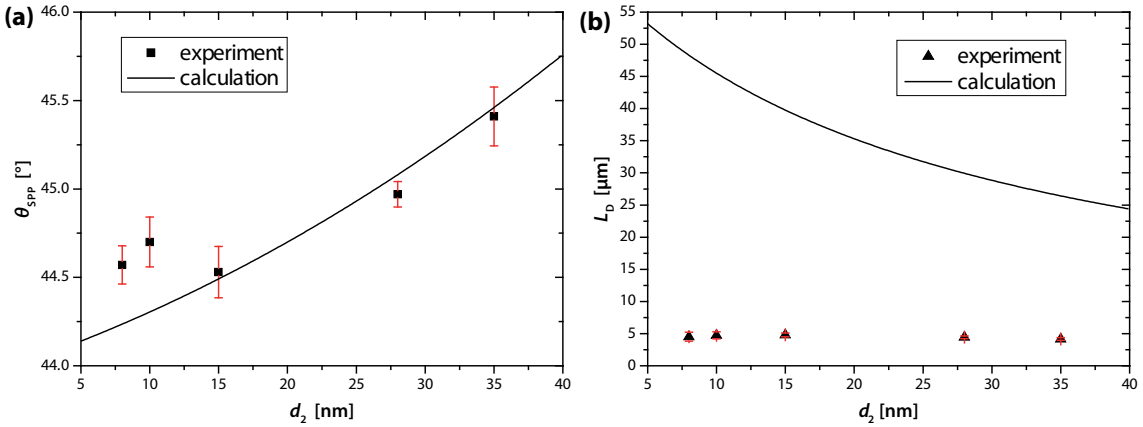

Figure 6.8: Results for (a) the plasmon emission angle θ_{SPP} (black squares) and (b) the propagation length L_{D} (black triangles) obtained from fitted SWCNT BFP patterns on spacer layers with different thicknesses d_2. Also shown are theoretical values for both quantities with different spacer thicknesses calculated according to eq. 2.9 (black solid lines). The error bars represent the standard deviation from several different SWCNTs situated on the same spacer layer.

gle θ_{SPP} obtained from fitting several SWCNT BFP patterns recorded for different spacer thicknesses d_2 (black squares). The error bars result from the standard deviation due to averaging over several different nanotubes on the same spacer layer. Theoretical values

for the plasmon angle as a function of the spacer thickness are also plotted (black solid line) and show a good agreement. The results for propagation lengths L_D extracted from fits are shown in fig. 6.8 (b) (black triangles) together with the calculated values (black solid line). In this case the experimental values reside at much lower propagation lengths than the calculation would suggest. Although the employed calculation model accounts for the damping of the plasmon by the dielectric spacer layer and also considers radiation damping by out-coupled leakage radiation, it does not include damping effects by surface roughness[232]. Increased surface roughness lowers the propagation length significantly due to additional out-coupling of SPPs through scattering at the surface defects[233,234]. In addition fitting the propagation length connected to the FWHM of the Lorentzian line-shape is limited by the resolution limit of the CCD camera that results from the pixel size and the magnification of the imaging system.

A full fitting procedure to further improve the unknown parameters n_{SiO_x} and n_{air} could result in a better match between experiment and calculation. However, there is no guarantee that the values of the refractive indices resulting from the best fit would be the actual values of these parameters, and in fact the success of the fitting procedure could hide potentially relevant sources of error, such as scattering from surface roughness. Therefore any further fitting was chosen not to be carried out. The present model also treats the interaction between the emitting state of the nanotube and the SPP within the weak coupling limit. Strong coupling[235,236] on the other hand would be expected to result in a larger width of the arcs and an apparent decrease of the plasmon propagation length, and therefore could help explaining the remaining disagreement between the experiment and the calculation. Note that in the present configuration the propagation length is mainly limited through coupling to leakage radiation that is used to study the SPPs. For thicker films exceeding 100 nm this coupling would be negligible leading to propagation length on the order of 70 µm.

6.4 Polarization resolved BFP patterns

Coupling to plasmons almost completely reshapes the emission of nanotubes both spatially and with respect to polarization as compared to PL emission on dielectrics. Polarization resolved radiation patterns of single SWCNTs on glass and on SPP supporting metal films are presented in fig. 6.9. Also shown are the corresponding theoretical patterns calculated for a single dipolar emitter (fig. 6.9 (b), (d), (f)). The multilayer structure used in the calculation of the field is the one used in the calculation of the SPP propagation properties: two layers with a finite thickness (gold and SiO_x) bound by two half-spaces (glass/objective and air). As the only free parameter the dipole orientation has been adjusted to match the measured patterns without analyzer (fig. 6.9 (d) and (j), respectively).

On glass the PL is distributed over a large angular range with highest intensities occurring in the directions perpendicular to the nanotube axis resulting in two broad lobes with a maximum peaking near the critical angle (fig. 6.9 (a)). The PL pattern of the same SWCNT recorded with vertical and horizontal analyzer orientations and the corresponding emission patterns are also shown. The PL is polarized mainly parallel to the dipole orientation (fig. 6.9 (b) and (e)). Remarkably, a single emitter situated on a air-dielectric interface also leads to a substantial orthogonal component as can be seen both from theory and experiment (6.9 (c) and (f)). This fact implicates consequences for measurements of polarization contrast, which will not reach zero, when single molecules with a high NA objective are investigated. In contrast the emission patterns from SWCNTs on a metal

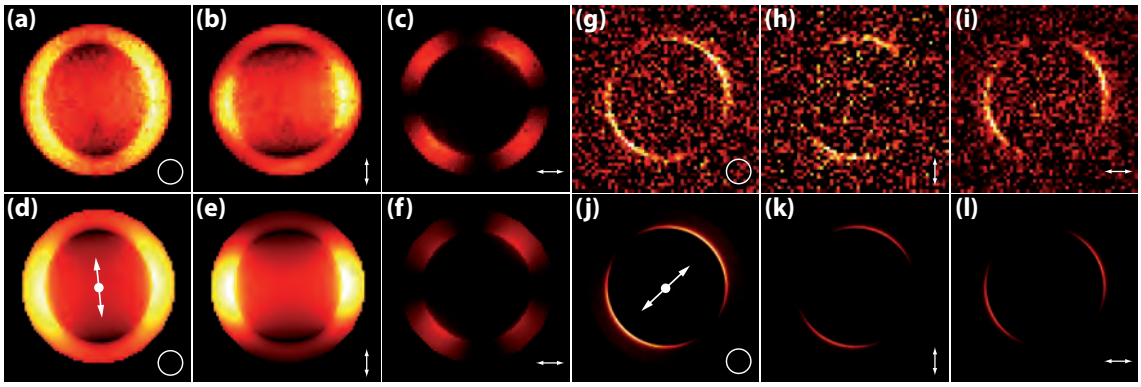

Figure 6.9: Comparison between experimentally obtained and calculated Fourier patterns with different polarizations for a SWCNT deposited on glass: (a), (d) without analyzer, (b), (e) analyzed vertically and (c), (f) analyzed horizontally. The corresponding images for a SWCNT on a 25 nm gold film: (g), (j) without analyzer, (h), (k) analyzed vertically and (i), (l) analyzed horizontally. The white arrow in the theoretical images (d) and (j) indicates the direction of the point dipole used for the calculations.)

film (fig. 6.9 (g)-(i)) show emission concentrated in the direction of the dipole with radial polarization (fig. 6.9 (j)-(l)). That clearly shows that SPPs are launched in the direction of the dipole axis and therefore in the direction of the SWCNT corresponding to a redirection of the SWCNT emission into a narrow angular range in Fourier space together with a directivity along the SWCNT axis. The good agreement between the theoretical images calculated for a single dipole and the experimental images observed for SWCNTs shows that nanotubes act as dipolar sources for plasmons propagating mainly in the direction of the nanotube axis.

Conclusion

This chapter discussed the excitation of propagating SPPs by single optically excited semiconducting SWCNTs on a thin metal film. Placing a single dipolar emitter onto a metal thin film completely reshapes the emission characteristics towards a narrow angular range in the BFP, a unique feature of propagating SPPs. Leakage radiation microscopy images in the BFP and real-space could be modeled successfully and revealed the propagation

length and direction of SPPs. The findings were further supported by a combined BFP pattern and AFM study of single SWCNTs, as well as by polarization resolved detection and subsequent BFP pattern recording. The polarization behavior of SPPs launched by single SWCNTs was found to be radial and was compared to measurements of SWCNTs on glass. The experimentally obtained BFP patterns could be reproduced by theoretical calculations with very good agreement. In essence, exciton recombination in nanotubes launches propagating SPPs on the metal film. These plasmons can couple to photon modes in the lower half-space that are finally detected as leakage radiation.

7 Remote excitation of SWCNTs by propagating SPPs

As shown in the previous chapter, single dipolar emitters are able to excite propagating SPPs which can be investigated by the technique of BFP imaging. However, an important step for a successful device integration is also the possibility to couple SPPs back to propagating radiation. One possible method to achieve this is the opposite scheme, wherein transitions in a dipolar emitter are excited via propagating SPPs. This has been done in the past for dye film patches[237] and clusters of quantum dots[238] located on metal waveguide structures and in the vicinity of a plasmonic nanowire[239]. The source of SPPs in all of these investigations was a focused laser beam either using the adapted Kretschmann configuration with a high NA objective or scattered light at gratings and nanowire edges.

Metal coated aperture fiber probes are an established tool to launch SPPs through the large wave vector components in the near-field of a sub-diffraction aperture, which has been used in the past to investigate SPP self interference[53] and addressing of nanoholes by SPPs[69].

The aim of the work presented in this chapter was to investigate the remote coupling between propagating SPPs and a single emitter. As in the previous chapter, the emitter system was chosen to be SWCNTs due to their known excitation and emission behavior, which enables a straight forward theoretical description as single dipolar emitters and the spectral separation between the excitation and emitted radiation. After characterization of the SPP excitation behavior of the aperture probe by analysis of real space and BFP images, the remote excitation of excitons in individual SWCNTs on a thin metal film via propagating SPPs launched by the aperture probe is discussed. The SWCNT acts as local sensor, mapping the SPP fields created by the aperture probe and the response from the nanotube is detected as leakage radiation at longer wavelengths due to the launch of SPPs, as shown in the previous chapter. A rather simple and established model for the theoretical description of aperture probes is used to understand the formation of the obtained intensity maps. The presented results enable further insight into the coupling between SPPs and single dipolar emitters and provide additional perspectives for integration of emitter systems into plasmonic circuits.

7.1 Excitation of SPPs with an aperture SNOM probe

For all the experiments presented in this chapter the home built shear force AFM head, as described in section 5.1.3, equipped with a commercial aluminum coated aperture probe (Loavlite) was used for the fine distance and positioning control. The nominal aperture diameter was 70 nm and the thickness of the metal coating was stated to be 50 nm. All detection modes are equal to the previous chapter 6, as described in section 5.1 and the aperture AFM head was attached on top of the confocal microscope. The coupling of laser light into the fiber was achieved by focusing an expanded, collimated beam of a linearly polarized HeNe-laser ($\lambda_{ex} = 632.8$ nm, Thorlabs HRP170) with a NA = 0.25 air objective onto the end face of the fiber (see fig. 5.3 in section 5.1.3).

The used sample substrate, consisting of a 20 nm gold film on a standard microscope cover glass with an added SiO_x spacer layer on top, was first used without SWCNT coverage to investigate the SPP excitation behavior of the aperture probe.

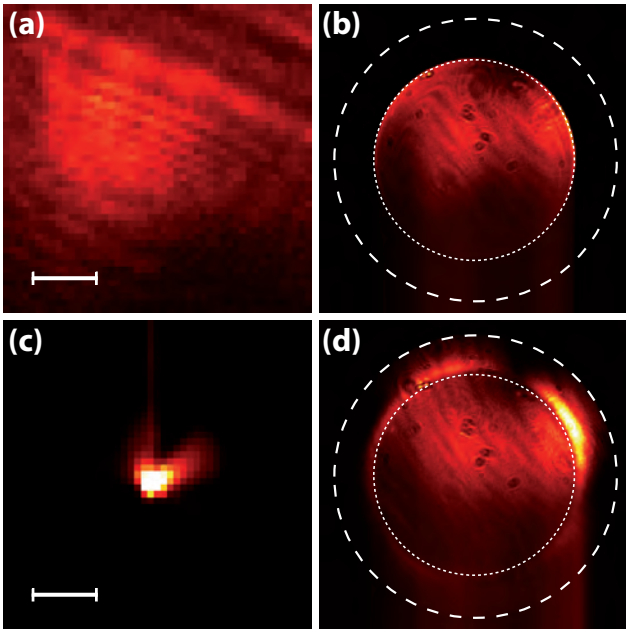

Figure 7.1: (a) Real space and corresponding (b) BFP pattern from an aperture probe excited at 633 nm and positioned about 4 µm away from a 20 nm thick gold film. The radiation is distributed over the sample surface in (a) real space and the (b) BFP pattern is restricted to a maximum angle corresponding to a NA of 1.0 (white dotted circle). Upon approach close to several nanometer to the surface the radiation in real space is confined to a small central spot (the maximum intensity is 20 times higher compared to (a)) and in the BFP angles larger than the critical angle are observed. The scale bar in all real space images corresponds to 2 µm and the maximum collected angle is indicated by a white dashed circle in the BFP patterns.

Fig. 7.1 (a) shows the real space image from the emission out of the aperture tip at a tip-sample distance of about 4 µm. The light is distributed over a large fraction of the sample

area only patterned by a few sample surface defects in the gold film. A corresponding BFP pattern in fig. 7.1 (b) shows the transmitted light confined into the allowed light zone with intensities recorded up to the critical angle $\theta_{\text{crit.}}$, indicated by the white dotted circle. This is in agreement with Snell's law and the definition of a propagating wave[48]. Only propagating waves are arriving in the detection sphere of the microscope objective and no SPPs are excited, which would show up as a signal contribution for angles larger than $\theta_{\text{crit.}}$. Upon activation of the PLL distance control the tip can be brought in the vicinity of the sample surface up to only several nanometer. Fig. 7.1 (c) illustrates the drastic change in the real space image after the approach. The radiation is now confined to a small central spot with two additional lobes extending from the center and decaying within about 1.5 µm. Next to the spatial confinement the overall intensity is drastically increased compared to the case of the aperture tip being further away from the surface. The maximum intensity for the intensity scale is 20 times higher compared to fig. 7.1 (a). Also in the BFP pattern in fig. 7.1 (d) the change upon the approach is visible by an additional intensity contribution in the detected forbidden zone between the critical angle (white dotted circle) and the maximum collected angle by the objective (white dashed circle). This intensity contribution can be attributed to leakage radiation detected from SPPs launched by the aperture probe in the upper left and right direction. It can be correlated with the two lobes reaching away from the central bright spot in the real space image (fig. 7.1 (c)).

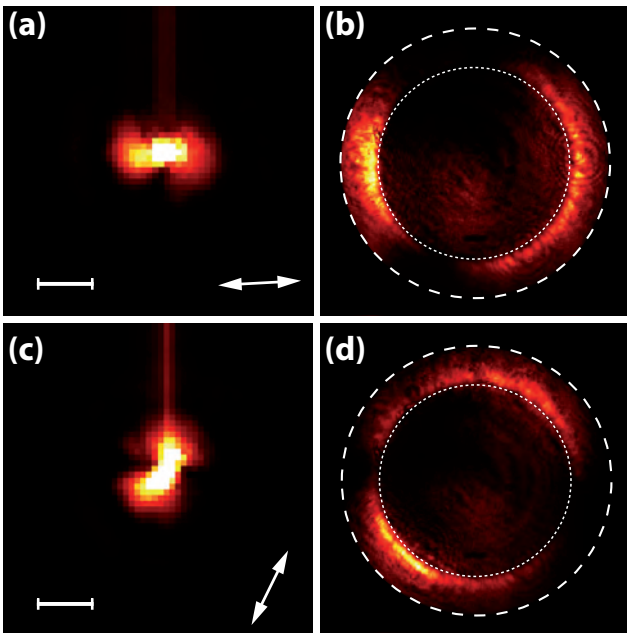

Figure 7.2: Real space images together with the corresponding BFP patterns for SPPs launched by an aperture probe, recorded for two different input polarizations (a),(b) and (c),(d). The output polarization direction, determined from the connecting line between the two lobes, is indicated by the white arrows as well as the critical angle (white dotted circle) and the maximum collection angle of the objective (white dashed circle). It has to be noted that the stripe in (c) is an imaging artifact due to the CCD read out.

The fiber input polarization provides an additional parameter to control the propagation direction of the launched SPPs[240]. In order to control the polarization a rotatable half-wave plate was mounted in front of the fiber coupling objective. Fig. 7.2 (a) shows the real space image with an approached aperture probe and horizontal input polarization, as indicated by the white arrow. Starting from a bright central spot, again two lobes are reaching to the left and to the right, decaying in intensity over the distance. This image reveals a high similarity with the real space images obtained for excited SWCNTs on a gold film presented in the previous chapter 6 (see fig. 6.1 (e)-(g)). SPPs are propagating in opposite directions away from the central excitation spot. In the corresponding BFP pattern in fig. 7.2 (b) two crescents in the direction of the polarization are visible. They are situated again in the region of forbidden light for angles larger than the critical angle (indicated by the white dotted circle) and correspond to the leakage radiation signal from the excited SPPs. This result reproduces the experimental BFP pattern from Hecht et al.[53] and verifies the ability to launch SPPs with the given aperture probe configuration. The double crescent intensity distribution in the BFP for aperture probes was explained by Van Labeke et al.[241] using theoretical calculations. The FWHM of the crescents in the experimental BFP patterns (fig. 7.2 (b)) is larger than compared to the case of SPPs launched by a SWCNT in the previous chapter (see fig. 6.1 (b)-(d)) mainly due to the reduced propagation length at the laser excitation wavelength. For the given sample geometry, according to eq. 2.9, the propagation length at $\lambda_{ex} = 632.8\,\text{nm}$ is $2.3\,\mu\text{m}$ while at $\lambda_{ex} = 980\,\text{nm}$, as in the case of an emitting (6,5) SWCNT, it is $28.2\,\mu\text{m}$. By rotating the wave-plate the fiber input polarization was now rotated by about 70° and the resulting real space image is presented in fig. 7.2 (c). As expected, the orientation of the two lobes follows the altered polarization, indicated again by the white double arrow. The same expected rotation can be observed in the corresponding BFP pattern, shown in fig. 7.2 (d).

In summary, an aperture fiber probe is an adequate tool to realize a scanning SPP source. After coupling laser light into the fiber end the radiation is channeled down to a confined spot at the tip apex. Evanescent fields, extending only few nanometers away from the tip combined with a lateral confinement to the region around the tip apex due to the aperture, present a controlled method to excite SPPs. Additional control can be gained by adjustment of the fiber input polarization, which allows adaption of the SPP propagation direction.

7.2 Remote excitation of SWCNTs by propagating SPPs excited with an aperture SNOM probe

For the subsequent investigation of the coupling between SPPs, launched by an aperture probe, and excitons in SWCNTs, the gold film/spacer layer sample was covered with individual CoMoCat nanotubes. First the sample was scanned confocally in order to

localize luminescent SWCNTs. The focus of the confocal microscope was then positioned on a SWCNT location and fixed for constant detection of the leakage radiation emission of the particular SWCNT. If the SWCNT is successfully excited the following PL emission occurs mainly via SPPs excitation, which can be detected through leakage radiation, as shown in the previous chapter 6. Now the aperture probe was scanned in excitation mode over the SWCNT position and the leakage radiation response was recorded simultaneously in dependence of the probe position as shown in fig. 7.3. The detection signal was filtered

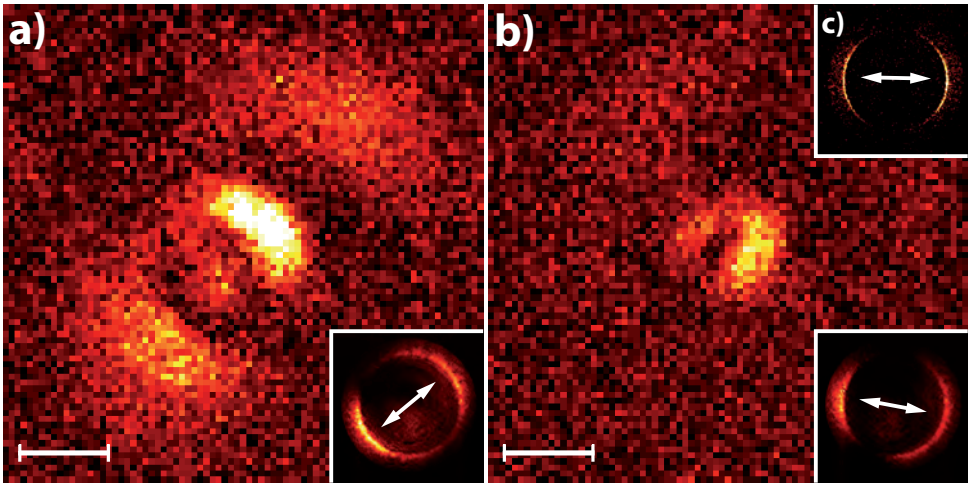

Figure 7.3: Emission maps from a single SWCNT during an aperture probe scan for two different input polarizations (a) and (b) with fixed detection on the nanotube position. The insets on the lower right show the corresponding BFP patterns characterizing the aperture probe output upon a feed at $\lambda_{ex} = 633\,\text{nm}$, the white arrows indicate the input polarization determined according to[241]. (c) depicts the confocal leakage radiation BFP pattern of the same SWCNT after excitation with $\lambda_{ex} = 565\,\text{nm}$. The white arrow indicates the orientation of the nanotube. The scale bar represents 300 nm in both maps.

with a 860 nm long-pass filter, in order to selectively detect emission response originating from the SWCNTs. Two scans were conducted with different aperture input polarizations ($\lambda_{ex} = 633\,\text{nm}$) monitored by BFP images as illustrated by the insets in fig. 7.3 (a) and (b). In order to determine the orientation of the SWCNT a BFP image was taken with direct confocal excitation at $\lambda_{ex} = 565\,\text{nm}$ by the method established in the previous chapter in section 6.1. Fig. 7.3 (c) shows the BFP pattern, which gives a clear indication for nearly horizontal alignment of the SWCNT. Two main features of both emission maps, in fig. 7.3 (a) and (b) can be seen. The first are two emission lobes about 400 nm away from the center (not so pronounced in fig. 7.3 (b)). This signature is a clear sign for remote excitation since the SWCNT shows a signal when the aperture probe is exciting SPPs away from the nanotube position. The observed range of remote excitation is limited by the SPP propagation length. The second emission contribution is located closer to the SWCNT position and features a nearly circular emission with a rather dark center. This feature does not exhibit an exponential intensity decay such as shown in the case of SPPs excited by a point dipole in section 6.2, which points towards a more complex

field distribution, generated by the aperture probe, that is discussed in more detail in the following section. Remarkably, the orientation of the resulting leakage radiation map pattern resembles strongly the orientation of the input light and is not influenced by the SWCNT dipole orientation determined by the BFP pattern in fig. 7.3 (c).

7.3 Theoretical modeling of the SPP fields generated by an aperture probe on a thin metal film

Since the image contrast of the fields probed by the SWCNT is not sufficiently explained by a dipolar SPP source, as indicated in the previous section, theoretical calculations of the fields created by the aperture probe on the surface of the metal film have been performed. These will allow to explain the field mapping behavior of the SWCNTs and to assign different contributions in the image contrast. A plane wave expansion through the multi-layered structure as used by Baida et al. [70] was employed. In this treatment the aperture probe is simulated with the Bethe-Bouwkamp model, which assumes a circular aperture with the radius a in a perfect metallic thin film screen irradiated by a plane wave from the top [242]. It is a recognized model in the field of aperture SNOM [243] and was successfully used before in the literature to describe the emission behavior of an aperture fiber probe in the context of aperture SNOM and to reproduce experimental data [240,244]. Fig. 7.4 shows the geometry assumed for the theoretical calculation, which places the aperture probe with an aperture diameter a and the laser input polarization of Θ at the distance z_T over the sample surface. The multilayer sample is characterized by the thickness of the metal layer d_1 as well as the dielectric constants of the different layer and half-spaces air (ε_0), gold (ε_1) and glass (ε_2). The cylindrical coordinate system is given by r, Ψ and z. According to Baida et al. [70] the field components of an aperture probe on the metal surface at $z = 0$ can be described by the following integrals over the range of collected k-vectors, containing first order Bessel functions J_n:

$$
\begin{aligned}
E_x(r,\Psi) = A_\mathrm{ex} \Bigg\{ & \cos^2(\Theta-\Psi) \int_0^{k_\mathrm{max}} \alpha(k)\, J_0(kr)\, k\,\mathrm{d}k \\
& - \sin^2(\Theta-\Psi) \int_0^{k_\mathrm{max}} \beta(k)\, J_0(kr)\, k\,\mathrm{d}k \\
& - \cos\left[2(\Theta-\Psi)\right] \int_0^{k_\mathrm{max}} \left[\alpha(k)+\beta(k)\right] \frac{J_1(kr)}{kr} k\,\mathrm{d}k \Bigg\}, \\
E_y(r,\Psi) = A_\mathrm{ex} & \left\{ \sin(\Theta-\Psi)\cos(\Theta-\Psi) \int_0^{k_\mathrm{max}} \left[\alpha(k)+\beta(k)\right] \left[\frac{2J_1(kr)}{kr} - J_0(kr)\right] k\,\mathrm{d}k \right\}, \\
E_z(r,\Psi) = A_\mathrm{ex} & \left\{ \left[-\mathrm{i}\cos(\Theta-\Psi) \int_0^{k_\mathrm{max}} \frac{k^2\alpha(k)}{w_3} J_1(kr)\ \mathrm{d}k \right] \right\},
\end{aligned}
\tag{7.1}
$$

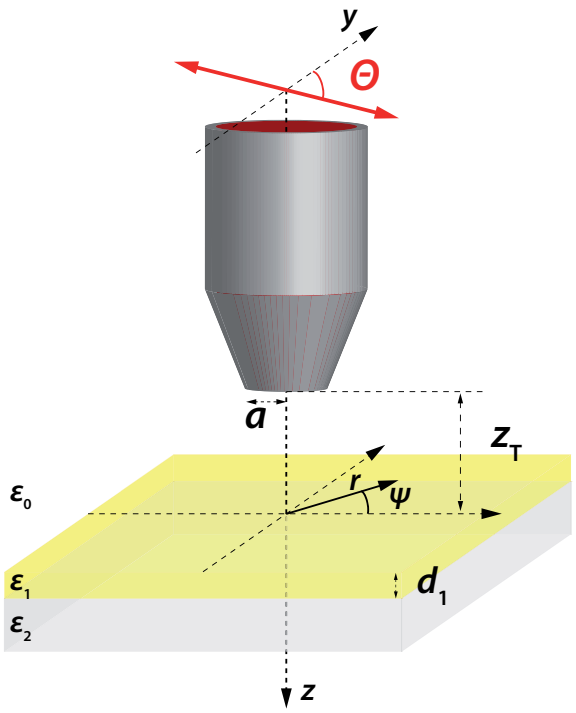

Figure 7.4: Schematic of the multilayer sample system which is used for the calculations of the fields emitted by the tip. Θ represents the angle of the light polarization coupled into the fiber, a the aperture radius, z_T the tip sample distance, Φ the orientation of the SWCNT dipole $\vec{p}$ and the respective dielectric constants of the layer system (ε_0, ε_1, ε_2) and the thickness of the gold film d_1. The cylindrical coordinate system is defined by r, Ψ and z.

where $\alpha(k)$ and $\beta(k)$ are defined as:

$$\begin{aligned}\alpha(k) &= t^{\mathrm{TM}}(k)\,\frac{\sin(ak)}{ak}\,\frac{\varepsilon_0 w_2}{\varepsilon_2 w_0}\,\mathrm{e}^{\mathrm{i}w_0|z_\mathrm{T}|},\\ \beta(k) &= t^{\mathrm{TE}}(k)\,\frac{3\left[ak\cos(ak)-\sin(ak)\right]}{(ak)^3}\,\mathrm{e}^{\mathrm{i}w_0 z_\mathrm{T}}.\end{aligned} \tag{7.2}$$

The multilayer structure is included in eq 7.2 by transmission coefficients t^{TM} and t^{TE}, which can be expressed in terms of Fresnel coefficients in reflection or transmission of the various interfaces, considering the finite thickness of the metal d_1:

$$t^l(k) = \frac{t^l_{01}t^l_{12}\mathrm{e}^{\mathrm{i}(w_1-w_2)d_1}}{1+r^l_{01}r^l_{12}\mathrm{e}^{2\mathrm{i}w_1 d_1}}, \quad l=\mathrm{TE},\,\mathrm{TM} \tag{7.3}$$

with

$$\begin{aligned} t^{\mathrm{TE}}_{01} &= \frac{2w_0}{w_0+w_1}, & r^{\mathrm{TE}}_{01} &= \frac{w_0-w_1}{w_0+w_1},\\ t^{\mathrm{TE}}_{12} &= \frac{2w_1}{w_1+w_2}, & r^{\mathrm{TE}}_{12} &= \frac{w_1-w_2}{w_1+w_2},\\ t^{\mathrm{TM}}_{01} &= \frac{2\varepsilon_1 w_0}{\varepsilon_1 w_0+\varepsilon_0 w_1}, & r^{\mathrm{TM}}_{01} &= \frac{\varepsilon_1 w_0-\varepsilon_0 w_1}{\varepsilon_1 w_0+\varepsilon_0 w_1},\\ t^{\mathrm{TE}}_{12} &= \frac{2\varepsilon_2 w_1}{\varepsilon_2 w_1+\varepsilon_1 w_2}, & r^{\mathrm{TM}}_{12} &= \frac{\varepsilon_2 w_1-\varepsilon_1 w_2}{\varepsilon_2 w_1+\varepsilon_1 w_2}. \end{aligned} \tag{7.4}$$

Different w_m with $m = 0, 1, 2$ consider the wave-vectors in the different media given by the following relation:

$$w_m = \sqrt{\varepsilon_m \frac{\omega^2}{c^2} - k^2}. \tag{7.5}$$

A_{ex} describes an amplitude factor for the initial electric field incident onto the modeled aperture:

$$A_{\mathrm{ex}} = -\frac{8\mathrm{i}\omega a^3 E_{\mathrm{ex}}}{6\pi^2 c}, \tag{7.6}$$

with E_{ex} as initial field amplitude. Fig. 7.5 (a) shows the total intensity $I_{xyz} = |E_x|^2 + |E_y|^2 + |E_z|^2$ for the used sample/tip geometry in the experiment calculated according to eq. 7.1. Next to the enhanced intensity around the aperture metal coating an addi-

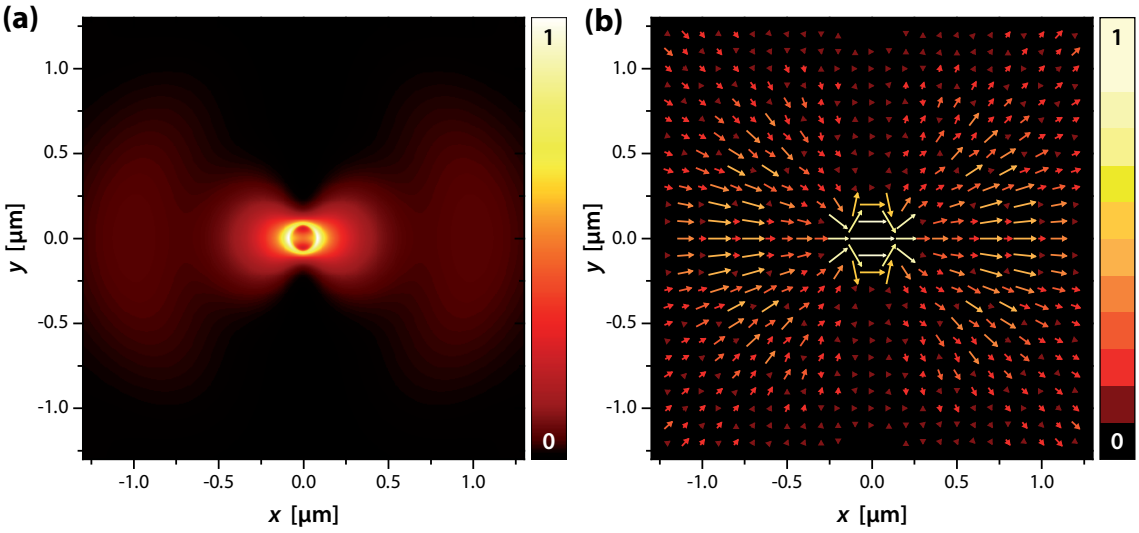

Figure 7.5: (a) Calculated intensity $I_{xyz} = |E_x|^2 + |E_y|^2 + |E_z|^2$ of the full field created in the metal air interface of a 20 nm gold film by the emission of an aperture probe at $\lambda_{\mathrm{ex}} = 633$ nm. (b) shows the corresponding vector plot of the in-plane component $E_x + E_y$ in (a). The length and color of the arrows indicate the magnitude of the polarization in the direction given by the arrow's orientation. The fiber input polarization is in both cases parallel to the x-axis ($\Theta = 0°$).

tional contribution about 1 µm away from the aperture position can be recognized. The corresponding vector plot of the in-plane field component from fig. 7.5 (a) is shown in fig. 7.5 (b).

In general, the formation of the image contrast in the experimental emission maps (fig. 7.3 (a) and (b)) can be understood by the squared product between the field produced by the aperture tip on the surface $\vec{E}_{\mathrm{tip}}$ ($z = 0$) and the transition dipole moment $\vec{\mu}_{\mathrm{SWCNT}}$ of the nanotube:

$$I(x, y) \propto \left| \vec{E}_{\mathrm{tip}} \cdot \vec{\mu}_{\mathrm{SWCNT}} \right|^2. \tag{7.7}$$

The two emission lobes in the experimental maps can be very well understood by excitation via the in-plane component of the aperture tip emission field, since the SWCNTs main

contributing transitions are polarized parallel to the nanotube's axis. Additionally, in measurements with a radially polarized doughnut mode [245] exciting SWCNTs on a gold film no evidence of an increased sensitivity of SWCNT transitions for perpendicular polarized field components could be found. In the vector plot in fig. 7.5 (b) it is shown, that the field contribution remote from the aperture center shows a radial polarization distribution. Thus the main orientation of the lobes follows the input polarization of the fiber but, as in the case of the experimental condition from fig. 7.3 (a) where the SWCNT orientation is roughly 60° rotated with respect to the input polarization Θ, the lobes are expected to be oriented with an angle between the SWCNT orientation and the fiber input polarization Θ. A big factor, which modifies the experimental situation compared to the ideal calculation, is the tip shape. The asymmetric intensity distribution in the experimental emission maps (fig. 7.3 (a) and (b)) is a strong indication for effects caused by a non ideal tip shape. Further, SWCNTs exhibit photo-bleaching behavior upon exposure to high electric fields [99,246], which can explain the reduced signal to noise ration for the second subsequent aperture scan in fig. 7.3 (b).

Fig. 7.6 (a) shows the intensity profile through the experimentally obtained emission map (black solid line), indicated in the inset by the white dashed line, together with a scaled calculated profile, according to eq. 7.1, for the in-plane I_{xy} component (blue dotted line) excited by an aperture probe. The position of the remote lobe emission feature can be

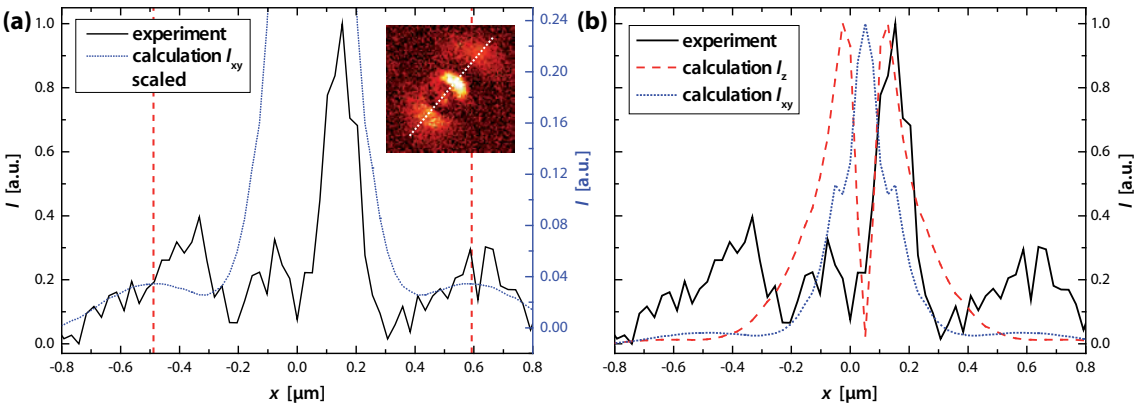

Figure 7.6: (a) intensity profile through the experimental emission map in fig. 7.3 (a) along the white dashed line in the inset together with a scaled profile from the in-plane component I_{xy} (blue dotted line), obtained by calculations of the field emitted by an aperture probe. A good agreement for the position of the outer lobes between experiment and calculation is evident as indicated by the vertical red dashed lines. (b) shows the same experimental profile as in (a) together with the out of plane component I_z (red dashed line) and the in-plane component I_{xy} (blue dotted line).

reproduced very well as indicated by the red dashed vertical lines. It has to be noted, that an even more remote excitation could be achieved by using light for the excitation in the NIR region. Since the damping of the SPP in gold is much lower at these energies, the propagation length is highly increased, as shown in section 2.2.2.

For the explanation of the second, central emission feature in the experimental intensity maps fig. 7.6 (b) shows the same experimental profile (black solid line) together with the theoretical profiles for the in-plane component I_{xy} (blue dotted line) and perpendicular component I_z (red dashed line) of the tip emission. Although the perpendicular component I_z seems to reproduce the central feature rather well, the insensitivity of the SWCNT towards perpendicularly polarized fields and the missing agreement in the lobe position render the assumption rather unlikely. Up to now the considerations of the image contrast only included the excitation efficiency (eq. 7.7). The overestimated intensity in the central region for the in-plane component I_{xy}, in the direct surroundings of the aperture tip, can be understood by taking the conditions for the detection of leakage radiation into consideration. In order to detect the leakage radiation from SPPs launched by the SWCNT with the given Kretschmann like microscopy configuration, the refractive index of the upper half-space medium n_0 needs to be larger than the substrate medium under the metal film (n_2). This is given as long the tip is not on top of the SWCNT position but as the tip moves during the scan over the SWCNT this condition is changed due to the fiber core towards nearly equal refractive indices ($n_0 \approx n_2$). Thus the central part of the emission maps is strongly reduced in detected intensity. This can be also seen as an effect of channeling the radiation into the fiber core, which has been investigated before for the detection of single molecules with an aperture probe on glass [247]. An additional quenching of the SWCNT emission can be expected by the influence of the metal coating in the direct surroundings of the aperture probe.

Conclusion

This chapter investigated the localized SPP excitation behavior of metal coated aperture probes, used in aperture SNOM, when located in close proximity to a metal film. With correlated real-space and BFP pattern images the SPP excitation was demonstrated and the influence of the fiber emission polarization on the SPP propagation direction was shown. By placing SWCNTs on the metal film and subsequent scanning with the before investigated aperture SPP source while detecting the emission from the SWCNTs, remote excitation of SWCNTs was demonstrated. Theoretical modeling of the excited SPP fields reveals that the SWCNT maps the SPPs locally with sub-diffraction resolution. These results demonstrate the possible integration of SWCNTs not only as SPP source but also as element to recouple propagating SPPs back to free space radiation.

8 Radiation channels close to a plasmonic nanowire

This chapter is based on the article "Radiation channels close to a plasmonic nanowire visualized by back focal plane imaging" which was published in *ACS Nano* **2013**, *7*, 10257.

Metallic NWs have drawn particular attention as plasmonic building blocks due to their successful implementation as waveguides[15,248,249], routers and logic gates[250–252]. SPPs on metallic NWs have been investigated by direct visualization[253], using a scanning aperture probe[87], by electrical detection[254] as well as by calculations[88]. A key step in plasmonic applications of NWs is the coupling of the initial energy source to the NW and the contributing energy relaxation pathways[62,64]. Importantly, sub-wavelength light confinement by the SPPs can be used to enhance the interaction between objects and light[220]. This coupling and the excitation and propagation of SPPs have been experimentally visualized by leakage radiation microscopy[12,255,256] combined with imaging of the BFP for a variety of plasmonic structures and devices[14,19,53].

In the following chapter the coupling of the emission from rare earth doped nanocrystals to SPP modes in silver NWs on glass were investigated. The ability of these nanocrystals to exhibit stable, non-bleaching upconverted PL on the anti-Stokes side of the laser energy[194] was employed to avoid temporal intensity fluctuations and to exclude any background contribution from laser scattering, metal luminescence or the sample substrate. With the help of the quantitative analysis of the recorded BFP patterns it is possible to separate the contributions of two different radiation channels. Namely, the direct dipolar emission of the nanocrystals into the glass substrate, observed also in the absence of the NW, and the excitation of propagating SPPs in the NW. In addition to the branching ratio into these two channels the SPP quasi-momentum and the plasmonic active wire length were obtained, all important parameters of active emitter-plasmon structures[62,68]. The results gathered through optical methods were supported by a TEM investigation of the plasmonic nanowires, extracting important parameters, such as material composition and other structure related quantities.

8.1 Transmission electron microscopy (TEM) characterization of plasmonic silver NWs

Silver nanowire samples, synthesized as described in section 5.2.2 were investigated first via TEM measurements carried out by Dr. Angela Wochnik in the group of Prof. Christina Scheu. The TEM experiments were aiming towards the investigation of material properties of the NWs, such as diameter distributions of the wires and a surrounding polymer layer as well as the purity of the wire material. In order to gather a good understanding of the plasmonic behavior the chemical composition of the nanowires has to be known. Contaminants, such as oxide layers, have strong implications for the properties of supported plasmons, since they cause a change in the dielectric function of the plasmonic materials and thus influence the SPP dispersion relation (see section 2.2).

Silver NWs were drop-casted out of solution on a copper TEM grid equipped with a lacey-carbon film as additional sample substrate. The subsequent investigation was performed with a FEI Titan 80-300 (S)TEM microscope operating at 300 kV. The microscope was equipped with an energy dispersive X-ray detector (EDAX), which was used for analytical characterization. Diffraction patterns were recorded using a CCD camera (Gatan UltraScan 1000) with a resolution of 4 million pixel and evaluated, using a calibrated camera constant obtained by measuring a Si standard. Fig. 8.1 (a) shows a representative TEM scan of a NW. Next to the NW (dark contrast) an indication of a cover layer around the NW with a light contrast can be seen. It is more evident in a magnified TEM image, taken from the area marked by the red dashed square, shown in fig. 8.1 (b). The surrounding layer can be attributed to the PVP used as a surfactant during the nanowire synthesis[215,259] as described in section 5.2.2 and was not evident in initial SEM experiments (see fig. 5.4 in section 5.2.2). Additionally, small particles can be found embedded in the surrounding PVP layer. As a first step towards the identification of the exact NW material a diffraction pattern was taken at the center of the wire marked with I in fig. 8.1 (a). Fig. 8.1 (c) shows the indexed diffraction pattern, which reveals the relative orientation between the incoming electron beam and the crystal planes. Together with the fact that silver crystallizes with a face centered cubic (fcc) lattice[191], the zone axis could be determined as [011]. The reciprocal distances determined from the diffraction pattern with 2.34 Å for the 111 plane, 2.04 Å for the 200 plane and 1.44 Å for the 220 are in very good agreement with the characteristic values given in the literature for Ag[257,258]. Indicated by red arrows in fig. 8.1 (c) are additional reflexes, which are situated on a discrete ring with the radius corresponding to a d-spacing of about 2.08 Å. This d-spacing value is close to the value for the 111 plane in copper[258,260]. Also the fact that the reflexes are distributed on a discrete ring is a strong indication of randomly oriented crystals such as in the case of powder diffraction measurements[191]. A fast Fourier transformation analysis (data not shown) of single particles in fig. 8.1 (c) reveals not only the d-spacing of 2.08 Å for the 111 plane but also a spacing of 1.80 Å for the 200 plane characteristic for Cu. These results

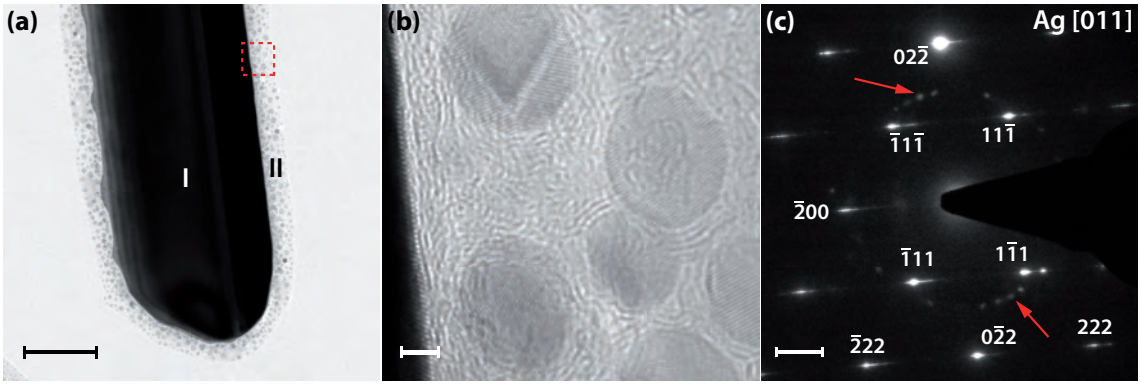

Figure 8.1: (a) TEM image from a representative silver NW with a clearly visible surrounding layer. Markers I and II show the detection position for the EDX spectra presented in fig. 8.2. The scale-bar represents 100 nm. (b) Shows a high resolution image of a magnified sample area from (a) indicated by the red dashed square. In the surrounding of the NW the wrapping polymer is clearly visible together with embedded single Cu nanoparticles. Here, the scale-bar represents 2 nm. (c) Depicts an electron diffraction pattern taken at position I. Apparent diffraction reflexes are indexed. The zone axis was determined to be [011] and the *d*-spacings of the indexed reflexes coincide with values for silver in the literature[257,258]. Indicated by the red arrows are additional reflexes originating from Cu nanoparticles in the polymer. The scale-bar represents $2\,\mathrm{nm}^{-1}$.

give a strong indication that the Cu nanoparticles, used in the synthesis as crystallization seeds, are embedded in the surrounding PVP layer in close proximity to the nanowire. No reflexes originating from silver oxides could be found.

In order to further analyze the chemical composition of the nanowires and the surrounding polymer, EDX spectra were taken at the positions I and II marked in fig. 8.1 (a). Fig. 8.2 shows an overlay of the spectra obtained at both positions divided into two graphs for improved visibility. The elemental analysis occurs through comparison of the different peak positions with values given in the literature[261,262] and are indicated by the vertical lines. As expected, the dominating contribution on the nanowire is silver as can be seen by the cluster of peaks situated around 3.1 keV in fig. 8.2 (a). Apparently, they are less pronounced in the case of the polymer. Typical X-ray emission lines for copper (at about 1.0, 8.0 and 9.0 keV) are visible due to the use of a copper TEM grid but even more due to the presence of Cu nanoparticles, since they are much more intense in the case of the PVP EDX spectrum at position II. This correlates nicely with the results from the electron diffraction data in fig. 8.1 (c). A signal for carbon is visible at about 0.25 keV, which appears more pronounced in the spectrum from the polymer due to the higher carbon content of the PVP. The signal for oxygen is only visible in the spectrum of the polymer and can be attributed again to PVP. Both spectra show small traces of iron and cobalt contaminants. In summary, the NW appear to consist only of silver, without any oxide contamination. The second result is the presence of a PVP polymer layer surrounding

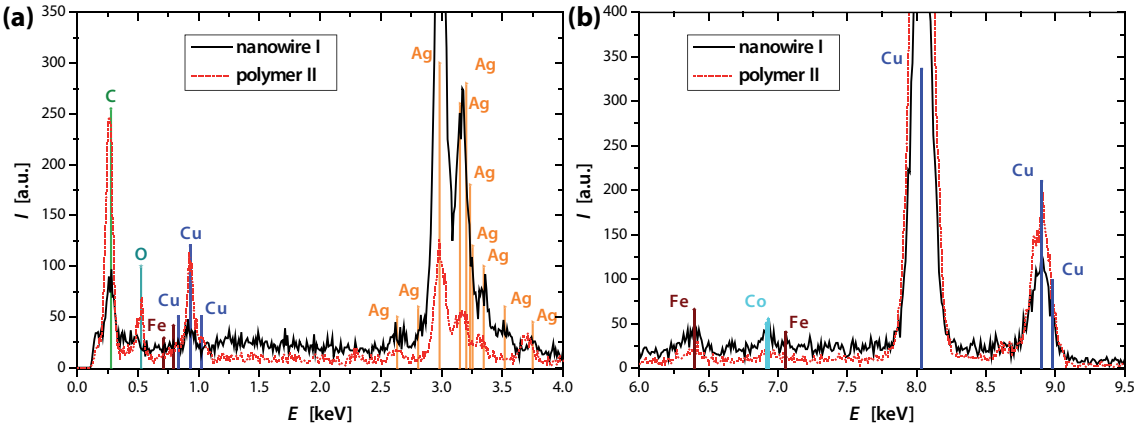

Figure 8.2: EDX spectra from the nanowire in fig. 8.1 (b) taken on the wire itself (black solid line, position I) and on the surrounding polymer layer (red dotted line, position II). For increased visibility the complete spectra are shown for two magnified energy ranges (a) and (b). The vertical lines indicate energy positions of characteristic element X-ray emission lines[261,262].

the nanowires, which contains embedded copper nanoparticles as residue from the wire synthesis.

In the course of the TEM investigation magnified scans, comparable to fig. 8.1 (b) were taken from 77 different NWs. Out of these images the wire diameter D_{wire} and the PVP thickness d_{PVP} were measured. Fig. 8.3 a shows the histogram of the wire diameter, to-

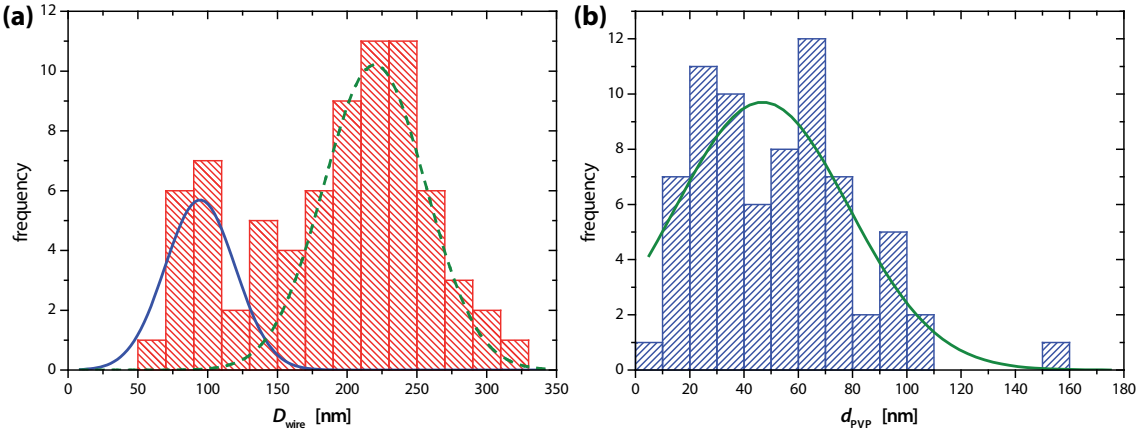

Figure 8.3: Distribution of (a) NW diameters from 77 different NWs measured from TEM images. The histogram was fitted with two Gaussian curves (blue solid line and green dashed line) revealing a maximum in the distribution at 95±30 nm and 220±43 nm. Also the thickness of the surrounding polymer layer was measured from the same NWs (b). This distribution exhibits a maximum at 48±37 nm, determined again by a Gaussian fit (green solid line).

gether with two Gaussian fits around the maxima in the distribution peaking at 95±30 nm (blue solid line) and 220±43 nm (green dashed line). The range of the diameter distribution coincides with the findings obtained by AFM topography measurements presented in

the following sections 8.2 and 8.4. Fig. 8.3 (b) shows the distribution for the measured PVP thickness d_{PVP} together with a Gaussian fit (green solid line) of the data peaking at 48±37 nm.

8.2 Optical investigation of different emission channels close to a plasmonic NW

For the optical investigations in the following section combined samples, consisting of $NaYF_4$ nanocrystals doped with 20 wt% $Yb^{3+}$and 2 wt% Er^{3+} subsequently spin-coated on top of silver nanowires on a glass substrate, as described in section 5.2.2, were used.

First, a sample area of 100 μm^2 was characterized by detecting the upconverted PL after excitation at 980 nm with a narrow band pass filter centered at 670 nm with a FWHM of 10 nm in front of the APD used for confocal scanning signal detection as described in section 5.1.1. A representative PL image of a magnified sample area can be seen in fig. 8.4 (a). Subsequently the same sample area was mapped via AFM to measure

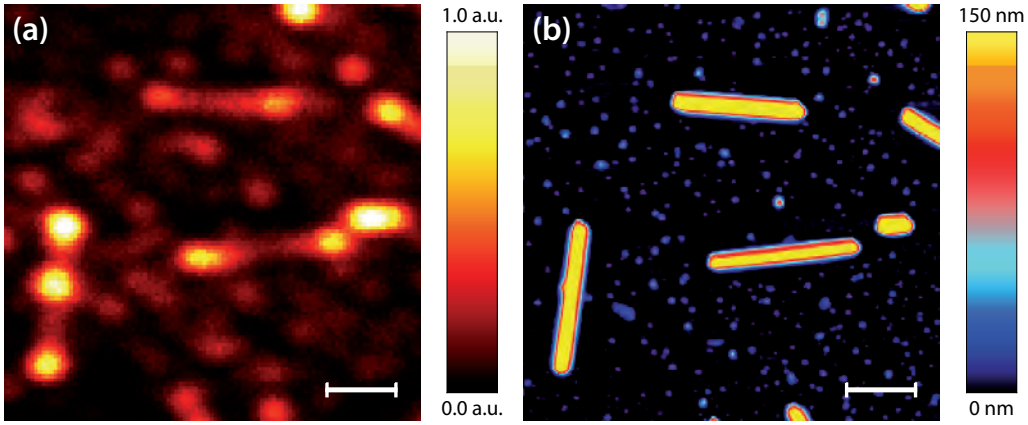

Figure 8.4: (a) Confocal PL map of a representative sample area together with the corresponding topography data in (b). In the PL map the NWs show up as elongated structures with higher intensity at the NW ends. Several single PL spots are located around the NWs which can be attributed to single or small clusters of rare earth nanocrystals which can also be seen in the AFM data. The scale bar represents 2.0 µm in both images.

the topographic height of each investigated NW. In the PL map (fig. 8.4 (a)) the NWs appear as luminescent elongated structures with additional bright end spots or bright spots along the wire. In addition, weaker luminescent spots are distributed all over the sample. The topography of the same sample area (fig. 8.4 (b)) shows the NWs at the same positions with lengths of few micrometers and heights between 100 and 250 nm as well as several smaller structures nearby (about 20 nm in height). The size of the smaller structures together with their luminescent behavior identifies them as single nanocrystals or small clusters of several crystals. From the PL signal shown in fig. 8.4 (a) it is evident that nanocrystals deposited in the vicinity of the NWs show enhanced PL and that the

plasmonic enhancement is most efficient at the NW ends. Emission enhancement can result from new radiation channels provided by the metal nanostructure corresponding to an increased local density of states[104]. In general, radiation channels are connected to characteristic angular distributions of emission that can be studied by BFP imaging[13,263], as described in section 3.

To illustrate the change of the emission characteristics induced by the NW BFP patterns of NCs without NW were measured, filtering the detected signal for the upconverted PL (bandpass 670 nm). Fig. 8.5 shows a representative example. The patterns consist of a

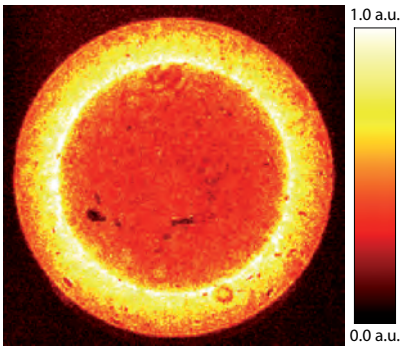

Figure 8.5: Back-focal plane PL emission pattern detected for a nanocrystal on glass. The detected angular range is limited by the maximum collection angle of the microscope objective that is given by its NA = 1.4.

radially symmetric intensity distribution that increases from the largest detectable angle given by the NA of the microscope objective towards the critical angle. For smaller angles the pattern shows a more uniform and weaker intensity.

In the next step BFP patterns were recorded for different NWs at varying excitation positions along the NW, again filtering the detected signal for the upconverted PL. Fig. 8.6 shows a representative example of the PL map of a single NW (fig. 8.6 (a)) together with the excitation positions and the recorded BFP patterns (fig. 8.6 (b)-(d)). When the NW

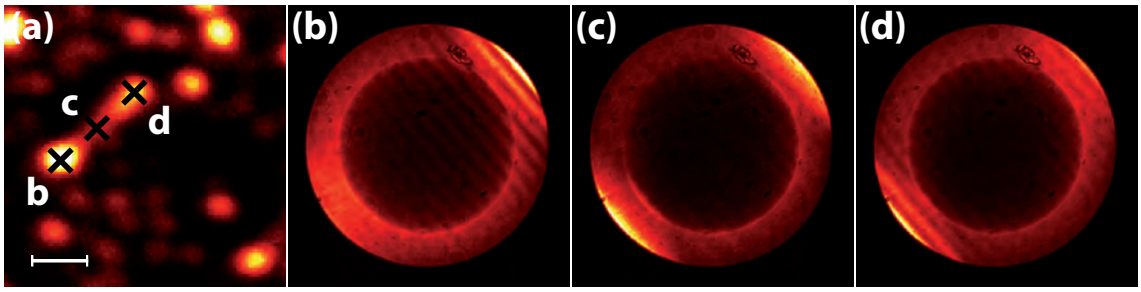

Figure 8.6: (a) Confocal PL map of a wire decorated with nanocrystals. The scale bar represents 2.0 µm. Upon excitation at different positions (b-d) the corresponding BFP patterns (b)-(d) were recorded. The detected angular range is limited by the maximum collection angle of the microscope objective that is given by its NA = 1.4.

is excited in the middle the BFP image (fig. 8.6 (c)) shows a symmetric pattern oriented

along the NW axis with two brighter lobes at the rims of the pattern. In contrast, the patterns recorded upon excitation of the NW ends (fig. 8.6 (b),(d)) exhibit an asymmetric intensity distribution with the lobes on the opposite side of the excitation position being brighter than the other. In addition, a fringe pattern with more contrast is visible when the NW is excited at the ends. This indicates that the position of excitation strongly influences the angular emission characteristics of the NW.

8.3 Theoretical description of the BFP pattern from different emission channels

The analysis and subsequent separation of radiation channels is possible if each of the contributing channels can be modeled theoretically. In order to describe the measured BFP patterns two apparent signal contributions can be distinguished: The direct emission from NCs and detected leakage radiation from SPPs propagating along the nanowire surface.

8.3.1 Theoretical modeling of the direct NC emission pattern

The first signal contribution stems from nanocrystal emission which is not coupled to the NW as presented for nanocrystals in the absence of a NW in fig. 8.5. As described in section 5.2.2, a single nanocrystal contains between 600 and 10^3 dipolar emission centers without preferred orientation, depending on the exact particle size. Thus the resulting BFP pattern can be treated as the sum of patterns from randomly oriented dipoles. This contribution is modeled using the theoretical description of dipolar emission on an interface from Lieb et al.[13] as described in section 3.1.1. Due to the symmetry of the resulting functions the random orientation of dipoles can be represented by two orthogonal in-plane dipoles and an additional dipole perpendicular to the surface, also indicated in fig. 8.7 (a) by black arrows ($\vec{p}_x$, $\vec{p}_y$ and $\vec{p}_z$). Thus the intensity in the the BFP I_{NC} can be described by the sum of the individual patterns of the single dipoles:

$$I_{\mathrm{NC}}\left(\vec{k}_{\mathrm{BFP}}\right) = I_{\mathrm{dipole},\,x} + I_{\mathrm{dipole},\,y} + I_{\mathrm{dipole},\,z}, \tag{8.1}$$

as depicted in fig. 8.7 (c). The comparison of the experimental pattern in fig. 8.7 (b) and modeled pattern in fig. 8.7 (c) reveals a very good agreement.

8.3.2 Theoretical modeling of the NW leakage radiation emission pattern

The second contribution originates from SPPs launched by nearby nanocrystals propagating along the NW surface which are detected as leakage radiation[255,256]. A characteristic signature of this radiation channel is the fringe pattern in the BFP image that results from the finite length of the NW in the µm range emitting via leakage radiation. BFP patterns

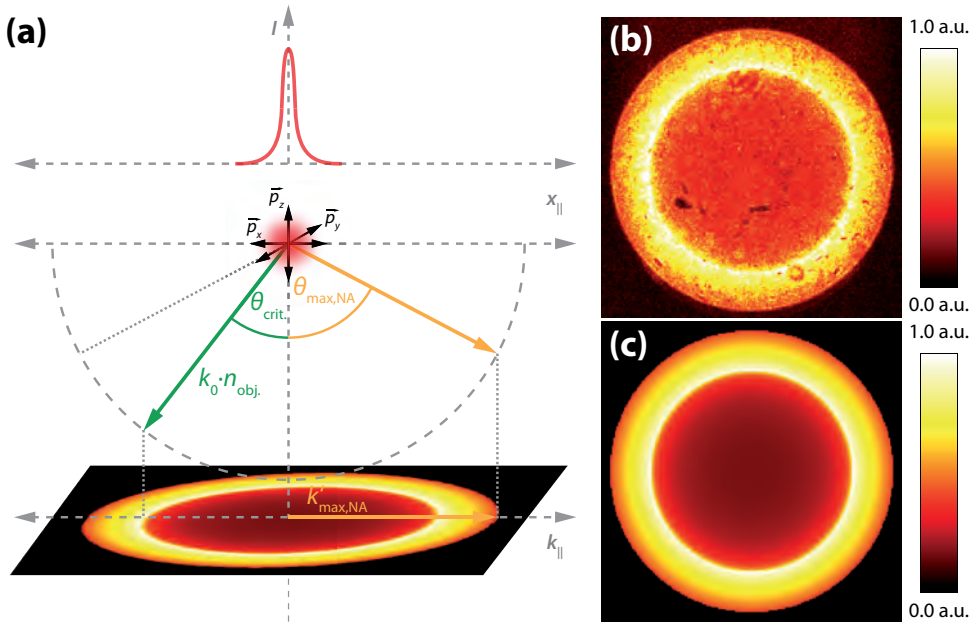

Figure 8.7: (a) Schematic of the BFP imaging for randomly oriented dipoles represented by two orthogonal in-plane and one out-of-plane dipole, indicated by black arrows. Also indicated are the projections of the critical angle $\theta_{crit.}$, the maximum detectable angle $\theta_{\mathrm{max,\,NA}}$ and k vector $k'_{\mathrm{max,\,NA}}$ determined by the objective NA. (b) shows an experimental BFP from a single NC on glass together with a (c) modeled pattern, calculated according to eq. 8.1.

of SPPs propagating along a plasmonic nanowire were described before in the literature by Shegai et al.[19]. The used model consisted of a chain of dipoles connected with a phase relation as introduced in section 3.2.2 and reproduces qualitatively the observed fringe pattern in the experimental BFP patterns (fig. 8.6). Although the fringe distance could be reproduced in some cases with good agreement, the intensity distribution between the single fringe components could not be modeled well.

In order to improve the description of the NW radiation channel a leaky 1D antenna resonator model, following the calculations from Taminiau et al.[20] was employed. The configuration is defined by the finite NW length L, the wire orientation given by the in-plane angle Ψ and the input excitation at the position a as shown in fig. 8.8. Plasmon propagation depends on k_{SPP} supported by the NW and a complex reflection coefficient r at its end including the phase change ϕ taken up with each reflection:

$$r = |r| \cdot \mathrm{e}^{i\phi};\ 0 \leq |r| \leq 1. \tag{8.2}$$

In order to include losses in the metal the plasmon wave-vector k_{SPP} is defined as a complex value in direct correlation with the propagation length L_D[32] as derived in section 2.1:

$$k_{\mathrm{SPP}} = k'_{\mathrm{SPP}} + ik''_{\mathrm{SPP}} = k'_{\mathrm{SPP}} + i\frac{1}{2L_D} \tag{8.3}$$

Taminiau et al.[20] first derive the current distribution $J(x,a)$ along the nanowire as a superposition of harmonic waves for $-\frac{L}{2} \leq x < a$ as

$$J(x,a) = \frac{J_0\left(\mathrm{e}^{\mathrm{i}k_{\mathrm{SPP}}a} + r\mathrm{e}^{\mathrm{i}k_{\mathrm{SPP}}L}\mathrm{e}^{-\mathrm{i}k_{\mathrm{SPP}}a}\right)}{1 - r^2\mathrm{e}^{2\mathrm{i}k_{\mathrm{SPP}}L}}\left(r\mathrm{e}^{\mathrm{i}k_{\mathrm{SPP}}L}\mathrm{e}^{\mathrm{i}k_{\mathrm{SPP}}x} - \mathrm{e}^{-\mathrm{i}k_{\mathrm{SPP}}x}\right), \tag{8.4}$$

and for $a < x \leq \frac{L}{2}$ as

$$J(x,a) = \frac{J_0\left(r\mathrm{e}^{\mathrm{i}k_{\mathrm{SPP}}L}\mathrm{e}^{\mathrm{i}k_{\mathrm{SPP}}a} + \mathrm{e}^{-\mathrm{i}k_{\mathrm{SPP}}a}\right)}{1 - r^2\mathrm{e}^{2\mathrm{i}k_{\mathrm{SPP}}L}}\left(\mathrm{e}^{\mathrm{i}k_{\mathrm{SPP}}x} - r\mathrm{e}^{\mathrm{i}k_{\mathrm{SPP}}L}\mathrm{e}^{-\mathrm{i}k_{\mathrm{SPP}}x}\right). \tag{8.5}$$

J_0 stands for the initial amplitude of the induced wave and depends on the type of dipole, its oscillator strength, the three-dimensional (3D) configuration and modal fields[235,264]. Since the focus of interest in this discussion is on the intensity distribution in the BFP and not in the calculation of absolute intensity values the initial amplitude is set to $J_0 = 1$. The underlying model for the presented current expression is conceptually equal to the dipole-chain model used by Shegai et al.[19] mentioned above with the addition of the variable excitation position a. To obtain the observed far field in Fourier space the current distribution is subjected to a Fourier transform which results in the formula for the fields in Fourier space:

$$E_{\mathrm{NW,\,BFP}} = E_0 \int_{-\frac{L}{2}}^{\frac{L}{2}} J(x,a)\,\mathrm{e}^{-\mathrm{i}k_{\parallel}x}\,\mathrm{d}x \tag{8.6}$$

E_0 describes the field of a point dipole at the origin and oriented parallel to the wire's long axis, which can be used to consider the air/glass interface on which the NW is deposited. This concept is again comparable to the approach chosen by Shegai et al.[19] where the structure factor, describing the phase relation between the different dipoles in the chain, is multiplied by a single dipole BFP pattern, reflecting the radiation behavior through the interface. The evaluation of the integral in eq. 8.6 gives a full description of the intensity distribution of SPP leakage radiation from a plasmonic nanowire in the Fourier plane with the orientation angle Ψ:

$$\begin{aligned} I_{\mathrm{NW}}\left(\vec{k}_{BFP}\right) = I^{\Psi}_{\mathrm{dipole}} \cdot \Bigg| \frac{\mathrm{i}}{1 - r^2\mathrm{e}^{2\mathrm{i}k_{\mathrm{SPP}}L}} \Bigg(A\left[\frac{r\mathrm{e}^{\mathrm{i}k_{\mathrm{SPP}}L}\mathrm{e}^{-\mathrm{i}(k_{\parallel}-k_{\mathrm{SPP}})z}}{k_{\parallel}-k_{\mathrm{SPP}}} - \frac{\mathrm{e}^{-\mathrm{i}(k_{\parallel}+k_{\mathrm{SPP}})z}}{k_{\parallel}+k_{\mathrm{SPP}}}\right]_{-\frac{L}{2}}^{a} \\ + B\left[\frac{\mathrm{e}^{-\mathrm{i}(k_{\parallel}-k_{\mathrm{SPP}})z}}{k_{\parallel}-k_{\mathrm{SPP}}} - \frac{r\mathrm{e}^{\mathrm{i}k_{\mathrm{SPP}}L}\mathrm{e}^{-\mathrm{i}(k_{\parallel}+k_{\mathrm{SPP}})z}}{k_{\parallel}+k_{\mathrm{SPP}}}\right]_{a}^{\frac{L}{2}}\Bigg)\Bigg|^2, \end{aligned} \tag{8.7}$$

with

$$\begin{aligned} A &= \mathrm{e}^{\mathrm{i}k_{\mathrm{SPP}}a} + r\mathrm{e}^{\mathrm{i}k_{\mathrm{SPP}}L}\mathrm{e}^{-\mathrm{i}k_{\mathrm{SPP}}a} \\ B &= r\mathrm{e}^{\mathrm{i}k_{\mathrm{SPP}}L}\mathrm{e}^{\mathrm{i}k_{\mathrm{SPP}}a} + \mathrm{e}^{-\mathrm{i}k_{\mathrm{SPP}}a} \end{aligned} \tag{8.8}$$

and

$$\begin{aligned} k_{\parallel} &= \vec{k}_{\mathrm{BFP}} \cdot \vec{e}_{\mathrm{NW}} \\ \vec{e}_{\mathrm{NW}} &= \begin{pmatrix} \cos(\Psi) \\ \sin(\Psi) \end{pmatrix}. \end{aligned} \tag{8.9}$$

Fig. 8.8 shows a representative NW BFP pattern I_{NW} calculated for a wire with a length of $L = 4.0\,\mu\mathrm{m}$, a diameter of 150 nm and a plasmon wave vector of $k'_{\mathrm{SPP}} = 1.648 \cdot 10^7 \mathrm{m}^{-1}$ predicted for SPPs in NWs surrounded by glass, excited at the nanocrystal emission at 670 nm[19,40]. The modulus of the reflection coefficient $|r|$ was taken to be 0.6 and the phase shift $\phi = 80°$[63]. The NW is excited at $a = -1.8\,\mu\mathrm{m}$, which corresponds to a excitation position 200 nm away from the wire edge. Together with the clearly visible fringes resulting

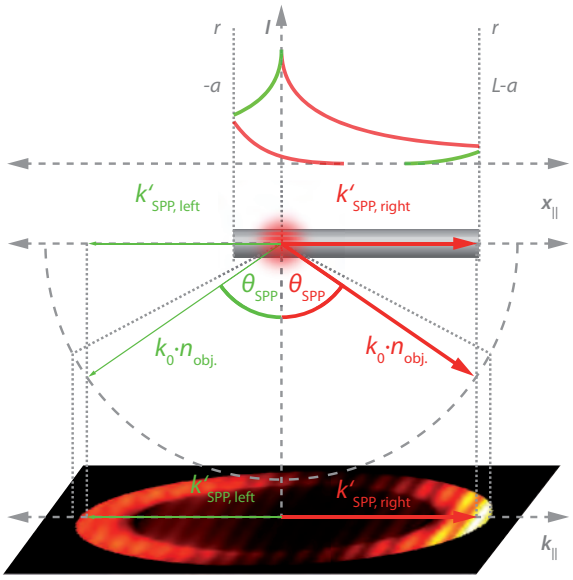

Figure 8.8: Schematic of the formation of a BFP pattern for the leaky antenna resonator as described in eq. 8.7. Indicated by the arrows are the wave-vectors for the right (red $k'_{\mathrm{SPP,\,right}}$) and the left (green $k'_{\mathrm{SPP,\,left.}}$) direction and their projection onto the Fourier plane after leaking into the glass substrate at the resonance angle θ_{SPP} given by $k'_{\mathrm{SPP}} = k_0 n_{\mathrm{obj.}} \sin\theta_{\mathrm{SPP}}$.

from the finite wire length the schematic in fig. 8.8 illustrates the formation of the BFP pattern, which explains the asymmetry in the intensity distribution that is also seen in the experimental patterns after exciting the wire at the ends (fig. 8.6 (b) and (d)). If the NW is excited at the left end, SPPs can travel only to the right before they are reflected. In Fourier space the wave-vector components are sorted by their propagation direction. Therefore it is evident that the excitation in the middle of the NW results in a symmetric BFP pattern with similar intensities on both sides (fig. 8.6 (c)). The present model treats the several µm long NWs as quasi-1D structures. For shorter NWs with considerably smaller aspect ratio the contribution of distinct sub- and super-radiant modes becomes more significant[20,264,265] due to the lower order of the modes.

The influence of the excitation position a on the fringe position and distribution in the leakage radiation BFP pattern I_{NW} is summarized in fig. 8.9. Fig. 8.9 (a) shows an intensity map of profiles through calculated NW BFP patterns I_{NW} along the central propagation direction $k_{\|}$ as a function of the excitation position a. For this calculation, according to eq. 8.7, an exemplary NW with a length of $L = 4.0\,\mu\mathrm{m}$, a diameter of 150 nm, a reflection

coefficient of $|r| = 0.6$ and a phase shift of $\phi = 80°$ [63] was chosen. The excitation position a, in this map ranges from central excitation of the NW ($a = 0\,\text{nm}$) to excitation at the wire edge ($a = 2.0\,\mu\text{m}$). The figure illustrates the significant changes in the fringe pattern upon different excitation positions. Not only the intensity ratio between single fringes changes, but also the position with respect to $k_{\parallel}$ is subjected to a significant change. The change is further clarified by full range BFP patterns for different excitation positions, as marked by the orange dashed lines b–e in fig. 8.9 (a). Fig. 8.9 (b) shows a BFP pattern

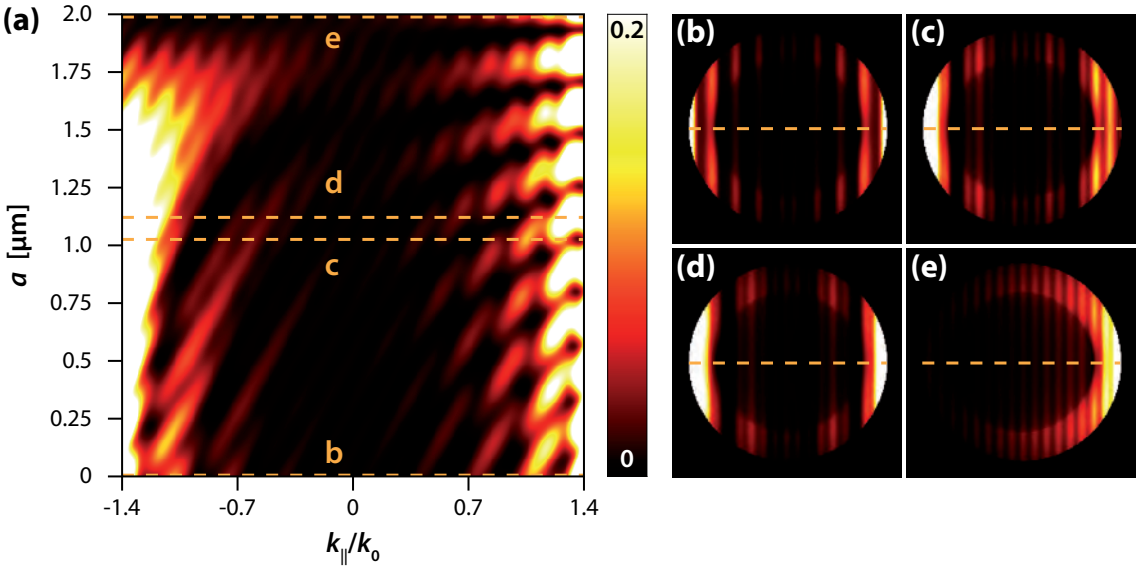

Figure 8.9: (a) map of profiles through theoretical BFP pattern I_{NW} along the propagation direction $k_{\parallel}$ as a function of the excitation position a, calculated for a 4 µm long NW with a diameter of 150 nm. The intensity scale is slightly saturated in order to reveal fringe features in the central region $\frac{|k_{\parallel}|}{k_0} < 1$. Orange dashed lines b–e mark the positions for the complete calculated patterns for central (b) excitation ($a = 0\,\text{nm}$), two positions separated 100 nm from each other (c) $a = 1.02\,\mu\text{m}$, (d) $a = 1.12\,\mu\text{m}$ and the end excitation with $a = 2.0\,\mu\text{m}$. All BFP patterns exhibit the same intensity scaling.

calculated for excitation in the center of the NW ($a = 0\,\mu\text{m}$) and reveals a symmetric intensity distribution with the same number of fringes on each side. Whereas excitation on the NW end ($a = 2.0\,\mu\text{m}$) results in an asymmetric intensity distribution, decaying from the right to left side, as discussed in fig. 8.8. Fig. 8.9 (c) and (d) depict two BFP patterns calculated for excitation positions $a = 1.02\,\mu\text{m}$ and $a = 1.12\,\mu\text{m}$ only separated 100 nm from each other. Still a significant change in the fringe pattern on the right side of the BFP pattern is noticeable.

The fringe pattern in general can be understood in the context of a finite length emitter. For SPPs propagating on an unconfined metal film with an exponential intensity decay can be modeled in the BFP by a Lorentzian line-shape with the maximum centered at k_{SPP}, as shown in section 6.2. In the case of a SPP propagating along a plasmonic NW, the propagation is confined to the length of the NW, thus the system behaves like a

finite emitter of leakage radiation. This finite emitter, approximated in real space by a delta function with the width L, leads in the BFP after Fourier transformation to a sinc function[266]:

$$\text{sinc}\left(k_{\parallel}\right) = L\frac{sin\left(k_{\parallel}\frac{L}{2}\right)}{k_{\parallel}\frac{L}{2}}. \tag{8.10}$$

Since the SPP still decays exponentially the leakage radiation signature in the BFP consist of a convolution of the Lorentzian line-shape with the sinc function, which creates a sinc-like function with a maximum centered at k_{SPP}. This is illustrated by the fringe pattern in the background of fig. 8.10. Fig. 8.10 shows the theoretical dispersion relation for a

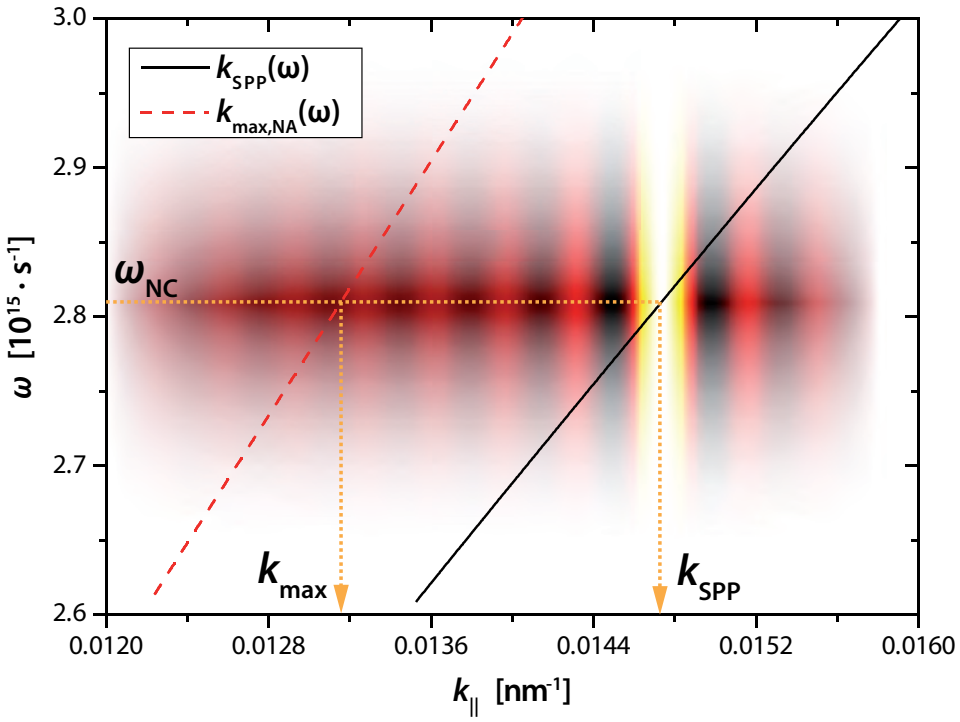

Figure 8.10: Calculated plasmon dispersion $k_{\text{SPP}}(\omega)$ (black solid line) for a silver NW with a diameter of 150 nm surrounded by glass according to eq. 2.19, together with the maximum detectable k-vector by a NA = 1.4 objective $k_{\text{max}}(\omega)$. The underlying sinc $(k_{\parallel})$-like pattern illustrates the fringes caused by the finite length emitter at the NC emission frequency ω_{NC}, which enables the detection of SPP leakage radiation from the NW, even if the central k'_{SPP} value is beyond the detectable k_{max}.

silver NW with a diameter of 150 nm, surrounded by glass according to eq. 2.19, $k_{\text{SPP}}(\omega)$ (black solid line) together with the maximum detectable k-vector range for a NA = 1.4 objective $k_{\text{max}}(\omega)$ left of the dashed red line. For a given emission wavelength of the NCs ω_{NC} (orange dotted line) the NW exhibits a k_{SPP} value outside the detectable range of the objective k_{max}. However, the fringes from the sinc-like intensity distribution in the BFP, centered at k_{SPP}, extend far into the detectable range. This enables not only the detection of leakage radiation but also the determination of k_{SPP}, by fitting the intensity decay of the fringe pattern, as well as the emitter length L, from the fringe distance, as shown in the following section.

8.4 Discussion of parameters extracted from fitting BFP patterns

All experimental BFP patterns were fitted with a combination of the NW pattern I_{NW} and the pattern consisting of randomly oriented dipoles I_{NC} developed in section 8.3:

$$I_{BFP,fit}\left(D, W, k'_{\mathrm{SPP}}, L, L_{\mathrm{D}}, a\right) = D \cdot I_{\mathrm{NC}} + W \cdot I_{\mathrm{NW}}\left(k'_{\mathrm{SPP}}, L, L_{\mathrm{D}}, a\right) \tag{8.11}$$

After adjusting the orientation angle Ψ to the NW axis, the free fit parameters were the amplitudes of the different channel contributions D and W, the real part of the plasmon wave-vector k'_{SPP} together with the propagation length L_D, the wire length L and the NC position a. Representative fits of experimental BFP patterns are shown in fig. 8.11 (d)-(f) together with the experimentally obtained patterns (fig: 8.11 (a)-(c)). The fitted patterns

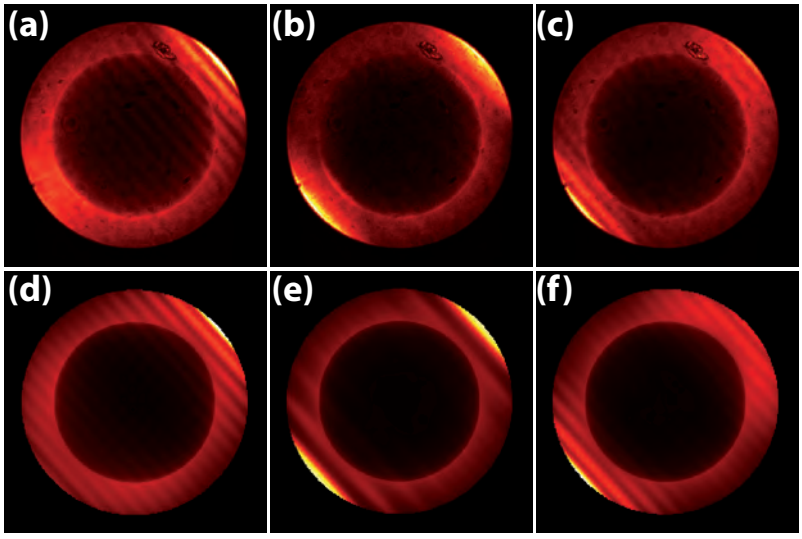

Figure 8.11: (a)-(c) Experimentally obtained BFP patterns from a NW excited at three different positions (b-d in fig: 8.6) (a) together with best fit patterns (d)-(f) calculated according to eq. 8.11.

agree very well with the experimental results supporting the simplified model describing the emission by the two distinct channels.

Theoretical BFP patterns used in the fit for the NC and the NW were normalized to the intensity radiated into all possible angles below and above the air/dielectric interface, as discussed in section 3.1.1 in the context of the detection efficiency dipolar radiation:

$$\int_0^{\pi}\int_0^{2\pi} I_{\mathrm{NC}}\ \mathrm{d}\varphi\mathrm{d}\theta = 1, \quad \int_0^{\pi}\int_0^{2\pi} I_{\mathrm{NW}}\ \mathrm{d}\varphi\mathrm{d}\theta = 1, \tag{8.12}$$

Thus, the amplitudes D and W can be seen as the number of photons emitted via each channel. The branching ratio F between the two radiation channels, that reflects the coupling strength between NC and NW can be defined as $F = \frac{W}{D}$. For the 49 studied NW positions this branching ratio was found to be 0.7 ± 0.3 on average. No correlation

between the branching ratio and the wire thickness could be observed. The spread in F probably reflects different NC to NW distances also caused by different thicknesses of the polymer layer covering the nanowires.

From the fringe distance in the BFP pattern parallel to the nanowire orientation $k_{||}$ one gains direct access to the active plasmonic length of the individual nanowire, i.e. the length of the nanowire over which light is emitted via leakage radiation:

$$L_{\mathrm{wire,BFP}} = \frac{2\pi}{\Delta k_{||}}. \tag{8.13}$$

In fig. 8.12 (a) the wire length L_{BFP} determined from the BFP patterns is plotted against the length measured via AFM topography L_{AFM}. Within the margin of error all lengths extracted from the fringe distances are slightly smaller than the respective lengths determined by AFM. These differences can be attributed to a surrounding layer of PVP as shown in section 8.1 that will increase L_{AFM}. This method to extract the active plasmonic

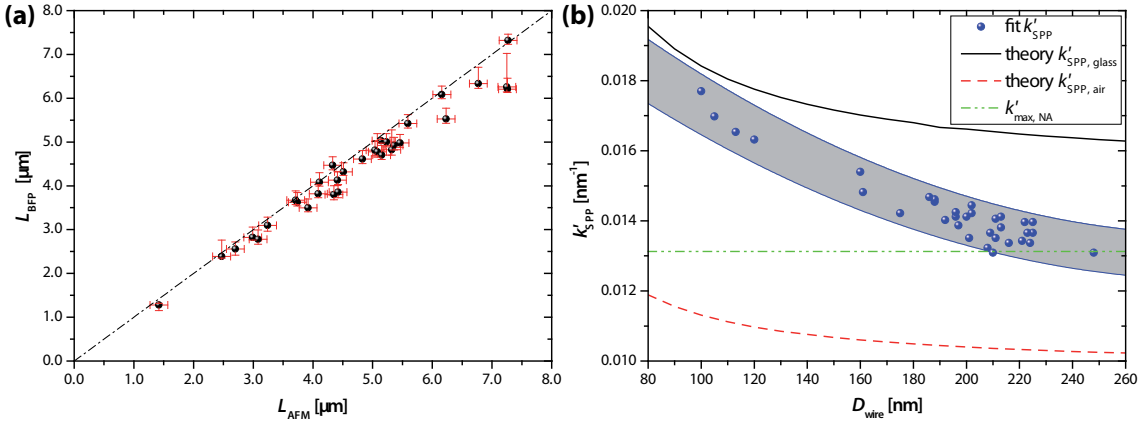

Figure 8.12: (a) Plot of the length extracted from the fringe distance in the BFP patterns L_{BFP} against the physical length measured by AFM L_{AFM} on the same nanowire. (b) The fitted k'_{SPP} is plotted against the thickness for each corresponding wire together with the uncertainty of the fit indicated by the gray shaded area. The black solid and the red dashed line represent the theoretical k values for the SPP at the metal glass interface $k'_{\mathrm{SPP,\,glass}}$ and at the metal air interface $k'_{\mathrm{SPP,\,air}}$, based on[40]. Indicated by the green dashed dotted line is the maximum detectable $k'_{\mathrm{max,\,NA}}$ with the used microscope objective (NA = 1.4).

resonator length by BFP pattern analysis exhibits a high sensitivity and offers an optical length determination without the need of additional detection techniques, such as AFM.

The finite length L of the NW over which it emits via leakage radiation leads to a fringe pattern in the BFP enabling the determination of k'_{SPP} even if k'_{SPP} lies outside the detectable wave vector range of the microscope objective as discussed in the previous section 8.3.2. In order to compare the values for k'_{SPP}, determined by fitting the BFP patterns for the different NWs with theoretical calculations, the model of thin metal cylindrical waveguides embedded in a medium[40] was used. This model was already employed for similar silver

NWs to calculate k'_{SPP} for a given wire thickness[19] and is discussed in more detail in section 2.2.3. As shown in fig. 8.12 (b) for larger NW diameters the experimental values k'_{SPP} are situated in between the theoretical k' values for the SPPs on NWs embedded in glass (black solid line) and embedded in air (red dashed line). This is a strong indication for a hybridized plasmon as described by *Shegai et al.*[19]. For decreasing wire thickness the values approach the larger and more bound $k'_{\mathrm{SPP,\,glass}}$ as shown by theoretical calculations[267].

Values for the propagation length L_D obtained from the fits show a general trend for an increasing propagation length with increasing nanowire diameter, in agreement with the literature[267]. This effect can be attributed to the increasing mode diameter for the SPP on the NW with increasing NW diameter and the associated lower losses in the metal.

Conclusion

This chapter focused on the emission channels in the vicinity of metallic nanowires. In the first step, the material composition of the silver nanowires was characterized by TEM and EDX spectroscopy. Besides the silver NWs, few copper nanoparticles embedded in a polymer layer surrounding the NWs remaining from the wire synthesis were observed. In a second step, these plasmonic NWs, deposited on a glass substrate, were combined with rare earth doped nanocrystals, which exhibit upconverted PL emission in the VIS. Radiation patterns of this coupled system were recorded in the BFP. It was found that the emission in the vicinity of a NW can be approximately described by two emission channels that can be calculated analytically: Dipolar emission, also observed in the absence of the nanowire, and leakage radiation from the nanowire. The latter can be calculated using an antenna-resonator model that considers the air-dielectric interface on which the nanowire is deposited and, additionally the position of excitation along the nanowire. Fitting of the experimentally observed patterns provides estimates of the ratio F of photons emitted via the nanowire mediated and dipolar channels with a mean value of $F = 0.7$. Finally, the fit of the back focal plane patterns gives access to the wave vector k_{SPP} of the SPP supported by the nanowire and the plasmonic active length L. These results are important for plasmonic applications of nanowires since the understanding of emission characteristics, coupling efficiency and SPP properties supported by such NWs, plays a key role in device integration.

9 Summary and outlook

In this work coupling between SPPs and different emitter systems has been investigated by the technique of BFP imaging. SPPs as surface bound electromagnetic waves propose the unique possibility to concentrate light to sub-wavelength scales and transport this energy over a length several magnitudes larger. For current efforts in the field of plasmonics towards device integration and miniaturization it is important to realize the excitation, manipulation and back conversion between light and SPPs without the need of external light sources. Thus, the integration of nanoscale emitters in a plasmonic architecture is desirable but requires a more profound knowledge about the coupling mechanism and the contributing relaxation pathways in coupled emitter-SPP systems. In order to gather detailed insight on the interaction between emitters and SPPs the focus of this work was to study single emitters in elementary plasmonic configurations that are accessible by analytical descriptions.

Next to standard microscopy methods combined BFP imaging enables access to emission characteristics, by detection of angularly resolved emission maps in the Fourier plane. Radiation channels are connected to characteristic angular distributions of emission that can be studied by BFP imaging. This technique has been used in the presented studies to determine SPP propagation and SPP properties as well as to separate and assign radiation channels.

The first key result of this work is the successful demonstration of SPPs launched by a single dipolar SWCNT emitter on a metal thin film after local optical excitation. Placing a single dipolar emitter onto a thin metal film completely reshapes the emission characteristics towards a narrow angular range in the BFP, a unique feature of propagating SPPs. Leakage radiation microscopy images in the BFP, which show two narrow crescents appearing at angles larger than the critical angle could be modeled successfully and contained the propagation length and direction of the SPPs. Corresponding real-space images revealed SPP propagation away from the single dipolar plasmon source and could be reproduced by calculations with very good agreement. The findings were further supported by a combined BFP pattern and AFM study of single SWCNTs, as well as by polarization resolved detection and subsequent BFP pattern recording. The polarization behavior of SPPs launched by single SWCNTs was found to be radial and was compared to measurements of SWCNTs on glass, which showed parallel polarization with respect to the dipole orientation. Experimentally obtained BFP patterns on both substrates could be reproduced by theoretical calculations with very good agreement. These results demonstrate

that nanotubes can act as SPP sources making them promising candidates for integration in plasmonic and nanophotonic circuits. Moreover, these results provided the basis for the successful demonstration of electrically excited SPPs by means of electroluminescent, on-chip integrated SWCNTs, achieved within cooperation [68].

The second key finding was the demonstration of remote excitation of SWCNT excitons via propagating SPPs. A scanning aperture probe was used as a SPP source enabling a fine control of the excitation position and the SPP propagation direction. First, light was coupled into an aperture probe, as used in SNOM, and was characterized regarding its SPP launching behavior when placed in close proximity to a thin metal film. Correlated real-space and BFP pattern images confirmed the SPP excitation and further revealed the influence of the fiber emission polarization on the SPP propagation direction. Second, photoluminescence images of SWCNTs, placed on the metal film, were recorded by raster-scanning the aperture probe SPP source. These images revealed an emission response from the SWCNTs while the aperture was roughly 400 nm away from the SWCNT position. This is a clear indication for remote excitation of SWCNT excitons via propagating SPPs. Theoretical modeling of the excited SPP fields showed that the SWCNT maps the SPPs locally with sub-diffraction resolution. The emission response of SWCNTs towards specific field components of an exciting SPP could also be confirmed by Rai et al. [268] who demonstrated the remote excitation efficiency as a function of relative angle and distance between the SWCNT and the SPP source.

In the last part of this work, radiation channels in the vicinity of a plasmonic nanowire were investigated. As a first step, the material composition of the silver nanowires was characterized by TEM and EDX spectroscopy. Besides the silver NWs, few copper nanoparticles, used in the wire synthesis, embedded in a polymer layer surrounding the NWs were observed. In a second step, rare earth doped nanocrystals, which exhibit upconverted PL emission in the VIS, were combined with the plasmonic NWs. Dipolar emission, also observed in the absence of the nanowire, and leakage radiation from the nanowire could be assigned and separated by analyzing recorded BFP patterns. The SPP contribution from the NW can be calculated using an antenna-resonator model that considers the air-dielectric interface on which the nanowire is deposited and the position of excitation along the nanowire. Fitting of the experimentally observed patterns provides estimates of the ratio F of photons emitted via the nanowire mediated and dipolar channels. Finally, the fit of the back focal plane patterns gives access to the wave vector k_{SPP} of the SPP supported by the NW and the plasmonic active length L. These results are important for plasmonic applications of nanowires since the understanding of emission characteristics, coupling efficiency and SPP properties supported by such NWs, plays a key role in device integration.

The use of BFP imaging could be expanded towards the observation and theoretical description of different emission processes and configurations such as optical antennas or more advanced plasmonic structures [269]. Further development of the method itself could

potentially provide access to additional quantities of investigated systems in an angularly resolved matter. One aspect of advanced BFP imaging was recently shown by Taminiau et al.[270] and Karaveli et al.[271], who combined the detection of the Fourier plane with a dispersive element and thus were able to show spectrally resolved momentum maps. The application of this method in combination with white-light reflection measurements would allow directly the recording of the dispersion relation of plasmonic metal structures and thin films. By monitoring possible changes in the dispersion relation if an emitter is placed on the metal structure the coupling regime between the SPP and the emitter system could be further investigated[58,272,273]. Another possible advancement would make use of the knowledge of the unique radiation patterns in the BFP from emitter systems. A selection of a distinct region in Fourier space by spatial filtering could enable selective measurements of properties connected to a specific radiation channel for a combined system. As an example, in the case of the presented nanocrystal-nanowire system radiation lifetimes could be measured for the coupled and uncoupled fraction of radiation at the same sample position. In summary, BFP imaging serves as a versatile optical detection method to image angular emission characteristics as unique properties of a studied system. At the same time it provides the capability to be readily integrated and combined with existing microscopy techniques.

Bibliography

[1] Ritchie, R. Plasma Losses by Fast Electrons in Thin Films. *Phys. Rev.* **1957**, *106*, 874–81.

[2] Barnes, W.; Dereux, A.; Ebbesen, T. Surface plasmon subwavelength optics. *Nature* **2003**, *424*, 824–30.

[3] Barnes, W. L. Surface plasmon-polariton length scales: a route to sub-wavelength optics. *J. Opt.* **2006**, *8*, 87–93.

[4] Oulton, R. F.; Sorger, V. J.; Genov, D. A.; Pile, D. F. P.; Zhang, X. A hybrid plasmonic waveguide for subwavelength confinement and long-range propagation. *Nat. Photonics* **2008**, *2*, 496–500.

[5] Murray, W. A.; Barnes, W. L. Plasmonic Materials. *Adv. Mater.* **2007**, *19*, 3771–82.

[6] Ozbay, E. Plasmonics: Merging photonics and electronics at nanoscale dimensions. *Science* **2006**, *311*, 189–93.

[7] Lal, S.; Hafner, J. H.; Halas, N. J.; Link, S.; Nordlander, P. Noble Metal Nanowires: From Plasmon Waveguides to Passive and Active Devices. *Acc. Chem. Res.* **2012**, *45*, 1887–95.

[8] Heeres, R. W.; Kouwenhofen, L. P.; Zwiller, V. Quantum interference in plasmonic circuits. *Nature Nanotechnol.* **2013**, *8*, 719–22.

[9] Kauranen, M.; Zayats, A. V. Nonlinear plasmonics. *Nature Photon.* **2012**, *6*, 737–48.

[10] Otto, A. Excitation of Nonradiative Surface Plasma Waves in Silver by the Method of Frustrated Total Reflection. *Z. Phys.* **1968**, *216*, 398–410.

[11] Kretschmann, E. Die Bestimmung optischer Konstanten von Metallen durch Anregung von Oberflächenplasmaschwingungen. *Z. Phys.* **1971**, *241*, 313–24.

[12] Drezet, A.; Hohenau, A.; Koller, D.; Stepanov, A.; Ditlbacher, H.; Steinberger, B.; Aussenegg, F. R.; Leitner, A.; Krenn, J. R. Leakage radiation microscopy of surface plasmon polaritons. *Mater. Sci. Eng. B* **2008**, *149*, 220–29.

[13] Lieb, M. A.; Zavislan, J. M.; Novotny, L. Single-molecule orientations determined by direct emission pattern imaging. *J. Opt. Soc. Am. B* **2004**, *21*, 1210–15.

[14] Hohenau, A.; Krenn, J. R.; Drezet, A.; Mollet, O.; Huant, S.; Genet, C.; Stein, B.; Ebbesen, T. W. Surface plasmon leakage radiation microscopy at the diffraction limit. *Opt. Express* **2011**, *19*, 25749–62.

[15] Zhang, D. G.; Fu, Q.; Wang, X. X.; Chen, Y. K.; Wang, P.; Ming, H. Charaterization of a dye doped planar polymer waveguide by leakage radiation microscopy. *J. Opt.* **2012**, *14*, 015003.

[16] Berthelot, J.; Tantussi, F.; Rai, P.; Colas des Francs, G.; Weeber, J.-C.; Bereux, A.; Fuso, F.; Allegrini, M.; Bouhelier, A. Determinant role of the edges in defining surface plasmon propagation in stripe waveguides and tapered concentrators. *J. Opt. Soc. Am. B* **2012**, *29*, 226–31.

[17] Descrovi, E.; Barakat, E.; Angelini, A.; Munzert, P.; De Leo, N.; Boarino, L.; Giorgis, F.; Herzig, H. P. Leakage radiation interference microscopy. *Opt. Lett.* **2013**, *38*, 3374–76.

[18] Archambault, A.; Teperik, T. V.; Marquier, F.; Greffet, J. J. Surface plasmon Fourier optics. *Phys. Rev. B* **2009**, *79*, 195414–22.

[19] Shegai, T.; Miljković, V. D.; Bao, K.; Xu, H.; Nordlander, P.; Johansson, P.; Käll, M. Unidirectional Broadband Light Emission from Supported Plasmonic Nanowires. *Nano Lett.* **2011**, *11*, 706–11.

[20] Taminiau, T. H.; Stefani, F. D.; van Hulst, N. F. Optical Nanorod Antennas Modeled as Cavities for Dipolar Emitters: Evolution of Sub- and Super-Radiant Modes. *Nano Lett.* **2011**, *11*, 1020–24.

[21] Bharadwaj, P.; Bouhelier, A.; Novotny, L. Electrical Excitation of Surface Plasmons. *Phys. Rev. Lett.* **2011**, *106*, 226802.

[22] Zhang, Y.; Boer-Duchemin, E.; Wang, T.; Rogez, B.; Comtet, G.; Le Moal, E.; Dujardin, G.; Hohenau, A.; Gruber, C.; Krenn, J. R. Edge scattering of surface plasmons excited by scanning tunneling microscopy. *Opt. Expr.* **2013**, *21*, 13938–48.

[23] Zenneck, J. Über die Ausbreitung der Wellen in der drahtlosen Telegraphie. *Ann. Phys.* **1909**, *333*, 665–736.

[24] Sommerfeld, A. Über die Fortpflanzung ebener elektromagnetischer Wellen längs einer ebenen Leiterfläche und ihre Beziehung zur drahtlosen Telegraphie. *Ann. Phys.* **1907**, *328*, 846–66.

[25] Powell, C.; Swan, J. Effect of Oxidation on the Characteristic Loss Spectra of Aluminum and Magnesium. *Phys. Rev.* **1960**, *118*, 640–43.

[26] Gramotnev, D. K.; Bozhevolnyi, S. I. Plasmonics beyond the diffraction limit. *Nat. Photonics* **2010**, *4*, 83–91.

[27] Gan, Q.; Bartoli, F. J.; Kafafi, Z. H. Plasmonic-Enhanced Organic Photovoltaics: Breaking the 10% Efficiency Barrier. *Adv. Mater.* **2013**, *25*, 2385–96.

[28] Roh, S.; Chung, T.; Lee, B. Overview of the Characteristics of Mirco- and Nano-Structured Surface Plasmon Resonance Sensors. *Sensors* **2011**, *11*, 1565–88.

[29] Szunerits, S.; Boukherroub, R. Sensing using localised surface plasmon resonance sensors. *Chem. Commun.* **2012**, *48*, 8999–9010.

[30] Berini, P.; De Leon, I. Surface plasmon-polariton amplifier and lasers. *Nat. Photonics* **2012**, *6*, 16–24.

[31] Maier, S. A., Ed. *Plasmonics: Fundamentals and Applications*, 1st ed.; Springer, 2007.

[32] Raether, H. *Surface Plasmons on Smooth and Rough Surfaces and on Gratings*; Springer, 1986.

[33] Novotny, L.; Hecht, B. *Principles of Nano-Optics*, 2nd ed.; Cambridge University Press, 2012.

[34] Marti, O.; Bielefeld, H.; Hecht, B.; Leiderer, P.; Mlynek, J. Near-field optical measurement of the surface plasmon field. *Opt. Commun.* **1993**, *96*, 225–28.

[35] Johnson, P. B.; Christy, R. W. Optical Constants of Noble Metals. *Phys. Rev. B* **1972**, *6*, 4370–79.

[36] Arakawa, E. T.; Williams, M. W.; Hamm, R. N.; Ritchie, R. H. Effect of Damping on Surface Plasmon Dispersion. *Phys. Rev. Lett.* **1973**, *31*, 1127–29.

[37] Pockrand, I. Surface plasma oscillations at silver surfaces with thin transparent and absorbing coatings. *Surf. Sci.* **1978**, *72*, 577–88.

[38] Hondros, D. Über elektromagnetische Drahtwellen. *Ann. Phys.* **1909**, *335*, 905–50.

[39] Neubrech, F.; Kolb, T.; Lovrincic, R.; Fahsold, G.; Pucci, A. Resonances of individual metal nanowires in the infrared. *Appl. Phys. Lett.* **2006**, *89*, 253104.

[40] Novotny, L. Effective Wavelength Scaling for Optical Antennas. *Phys. Rev. Lett.* **2007**, *98*, 266802.

[41] Novotny, L.; Hafner, C. Light propagation in a cylindrical waveguide with a complex, metallic, dielectric function. *Phys. Rev. E* **1994**, *50*, 4094–106.

[42] Burke, J. J.; Stegeman, G. I.; Tamir, T. Surface-polariton-like waves guided by thin, lossy metal films. *Phys. Rev. B* **1986**, *33*, 5186–5201.

[43] Zayats, A. V.; Smolyaninov, I. I.; Maradudin, A. A. Nano-optics of surface plasmon polaritons. *Phys. Rep.* **2005**, *408*, 131–314.

[44] Kano, H.; Mizuguchi, S.; Kawata, S. Excitation of surface-plasmon polaritons by a focused laser beam. *J. Opt. Soc. Am. B* **1998**, *15*, 1381–86.

[45] Bouhelier, A.; Wiederrecht, G. P. Excitation of broadband surface plasmon polaritons: Plasmonic continuum spectroscopy. *Phys. Rev. B* **2005**, *71*, 195406.

[46] Bouhelier, A.; Ignatovich, F.; Bruyant, A.; Huang, C.; Colas des Francs, G.; Weeber, J.-C.; Deeux, A.; Wiederrecht, G. P.; Novotny, L. Surface plasmon interference excited by tightly focused laser beams. *Opt. Lett.* **2007**, *32*, 2535–37.

[47] Wood, R. W. On a Remarkable Case of Uneven Distribution of Light in a Diffraction Grating Spectrum. *Proc. Phys. Soc. London* **1902**, *18*, 269–75.

[48] Hecht, E. *Optics*, 4th ed.; Addison Wesley, 2002.

[49] Ropers, C.; Neacsu, C. C.; Elsaesser, T.; Albrecht, M.; Raschke, M. B.; Lienau, C. Grating-Coupling of Surface Plasmons onto Metallic Tips: A Nanoconfined Light Source. *Nano Lett.* **2007**, *7*, 2784–88.

[50] Lezec, H. J.; Degiron, A.; Devaux, E.; Linke, R. A.; Martin-Moreno, L.; Garcia-Vidal, F. J.; Ebbesen, T. W. Beaming Light from a Subwavelength Aperture. *Science* **2002**, *297*, 820–22.

[51] Ditlbacher, H.; Krenn, J.; Schider, G.; Leitner, A.; Aussenegg, F. R. Two-dimensional optics with surface plasmon polaritons. *Appl. Phys. Lett.* **2002**, *81*, 1762.

[52] Ditlbacher, H.; Krenn, J. R.; Hohenau, A.; Leitner, A.; Aussenegg, F. R. Efficiency of local light-plasmon coupling. *Appl. Phys. Lett.* **2003**, *83*, 3665.

[53] Hecht, B.; Bielefeldt, H.; Novotny, L.; Inoue, Y.; Pohl, D. W. Local Excitation, Scattering, and Interference of Surface Plasmons. *Phys. Rev. Lett.* **1996**, *77*, 1889–92.

[54] Baudrion, A.-L.; de Leon-Perez, F.; Mahboub, O.; Hohenau, A.; Ditlbacher, H.; Garcia-Vidal, F. J.; Dintinger, J.; Ebbesen, T. W.; Martin-Moreno, L.; Krenn, J. R. Coupling efficiency of light to surface plasmon polariton for single subwavelength holes in a gold film. *Opt. Expr.* **2008**, *16*, 3420–29.

[55] Lalulet, J.-Y.; Drezet, A.; Genet, C.; Ebbesen, T. W. Generation of surface plasmons at single subwavelength slits: from slit to ridge plasmon. *New J. Phys.* **2008**, *10*, 105014.

[56] Pockrand, I.; Brillante, A.; Möbius, D. Exciton-surface plasmon coupling: An experimental investigation. *J. Chem. Phys.* **1982**, *77*, 6289–95.

[57] Lakowicz, J. Radiative decay engineering 3. Surface plasmon-coupled directional emission. *Anal. Biochem.* **2004**, *324*, 153–69.

[58] Bellessa, J.; Bonnand, C.; Plenet, J. C.; Mugnier, J. Strong Coupling between Surface Plasmons and Excitons in an Organic Semiconductor. *Phys. Rev. Lett* **2004**, *93*, 036404.

[59] Fedutik, Y.; Temnov, V.; Woggon, U.; Ustinovich, E.; Artemyev, M. Exciton-Plasmon Interaction in a Composite Metal-Insulator-Semiconductor Nanowire System. *J. Am. Chem. Soc.* **2007**, *129*, 14939–45.

[60] Hakala, T.; Toppari, J.; Kuzyk, A.; Pettersson, M.; Tikkanen, H.; Kunttu, H.; Törmä, P. Vacuum Rabi Splitting and Strong-Coupling Dynamics for Surface-Plasmon Polaritons and Rhodamine 6G Molecules. *Phys. Rev. Lett.* **2009**, *103*, 053602.

[61] Valmorra, F.; Bröll, M.; Schwaiger, S.; Welzel, N.; Heitmann, D.; Mendach, S. Strong coupling between surface plasmon polariton and laser dye rhodamine 800. *Appl. Phys. Lett.* **2011**, *99*, 051110.

[62] Akimov, A. V.; Mukherjee, A.; Yu, C. L.; Chang, D. E.; Zibrov, A. S.; Hemmer, P. R.; Park, H.; Lukin, M. D. Generation of single optical plasmons in metallic nanowires coupled to quantum dots. *Nature* **2007**, *450*, 402–6.

[63] Kolesov, R.; Grotz, B.; Balasubramanian, G.; Stö, R. J.; Nicolet, A. A. L.; Hemmer, P. R.; Jelezko, F.; Wrachtrup, J. Wave-particle duality of single surface plasmon polaritons. *Nat. Phys.* **2009**, *5*, 470–74.

[64] Gruber, C.; Trügler, A.; Hohenau, A.; Hohenester, U.; Krenn, J. R. Spectral Modifications and Polarization Dependent Coupling in Tailored Assemblies of Quantum Dots and Plasmonic Nanowires. *Nano Lett.* **2013**, *9*, 1–6.

[65] Walters, R. J.; van Loon, R. V. A.; Brunets, I.; Schmitz, J.; Polman, A. A silicon-based electrical source of surface plasmon polaritons. *Nat. Mater.* **2010**, *9*, 21–5.

[66] Wang, L.; Li, T.; Li, L.; Xia, W.; Xu, X. G.; Zhu, S. N. Electrically generated unidirectional surface plasmon source. *Opt. Expr.* **2012**, *20*, 8710–17.

[67] Koller, D. M.; Hohenau, H., A. Ditlbacher; Galler, N.; Reil, F.; Aussenegg, F. R.; Leitner, A.; List, E. J. W.; Krenn, J. R. Organic plasmon-emitting diode. *Nat. Photon.* **2008**, *2*, 684–87.

[68] Rai, P.; Hartmann, N.; Berthelot, J.; Arocas, J.; Colas des Francs, G.; Hartschuh, A.; Bouhelier, A. Electrical Excitation of Surface Plasmons by an Individual Carbon Nanotube Transistor. *Phys. Rev. Lett.* **2013**, *111*, 026804.

[69] Sönnichsen, C.; Duch, A. C.; Steininger, G.; Koch, M.; von Plessen, G.; Feldmann, J. Launching surface plasmons into nanoholes in metal films. *Appl. Phys. Lett.* **2000**, *76*, 140–42.

[70] Baida, F. I.; Van Labeke, D.; Bouhelier, A.; Huser, T.; Pohl, D. W. Propagation and diffraction of locally excited surface plasmons. *J. Opt. Soc. Am. A* **2001**, *18*, 1552–61.

[71] Brun, M.; Drezet, A.; Mariette, H.; Chevalier, N.; Woehl, J. C.; Huant, S. Remote optical adressing of single nano-objects. *Europhys. Lett.* **2003**, *64*, 634–40.

[72] Mollet, O.; Cuche, A.; Drezet, A.; Huant, S. Leakage radiation microscopy of surface plasmons launched by a nanodiamond-based tip. *Diam. Relat. Mater.* **2011**, *20*, 995–98.

[73] Raether, H. *Excitation of Plasmons and Interband Transitions by Electrons*; Springer Tracts in Modern Physics; Springer, 1980; Vol. 88.

[74] Rocca, M. Low-energy EELS investigation of surface electronic excitations on metals. *Surf. Sci. Rep.* **1995**, *22*, 1–71.

[75] Marty, R.; Girard, C.; Arbouet, G., A. Colas des Francs Near-field coupling of a point-like dipolar source with a thin metallic film: Implication for STM plasmon excitation. *Chem. Phys. Lett.* **2012**, *532*, 100–5.

[76] Simon, H. J.; Guha, J. K. Directional surface plasmon scattering from silver films. *Opt. Commun.* **1976**, *18*, 391–94.

[77] Bouhelier, A.; Huser, T.; Tamaru, H.; Güntherodt, H.-J.; Pohl, D. W.; Baida, F. I.; Van Labeke, D. Plasmon optics of structured silver films. *Phys. Rev. B* **2001**, *63*, 155404.

[78] Krenn, J. R.; Weeber, J.-C. Surface plasmon polaritons in metal stripes and wires. *Phil. Trans. R. Soc. Lond. A* **2004**, *362*, 739–56.

[79] Ditlbacher, H.; Krenn, J. R.; Leitner, A.; Aussenegg, F. R. Surface plasmon polariton-based optical beam profiler. *Opt. Lett.* **2004**, *29*, 1408–10.

[80] Stepanov, A. L.; Krenn, J. R.; Ditlbacher, H.; Hohenau, A.; Drezet, A.; Steinberger, B.; Leitner, A.; Aussenegg, F. A. Quantitative analysis of surface plasmon interaction with silver nanoparticles. *Opt. Lett.* **2005**, *30*, 1524–26.

[81] Dawson, P.; de Fornel, F.; Goudonnet, J.-P. Imaging of Surface Plasmon Propagation and Edge Interaction Using a Photon Scanning Tunneling Microscope. *Phys. Rev. Lett.* **1994**, *72*, 2927–30.

[82] Dawson, P.; Puygranier, B. A. F.; Goudonnet, J.-P. Surface plasmon propagation length: A direct comparison using photon scanning tunneling microscopy and attenuated total reflection. *Phys. Rev. B* **2001**, *63*, 205410.

[83] Weeber, J.-C.; Krenn, J. R.; Dereux, A.; Lamprecht, B.; Lacroute, Y.; Goudonnet, J. P. Near-field observation of surface plasmon polariton propagation on thin metal stripes. *Phys. Rev. B* **2001**, *64*, 045411.

[84] Karrai, K.; Grober, R. D. Piezoelectric tipsample distance control for near field optical microscopes. *Appl. Phys. Lett.* **1995**, *66*, 1842–44.

[85] Adam, P. M.; Salomon, L.; de Fornel, F.; Goudonnet, J. P. Determination of the spatial extension of the surface-plasmon evanescent field of a silver film with a photon scanning tunneling microscope. *Phys. Rev. B* **1993**, *48*, 2680–83.

[86] Yin, L.; Vlasko-Vlasov, V. K.; Rydh, A.; Pearson, J.; Welp, U.; Chang, S.-H.; Gray, S. K.; Schatz, G. C.; Brown, D. B.; Kimball, C. W. Surface plasmons at single nanoholes in Au films. *Appl. Phys. Lett.* **2004**, *85*, 467–69.

[87] Ditlbacher, H.; Hohenau, A.; Wagner, D.; Kreibig, U.; Rogers, M.; Hofer, F.; Aussenegg, F. R.; Krenn, J. R. Silver Nanowires as Surface Plasmon Resonators. *Phys. Rev. Lett.* **2005**, *95*, 257403.

[88] Laroche, T.; Girard, C. Near-field optical properties of single plasmonic nanowires. *Appl. Phys. Lett.* **2006**, *89*, 233119.

[89] Krenn, J. R.; Dereux, A.; Weeber, J. C.; Bourillot, E.; Lacroute, Y.; Goudonnet, J. P.; Schider, G.; Gotschy, W.; Leitner, A.; Aussenegg, F. R.; Girard, C. Squeezing the Optical Near-Field Zone by Plasmon Coupling of Metallic Nanoparticles. *Phys. Rev. B* **1993**, *48*, 2680–83.

[90] Denkova, D.; Verellen, N.; Silhanek, A. V.; Valev, V. K.; Van Dorpe, P.; Moshchalkov, V. V. Mapping Magnetic Near-Field Distributions of Plasmonic Nanoantennas. *ACS Nano* **2013**, *7*, 3168–76.

[91] Yin, L.; Vlasko-Vlasov, V. K.; Pearson, J.; Hiller, J. M.; Hua, J.; Welp, U.; Brown, D. E.; Kimball, C. W. Subwavelength Focusing and Guiding of Surface Plasmons. *Nano Lett.* **2005**, *5*, 1399–402.

[92] Kihm, H. W.; Kim, J.; Koo, S.; Ahn, J.; Ahn, K.; Lee, K.; Park, N.; Kim, D.-S. Optical magnetic field mapping using a subwavelength aperture. *Opt. Express* **2013**, *21*, 5625–33.

[93] Fort, E.; Grésillon, S. Surface enhanced fluorescence. *J. Phys. D* **2008**, *41*, 013001.

[94] Ditlbacher, H.; Krenn, J. R.; Felidj, N.; Lamprecht, B.; Schider, G.; Salerno, M.; Leitner, A.; Aussenegg, F. R. Fluorescence imaging of surface plasmon fields. *Appl. Phys. Lett.* **2002**, *80*, 404–6.

[95] Chance, R. R.; Prock, A.; Silbey, R. *Molecular fluorescence and energy transfer near interfaces*; Advances in Chemical Physics; Wiley & Sons, 2007; Vol. 37.

[96] Solis, D.; Chang, W.-C.; Khanal, B. P.; Bao, K.; Nordlander, P.; Zubarev, E. R.; Link, S. Bleach-Imaged Plasmon Propagation (BlIPP) in Single Gold Nanowires. *Nano Lett.* **2010**, *10*, 3482–85.

[97] Kubitschek, U., Ed. *Fluorescence Microscopy - From Principles to Biological Applications*, 1st ed.; Wiley-Blackwell, 2013.

[98] Hartschuh, A. Tip-Enhanced Near-Field Optical Microscopy. *Angew. Chem. Int. Ed.* **2008**, *47*, 8178–91.

[99] Hartschuh, A.; Qian, H.; Böhmler, M.; Georgi, C. Tip-enhanced near-field optical microscopy of carbon nanotubes. *Anal. Biochem. Chem.* **2009**, *394*, 1787–95.

[100] Böhmler, M.; Wang, Z.; Myalitsin, A.; Mews, A.; Hartschuh, A. Optical Imaging of CdSe Nanowires with Nanoscale Resolution. *Angew. Chem. Int. Ed.* **2011**, *50*, 11536–38.

[101] Huang, B.; Bates, M.; Zhuang, X. Super-Resolution Fluorescence microscopy. *Annu. Rev. Biochem.* **2009**, *78*, 993–1016.

[102] Müller, T.; Schumann, C.; Kraegeloh, A. STED Microscopy and its Applications: New Insights into Cellular Processes on the Nanoscale. *ChemPhysChem* **2012**, *13*, 1986–2000.

[103] Huang, C.; Bouhelier, A.; Colas des Francs, G.; Bruyant, A.; Guenot, A.; Finot, E.; Weeber, J.-C.; Dereux, A. Gain, detuning, and radiation patterns of nanoparticle optical antennas. *Phys. Rev. B* **2008**, *78*, 155407.

[104] Bharadwaj, P.; Deutsch, B.; Novotny, L. Optical Antennas. *Adv. Opt. Photon.* **2009**, *1*, 438–83.

[105] Böhmler, M.; Hartmann, N.; Georgi, C.; Hennrich, F.; Green, A. A.; Hersam, M. C.; Hartschuh, A. Enhancing and redirecting carbon nanotube photoluminescence by an optical antenna. *Opt. Express* **2010**, *18*, 16443–51.

[106] Taminiau, T. H.; Stefani, F. D.; Segerink, F. B.; Van Hulst, N. F. Optical antennas direct single-molecule emission. *Nat. Photonics* **2008**, *2*, 234–37.

[107] Schuller, J. A.; Karaveli, S.; Schiros, T.; He, K.; Yang, S.; Kymissis, I.; Shan, J.; Zia, R. Orientation of luminescent excitons in layered nanomaterials. *Nat. Nanotechnol.* **2013**, *8*, 271–76.

[108] Otsuki, S.; Murase, N.; Kano, H. Back focal plane microscopic ellipsometer with internal reflection geometry. *Opt. Commun.* **2013**, *294*, 24–28.

[109] Novotny, L. Allowed and forbidden light in near-field optics. I. A single dipole. *J. Opt. Soc. Am. A* **1997**, *14*, 91–104.

[110] Bömler, M. Tip-enhanced near-field optical microscopy on the quasi 1D semiconductors carbon nanotubes and CdSe nanowires. Ph.D. thesis, Ludwig-Maximilians-Universität München, 2012.

[111] Hartmann, N. Räumliche Abstrahlcharakteristiken von Kohlenstoffnanoröhren und deren Manipulation. M.Sc. thesis, Ludwig-Maximilians-Universität München, 2009.

[112] Weyl, H. Ausbreitung elektromagnetischer Wellen über einem ebenen Leiter. *Ann. Phys.* **1919**, *365*, 481–500.

[113] Born, M.; Wolf, E. *Principles of Optics*, 6th ed.; Cambridge University Press, 2006.

[114] Wilson, T.; Juskaitis, R. The axial response of confocal microscopes with high numerical aperture objective lenses. *Bioimaging* **1995**, *3*, 35–8.

[115] Tang, W. T.; Chung, E.; Kim, Y.-H.; So, P. T. C.; Sheppard, C. J. R. Investigation of the point spread function of surface plasmon-coupled emission microscopy. *Opt. Express* **2007**, *15*, 4634–46.

[116] Fattinger, C.; Lukosz, W. Optical-environment-dependent lifetimes and radiation patterns of luminescent centers in very thin films. *J. Lumin.* **1984**, *31*, 933–35.

[117] Zhang, J.; See, C. W.; Somekh, M. G.; Pitter, M. C.; Liu, S. G. Wide-field surface plasmon microscopy with solid immersion excitation. *Appl. Phys. Lett.* **2004**, *85*, 5451–53.

[118] Stabler, G.; Somekh, M. G.; See, C. W. High resolution wide-field surface plasmon mircoscopy. *J. Microsc.* **2004**, *214*, 328–33.

[119] Moh, K. J.; Yuan, X.-C.; Bu, J.; Zhu, S. W.; Gao, B. Z. Surface plasmon resonance imaging of cell-substrate contacts with radially polarized beams. *Opt. Express* **2008**, *16*, 20734–41.

[120] Zhang, D. G.; Yuan, X.-C.; Yuan, G. H.; Wang, P.; Ming, H. Directional fluorescence emission characterized with leakage radiation microscopy. *J. Opt.* **2010**, *12*, 035002.

[121] Huang, B.; Yu, F.; Zare, R. N. Surface Plasmon Resonance imaging Using a High Numerical Aperture Microscope Objective. *Anal. Chem.* **2007**, *79*, 2979–83.

[122] Berthelot, J.; Bouhelier, A.; Colas des Francs, G.; Weeber, J.-C.; Dereux, A. Excitation of a one-dimensional evanescent wave by conical edge diffraction of surface plasmon. *Opt. Express* **2011**, *19*, 5303–12.

[123] Song, M.; Bouhelier, A.; Bramant, P.; Sharma, J.; Dujardin, E.; Zhang, D.; Colas des Francs, G. Imaging Symmetry-Selected Corner Plasmon Modes in Penta-Twinned Crystalline Ag Nanowires. *ACS Nano* **2011**, *5*, 5874–80.

[124] Gryczynski, I.; Malicka, J.; Gryczynski, Z.; Lakowicz, J. R. Radiative decay engineering 4. Experimental studies of surface plasmon-coupled directional emission. *Anal. Biochem.* **2004**, *324*, 170–82.

[125] Enderlein, J.; Ruckstuhl, T. The efficiency of surface-plasmon coupled emission for sensitive fluorescence detection. *Opt. Express* **2005**, *13*, 8855–65.

[126] Zhang, D. G.; Moh, K. J.; Yuan, X.-C. Surface plasmon-coupled emission from shaped PMMA films doped with fluorescence molecules. *Opt. Express* **2010**, *18*, 12185–90.

[127] Chen, Y.; Zhang, D.; Han, L.; Rui, G.; Xinagxian, W.; Wang, P.; Ming, H. Surface-plasmon-coupled emission microscopy with a polarization converter. *Opt. Lett.* **2013**, *38*, 736–38.

[128] Cao, Q.; Hur, S.-H.; Zhu, Z.-T.; Sun, Y.; Wang, C.; Meitl, M. A.; Shim, M.; Rogers, J. A. Highly Bendable, Transparent Thin-Film Transistors That Use Carbon-Nanotube-Based Conductors and Semiconductors with Elastomeric Dielectrics. *Adv. Mater.* **2006**, *18*, 304–9.

[129] Snow, E. S.; Perkins, F. K.; Houser, E. J.; Badescu, S. C.; Reinecke, T. L. Chemical detection with a single-walled carbon nanotube capacitor. *Science* **2005**, *307*, 1942–45.

[130] Yang, L.; Wang, S.; Zheng, Q.; Zhang, Z.; Peng, L.-M. Carbon Nanotube Photoelectronic and Photovoltaic Devices and their Applications in Infrared Detection. *Small* **2013**, *9*, 1225–36.

[131] Dai, L.; Channg, D. W.; Baek, J.-B.; Lu, W. Carbon Nanomaterials for Advanced Energy Conversion and Storage. *Small* **2012**, *8*, 1130–66.

[132] Engel, M.; Small, J. P.; Steiner, M.; Freitag, M.; Green, A. A.; Hersam, M. C.; Avouris, P. Thin Film Nanotube Transistors Based on Self-Assembled, Aligned, Semiconducting Carbon Nanotube Arrays. *ACS Nano* **2008**, *2*, 2445–52.

[133] Kinoshita, M.; Steiner, M.; Engel, M.; Small, J. P.; Green, A. A.; Hersam, M. C.; Krupke, R.; Mendez, E. E.; Phaedon, A. The polarized carbon nanotube thin film LED. *Opt. Express* **2010**, *18*, 25738–45.

[134] Pfeiffer, M. H. P.; Stürzl, N.; Marquardt, C. W.; Engel, M.; Dehm, S.; Hennrich, F.; Kappes, M. M.; Lemmer, U.; Krupke, R. Electroluminescence from chirality-sorted (9,7)-semiconducting carbon nanotube devices. *Opt. Express* **2011**, *19*, 1184–89.

[135] Reich, S.; Thomsen, C.; Maultzsch, J. *Carbon Nanotubes*; Wiley-VCH: Weinheim, 2004.

[136] Georgi, C. Exciton Mobility and Localized Defects in Single Carbon Nanotubes Studied with Tip-Enhanced Near-Field Optical Microscopy. Ph.D. thesis, Ludwig-Maximilians-Universität München, 2011.

[137] Dukovic, G.; Balaz, M.; Doak, P.; Berova, N. D.; Zheng, M.; Mclean, R. S.; Brus, L. E. Racemic Single-Walled Carbon Nanotubes Exhibit Circular Dichroism When Wrapped with DNA. *J. Am. Chem. Soc.* **2006**, *128*, 9004–5.

[138] Akazaki, K.; Toshimitsu, F.; Ozawa, H.; Fujigaya, T.; Nakashima, N. Recognition and One-Pot Extraction of Right- and Left-Handed Semiconducting Single-Walled Carbon Nanotube Enantiomers Using Fluorene-Binaphthol Chiral Copolymers. *J. Am. Chem. Soc.* **2012**, *134*, 12700–7.

[139] Jorio, A., Dresselhaus, M. S., Dresselhaus, G., Eds. *Carbon Nanotubes*; Topics in Applied Physics; Springer: Berlin / Heidelberg, 2008; Vol. 111.

[140] Gokus, T. Time-Resolved Photoluminescence and Elastic White Light Scattering of Individual Carbon Nanotubes and Optical Characterization of Oxygen Plasma Treated Graphene. Ph.D. thesis, Ludwig-Maximilians-Universität München, 2011.

[141] Qian, H. Tip-Enhanced Near-Field Optical Spectroscopy on Single-Walled Carbon Nanotubes. Ph.D. thesis, Ludwig-Maximilians-Universität München, 2008.

[142] Saito, R.; Dresselhaus, G.; Dresselhaus, M. S. Physical Properties of Carbon Nanotubes. **1998**,

[143] Ferrari, A. C.; Basko, D. M. Raman spectroscopy as a versatile tool for studying the properties of graphene. *Nat. Nanotechnol.* **2013**, *8*, 235–46.

[144] Kuzmany, H.; Pfeiffer, R.; Hulman, M.; Kramberger, C. Raman spectroscopy of fullerenes and fullerene-nanotube composites. *Phil. Trans. R. Soc. Lond. A* **2004**, *362*, 2375–406.

[145] Miyauchi, Y.; Oba, M.; Maruyama, S. Cross-polarized optical absorption of single-walled nanotubes by polarized photoluminescence excitation spectroscopy. *Phys. Rev. B* **2006**, *74*, 205440.

[146] Lefebvre, J.; Finnie, P. Polarized Photoluminescence Excitation Spectroscopy of Single-Walled Carbon Nanotubes. *Phys. Rev. Lett.* **2007**, *98*, 167406.

[147] Maultzsch, J.; Pomraenke, R.; Reich, S.; Chang, E.; Prezzi, D.; Ruini, A.; Molinari, E.; Strano, M. S.; Thomsen, C.; Lienau, C. Exciton binding energies in carbon nanotubes from two-photon photoluminescence. *Phys. Rev. B* **2005**, *72*, 241402.

[148] Walsh, A. G.; Vamivakas, A. N.; Yin, Y.; Cronin, S. B.; Ünlü, M. S.; Goldberg, B. B.; Swan, A. K. Scaling of exciton binding energy with external dielectric function in carbon nanotubes. *Physica E* **2008**, *40*, 2375–79.

[149] Okazaki, T.; Saito, T.; Matsuura, K.; Ohshima, S.; Yumura, M.; Iijima, S. Photoluminescence Mapping of "As-Grown" Single-Walled Carbon Nanotubes: A Comparison with Micelle-Encapsulated Nanotube Solutions. *Nano Lett.* **2005**, *5*, 2618–23.

[150] Ohno, Y.; Iwasaki, S.; Murakami, Y.; Kishimoto, S.; Maruyama, S.; Mizutani, T. Chirality-dependent environmental effects in photoluminescence of single-walled carbon nanotubes. *Phys. Rev. B* **2006**, *73*, 235427.

[151] Dyatlowa, O. A.; Gomis-Bresco, J.; Malic, E.; Telg, H.; Maultzsch, J.; Zhong, G.; Geng, J.; Woggon, U. Dielectric screeing effects on transistion energies in aligned carbon nanotubes. *Phys. Rev. B* **2012**, *85*, 245449.

[152] Siitonen, A. J.; Tsyboulski, D. A.; Bachilo, S. M.; Weisman, R. B. Surfactant-Dependent Exciton Mobility in Single-Walled Carbon Nanotubes Studied by Single-Molecule Reactions. *Nano Lett.* **2010**, *10*, 1595–99.

[153] Georgi, C.; Böhmler, M.; Qian, H.; Novotny, L.; Hartschuh, A. Probing exciton propagation and quenching in carbon nanotubes with near-field optical microscopy. *Phys. Status Solidi B* **2009**, *246*, 2683–88.

[154] Manzoni, C.; Gambetta, A.; Menna, E.; Meneghetti, M.; Lanzani, G.; Cerullo, G. Intersubband Exciton Relaxation Dynamics in Single-Walled Carbon Nanotubes. *Phys. Rev. Lett.* **2005**, *94*, 207401.

[155] Hertel, T.; Perebeinos, V.; Crochet, J.; Arnold, K.; Kappes, P., M. abd Avouris Intersubband Decay of 1-D Exciton Resonances in Carbon Nanotubes. *Nano Lett.* **2008**, *8*, 87–91.

[156] Torrens, O. N.; Zheng, M.; Kikkawa, J. M. Energy of K-Momentum Dark Excitons in Carbon Nanotubes by Optical Spectroscopy. *Phys. Rev. Lett.* **2008**, *101*, 157401.

[157] Harutyunyan, H.; Gokus, T.; Green, A. A.; Hersam, M. C.; Allegrini, M.; Hartschuh, A. Defect-Induced Photoluminescence from Dark Excitonic States in Individual Single-Walled Carbon Nanotubes. *Nano Lett.* **2009**, *9*, 2010–14.

[158] Kinder, J. M.; Mele, E. J. Nonradiative recombination of excitons in carbon nanotubes mediated by free charge carriers. *Phys. Rev. B* **2008**, *78*, 155429.

[159] Berciaud, S.; Cognet, L.; Lounis, B. Luminescence Decay and the Absorption Cross Section of individual Single-Walled Carbon Nanotubes. *Phys. Rev. Lett.* **2008**, *101*, 077402.

[160] Gokus, T.; Cognet, L.; Duque, J. G.; Pasquali, M.; Hartschuh, A.; Lounis, B. Mono- and Biexponential Luminescence Decays of Individual Single-Walled Carbon Nanotubes. *J. Phys. Chem. C* **2010**, *114*, 14025–28.

[161] Miyauchi, Y.; Matsuda, K.; Yamamoto, Y.; Nakashima, N.; Kanemitsu, Y. Length-Dependent Photoluminescence Lifetimes in Single-Walled Carbon Nanotubes. *J. Phys. Chem. C* **2010**, *114*, 12905–8.

[162] Lefebvre, J.; Austing, D. G.; Bond, J.; Finnie, P. Photoluminescence Imaging of Suspended Single-Walled Carbon Nanotubes. *Nano Lett.* **2006**, *6*, 1603–8.

[163] O'Connell, M. J.; Bachilo, S. M.; huffman, C. B.; Moore, V. C.; Strano, M. S.; Haroz, E. H.; Rialon, K. L.; Boul, P. J.; Noon, W. H.; Kittrell, C.; Ma, J.; Hauge, R. H.; Weisman, R. B.; Smalley, R. E. Band Gap Fluorescence from individual Single-Walled Carbon Nanotubes. *Science* **2002**, *297*, 593–6.

[164] Wang, F.; Dukovic, G.; Brus, L. E.; Heinz, T. F. Time-Resolved Fluorescence of Carbon Nanotubes and Its Implication for Radiative Lifetimes. *Phys. Rev. Lett.* **2004**, *92*, 177401.

[165] Crochet, J.; Clemens, M.; Hertel, T. Quantum Yield Heterogeneities of Aqueous Single-Wall Carbon Nanotube Suspensions. *J. Am. Chem. Soc.* **2007**, *129*, 8058–59.

[166] Bachilo, S. M.; Strano, M. S.; Kittrell, C.; Hauge, R. H.; Smalley, R. E.; Weisman, R. B. Structure-Assigned Optical Spectra of Single-Walled Carbon Nanotubes. *Science* **2002**, *298*, 2361–66.

[167] Das, A.; Sood, A. K.; Govindaraj, A.; Saitta, A. M.; Lazzeri, M.; Mauri, F.; Rao, C. N. R. Doping in Carbon Nanotubes Probed by Raman and Transport Measurements. *Phys. Rev. Lett.* **2007**, *99*, 136803.

[168] Saito, R.; Jorio, A.; Souza Filho, A. G.; Dresselhaus, G.; Dresselhaus, M. S.; Pimenta, M. A. Probing Phonon Dispersion Relations of Graphite by Double Resonance Raman Scattering. *Phys. Rev. Lett.* **2002**, *88*, 027401.

[169] Jorio, A.; Souza Filho, A. G.; Dresselhaus, G.; Dresselhaus, M. S.; Swan, A. K.; Ünlü, M. S.; Goldberg, B. B.; Pimenta, M. A.; Hafner, J. H.; Lieber, C. M.; Saito, R. G-band resonant Raman study of 62 isolated single-wall carbon nanotubes. *Phys. Rev. B* **2002**, *65*, 155412.

[170] Jorio, A.; Saito, R.; Hafner, J. H.; Lieber, C. M.; Hunter, M.; McClure, T.; Dresselhaus, G.; Dresselhaus, M. S. Structural (n,m) Determination of Isolated Single-Wall Carbon Nanotubes by Resonant Raman Scattering. *Phys. Rev. Lett.* **2001**, *86*, 1118–21.

[171] Maultzsch, J.; Reich, S.; Thomsen, C.; Webster, S.; Czerw, R.; Carroll, D. L.; Vieira, S. M. C.; Birkett, P. R.; Rego, C. A. Raman characterization of boron-doped multiwalled carbon nanotubes. *Appl. Phys. Lett.* **2002**, *81*, 2647–49.

[172] Boyd, R. W., Ed. *Nonlinear Optics*, 1st ed.; Academic Press, 2003.

[173] Joubert, M.-F. Photon avalanche upconversion in rare earth laser materials. *Opt. Mater.* **1999**, *11*, 181–203.

[174] Scheps, R. Upconversion Laser Processes. *Prog. Quant. Electr.* **1996**, *20*, 271–358.

[175] Downing, E.; Hesselink, L.; Ralston, J.; Macfarlane, R. A Three-Color, Solid-State, Three-Dimensional Display. *Science* **1996**, *273*, 1185–89.

[176] Suyver, J. F.; Aebischer, A.; Biner, D.; Gerner, P.; Grimm, J.; Heer, S.; Krämer, K. W.; Reinhard, C.; Güdel, H. U. Novel materials doped with tricalent lanthanides and transition metal ions showing near-infrared to visible photon upconversion. *Opt. Mater.* **2005**, *27*, 1111–30.

[177] Gorris, H. H.; Wolfbeis, O. S. Photon-upconverting nanoparticles for optical encoding and multiplexing of cells, biomolecules, and microspheres. *Angew. Chem. Int. Ed.* **2013**, *52*, 3584–600.

[178] Kumar, R.; Nyk, M.; Ohulchanskyy, T. Y.; Flask, C. A.; Prasad, P. N. Combined Optical and MR Bioimaging Using Rare Earth Ion Doped $NaYF_4$ Nanocrystals. *Adv. Funct. Mater.* **2009**, *19*, 853–59.

[179] Wang, F.; Liu, X. Recent advances in the chemistry of lanthanide-doped upconversion nanocrystals. *Chem. Soc. Rev.* **2009**, *38*, 976–89.

[180] Ye, X.; Collins, J. E.; Kang, Y.; Chen, J.; Chen, D. T. N.; Yodh, A. G.; Murray, C. B. Morphologically controlled synthesis of colloidal upconversion nanophosphors and their shape-directed self-assembly. *Proc. Natl. Acad. Sci. U.S.A.* **2010**, *107*, 22430–35.

[181] Auzel, F.; Pecile, D. Comparison and efficiency of materials for summation of photons assisted by energy transfer. *J. Lumin.* **1973**, *8*, 32–43.

[182] Salley, G. M.; Valienty, R.; Guedel, H. U. Luminescence upconversion mechanism in Yb^{3+}–Tb^{3+} systems. *J. Lumin.* **2001**, *94*, 305–9.

[183] Auzel, F.; Pecile, D. Absolute efficiency for IR to blue conversion materials and theoretical prediction for optimized matrices. *J. Lumin.* **1976**, *11*, 321–30.

[184] Wu, X.; Denis, J. P.; Özen, G.; Pelle, F. Infrared-to-visible conversion luminescence of Tm^{3+} and Yb^{3+} ions in glass ceramics. *J. Lumin.* **1994**, *60*, 212–15.

[185] Chamarro, M. A.; Cases, R. Energy up-conversion in (Yb, Ho) and (Yb, Tm) doped fluorohafnate glasses. *J. Lumin.* **1988**, *42*, 267–74.

[186] Suyver, J. F.; Grimm, J.; Krämer, K. W.; Güdel, H. U. Highly efficient near-infrared to visible up-conversion process in $NaYF_4$:Er^{3+}, Yb^{2+}. *J. Lumin.* **2005**, *114*, 53–59.

[187] Suyver, J. F.; Grimm, J.; van Deen, M. K.; Biner, D.; Krämer, K. W.; Güdel, H. U. Upconversion spectroscopy and properties of $NaYF_4$ doped with Er^{3+}, Tm^{3+} and/or Yb^{3+}. *J. Lumin.* **2006**, *117*, 1–12.

[188] Boyer, J.-C.; Vetrone, F.; Cuccia, L. A.; Capobianco, J. A. Synthesis of colloidal Upconverting $NaYF_4$ Nanocrystals Doped with Er^{3+}, Yb^{3+} and Tm^{3+}, Yb^{3+} via Thermal Decomposition of Lanthanide Trifluoracetate Precursors. *J. Am. Chem. Soc.* **2006**, *128*, 7444–45.

[189] Schäfer, H.; Ptacek, P.; Kömpe, K.; Haase, M. Lanthanide-Doped $NaYF_4$ Nanocrystals in Aqueous Solution Displaying Strong Up-Conversion Emission. *Chem. Mater.* **2007**, *19*, 1396–1400.

[190] Haase, M.; Schäfer, H. Upconverting nanoparticles. *Angew. Chem. Int. Ed.* **2011**, *50*, 5808–29.

[191] Giacovazzo, C.; Monaco, H. L.; Artioli, G.; Viterbo, D.; Ferraris, G.; Gilli, G.; Zanotti, G.; Catti, M. *Fundamentals of Crystallography*, 2nd ed.; Oxford University Press: Oxford, 2002.

[192] Krämer, K. W.; Biner, D.; Frei, G.; Güdel, H. U.; Hehlen, M. P.; Lüthi, S. R. Hexagonal Sodium Yttrium Fluoride Based Green and Blue Emitting Upconversion Phosphors. *Chem. Mater.* **2004**, *16*, 1244–51.

[193] Lissner, F.; Krämer, K.; Mayer, G.; Hu, Z.; Kaindl, G. Die Chloride $Na_{3x}M_{2-x}Cl_6$ (M = La–SM) und NaM_2Cl_6 (M = Nd, Sm): Derivate des UCl_3-Typs. Synthese, Kristallstruktur und Röntgenabsorptionsspektroskopie (XANES). *Z. anorg. allg. Chem.* **1994**, *620*, 444–50.

[194] Auzel, F. Upconversion and anti-Stokes processes with f and d ions in solids. *Chem. Rev.* **2004**, *104*, 139–73.

[195] Chivian, J. S.; Case, W. E.; Eden, D. D. The Photon avalanche: A new phenomenon in Pr_3^+-based infrared quantum counters. *Appl. Phys. Lett.* **1979**, *35*, 124–25.

[196] Case, W. E.; Koch, M. E.; Kueny, A. W. The photon avalanche in rare-earth crystals. *J. Lumin.* **1990**, *45*, 351–53.

[197] Stouwdam, J. W.; van Veggel, F. C. J. M. Near-infrared Emission of Redispersible Er^{3+}, Nd^{3+}, and Ho^{3+} Doped LaF_3 Nanoparticles. *Nano Lett.* **2002**, *2*, 733–37.

[198] Chen, X.; Ma, E.; Liu, G. Energy Levels and Optical Spectroscopy of Er^{3+} in Gd_2O_3 Nanocrystals. *J. Phys. Chem. C* **2007**, *111*, 10404–11.

[199] Wang, F.; Liu, X. Upconversion Multicolor Fine-Tuning: Visible to Near-Infrared Emission from Lanthanide-Doped $NaYF_4$ Nanoparticles. *J. Am. Chem. Soc.* **2008**, *130*, 5642–43.

[200] Wu, S.; Han, G.; Milliron, D. J.; Aloni, S.; Altoe, V.; Talapin, D. V.; Cohen, B. E.; Shuck, P. J. Non-blinking and photostable upconverted luminescence from single lanthanide-doped nanocrystals. *Proc. Natl. Acad. Sci. U.S.A.* **2009**, *106*, 10917–21.

[201] Park, Y. I.; Kim, J. H.; Lee, K. T.; Jeon, K.-S.; Na, H. B.; Yu, J. H.; Kim, H. M.; Lee, N.; Choi, S. H.; Baik, S.-I.; Kim, H.; Park, S. P.; Park, B.-J.; Kim, Y. W.; Lee, S. H.; Yoon, S.-Y.; Song, I. C.; Moon, W. K.; Suh, Y. D.; Hyeon, T. Nonblinking and Nonbleaching Upconverting Nanoparticles as an Optical Imaging Nanoprobe and T1 Magnetic Resonance Imaging Contrast Agent. *Adv. Mater.* **2009**, *21*, 4467–71.

[202] Meschede, D. *Optik, Licht und Laser*, 2nd ed.; Teubner, 2005.

[203] Lauterborn, W.; Kurz, T.; Wiesenfeldt, M. *Kohärente Optik - Grundlagen für Physiker und Ingenieure*, 1st ed.; Springer, 1993.

[204] Mollet, O.; Huant, S.; Drezet, A. Scanning plasmonic microscopy by image reconstruction from the Fourier space. *Opt. Express* **2012**, *20*, 28923–28.

[205] Egerton, R. F., Ed. *Physical Principles of Electron Microscopy*, 1st ed.; Springer US, 2013.

[206] Orfanidis, S. J., Ed. *Optimum Signal processing*, 2nd ed.; http://eceweb1.rutgers.edu/ orfanidi/osp2e/, 2007.

[207] Hafner, J. H.; Bronikowski, M. J.; Azamian, B. R.; Nikolaev, P.; Rinzler, A. G.; Colbert, D. T.; Smith, K. A.; Smalley, R. E. Catalytic growth of single-wall carbon nanotubes from metal particles. *Chem. Phys. Lett.* **1998**, *296*, 195–202.

[208] Kitiyanan, B.; Alvarez, W. E.; Harwell, J. H.; Resasco, D. E. Controlled production of single-wall carbon nanotubes by catalytic decomposition of CO on bimetallic Co-Mo catalysts. *Chem. Phys. Lett.* **2000**, *317*, 497–503.

[209] Iijima, S.; Ichihashi, T. Single-shell carbon nanotubes of 1-nm diameter. *Nature* **1993**, *363*, 603–5.

[210] Bethune, D. S.; Kiang, C. H.; de Vries, M. S.; Gorman, G.; Savoy, R.; Vazquez, J.; Beyers, R. Cobalt-catalysed growth of carbon nanotubes with single-atomic-layer walls. *Nature* **1993**, *363*, 605–7.

[211] Prasek, J.; Drbohlavova, J.; Chomoucka, J.; Hubalek, J.; Jasek, O.; Adam, V.; Kizek, R. Methods for carbon nanotube synthesis - review. *J. Mater. Chem.* **2011**, *21*, 15872–84.

[212] Choi, J. H.; Strano, M. S. Solvatochromism in single-walled carbon nanotubes. *Appl. Phys. Lett.* **2007**, *90*, 223114.

[213] Duque, J. G.; Pasquali, M.; Cognet, L.; Lounis, B. Environmental and Synthesis-Dependent Luminescence Properties of Individual Single-Walled Carbon Nanotubes. *ACS Nano* **2009**, *3*, 2153–6.

[214] Moore, V. C.; Strano, M. S.; Haroz, E. H.; Hauge, R. H.; Smalley, R. E. Individually Suspended Single-Walled Carbon nanotubes in Various Surfactants. *Nano Lett.* **2003**, *3*, 1379–82.

[215] Sun, Y.; Yin, Y.; Mayers, B. T.; Herricks, T.; Xia, Y. Uniform Silver Nanowires Synthesis by Redusing $AgNO_3$ with Ethylene Glycol in the Presence of Seeds and Poly(Vinyl Pyrrolidone). *Chem. Mater.* **2002**, *14*, 4736–45.

[216] Olejnik, M.; Krajnik, B.; Kowalska, D.; Twardowska, M.; Czechowski, N.; Hofmann, E.; Mackowski, S. Imaging of fluorescence enhancement in photosynthetic complexes coupled to silver nanowires. *Appl. Phys. Lett.* **2013**, *102*, 083703.

[217] Olejnik, M.; Twardowska, M.; Zaleszczyk, W.; Mackowski, S. Bioconjugation of Silver Nanowires with Photosynthetic Light-Harvesting Complexes. *Act. Phys. Pol. A* **2012**, *122*, 357–60.

[218] Zhang, Y.-W.; Sun, X.; Si, R.; You, L.-P.; Yan, C.-H. Single-Crystalline and Monodisperse LaF_3 Triangular Nanoplates from a Single-Source Precursor. *J. Am. Chem. Soc.* **2005**, *127*, 3260–1.

[219] Ehlert, O.; Thomann, R.; Darbandi, M.; Nann, T. A Four-Color Colloidal Multiplexing Nanoparticle System. *ACS Nano* **2008**, *2*, 120–4.

[220] Schuller, J. A.; Barnard, E. S.; Cai, W.; Jun, Y. C.; White, J. S.; Brongersma, M. L. Plasmonics for extreme light concentration and manipulation. *Nat. Mater.* **2010**, *9*, 193–204.

[221] Hohenau, A.; Krenn, J. R.; Stepanov, A. L.; Drezet, A.; Ditlbacher, H.; Steinberger, B.; Leitner, A.; Aussenegg, F. R. Dielectric optical elements for surface plasmons. *Opt. Lett.* **2005**, *30*, 893–95.

[222] Freitag, M.; Chen, J.; Tersoff, J.; Tsang, J. C.; Fu, Q.; Liu, J.; Avouris, P. Mobile Ambipolar Domain in Carbon-Nanotube Infrared Emitters. *Phys. Rev. lett.* **2004**, *93*, 076803.

[223] Avouris, P.; Freitag, M.; Perebeinos, V. Carbon-nanotube photonics and optoelectronics. *Nature Photon.* **2008**, *2*, 341–50.

[224] Vasilev, K.; Knoll, W.; Kreiter, M. Fluorescence intensites of chromophores in front of a thin metal film. *J. Chem. Phys.* **2004**, *120*, 3439–45.

[225] Hennrich, F.; Krupke, R.; Arnold, K.; Rojas Stütz, J. A. R.; Lebedkin, S.; Koch, T.; Schimmel, T.; Kappes, M. M. The Mechanism of Cavitation-Induced Scission of Single-Walled Carbon Nanotubes. *J. Phys. Chem. B* **2007**, *111*, 1932–37.

[226] Casey, J. P.; Bachilo, S. M.; Moran, C. H.; Weisman, R. B. Chirality-Resolved Length Analysis of Single-Walled Carbon Nanotube Samples through Shear-Aligned Photoluminescence Anisotropy. *ACS Nano* **2008**, *2*, 1738–46.

[227] Chew, H. B.; Moon, M.-W.; Lee, K. R.; Kim, K.-S. Compressive dynamic scission of carbon nanotubes under sonication: fracture by atomic ejection. *Proc. R. Soc. A* **2010**, *467*, 1270–89.

[228] Drezet, A.; Hohenau, A.; Koller, D.; Stepanov, A.; Ditlbacher, H.; Steinberger, B.; Aussenegg, F. R.; Leitner, A.; Krenn, J. R. Leakage radiation microscopy of surface plasmon polaritons. *Materials Science and Engineering: B* **2008**, *149*, 220–29.

[229] Drezet, A.; Hohenau, A.; Stepanov, A. L.; Ditlbacher, H.; Steinberger, B.; Galler, N.; Aussenegg, F. R.; Leitner, A.; Krenn, J. R. How to erase surface plasmon fringes. *Appl. Phys. Lett.* **2006**, *89*, 091117.

[230] Colas des Francs, G.; Grandidier, J.; Massenot, S.; Bouhelier, A.; Weeber, J.-C.; Dereux, A. Integrated plasmonic waveguides: A mode solver based on density of states formulation. *Phys. Rev. B* **2009**, *80*, 115419.

[231] Arnoldus, H. F.; Foley, J. T. Transmission of dipole radiation through interfaces and the phenomenon of anti-critical angles. *J. Opt. Soc. Am. A* **2004**, *21*, 1109–17.

[232] Kolomenski, A.; Kolomenskii, A.; Noel, J.; Peng, S.; Schuessler, H. Propagation length of surface plasmons in a metal film with roughness. *Appl. Opt.* **2009**, *48*, 5683–91.

[233] Braundmeier, A.; Arakawa, E. Effect of surface roughness on surface plasmon resonance absorption. *J. Phys. Chem. Solids* **1974**, *35*, 517–20.

[234] Kapitza, H. Influence of surface roughness on the reflection of gold films in the region of surface plasmon excitation. *Opt. Commun.* **1976**, *16*, 73–75.

[235] Chang, D. E.; Sørensen, A. S.; Hemmer, P. R.; Lukin, M. D. Strong coupling of single emitters to surface plasmons. *Phys. Rev. B* **2007**, *76*, 035420.

[236] Novotny, L. Strong coupling, energy splitting, and level crossings: A classical perspective. *Am. J. Phys.* **2010**, *78*, 1199–1202.

[237] Kuzyk, A.; Pettersson, M.; Toppari, J. J.; Hakala, T. K.; Tikkanen, H.; Kunttu, H.; Törmä, P. Molecular coupling of light with plasmonic waveguides. *Opt. Express* **2007**, *15*, 9908–17.

[238] Wang, Y.; Liu, X.; Whitmore, D.; Xing, W.; Potma, E. O. Remote multi-color excitation using femtosecond propagating surface plasmon polaritons in gold films. *Opt. Express* **2011**, *19*, 13454–63.

[239] Wei, H.; Ratchford, D.; Li, X. E.; Xu, H.; Shih, C.-K. Propagating Surface Plasmon Induced Photon Emission from Quantum Dots. *Nano Lett.* **2009**, *9*, 4168–71.

[240] Van Labeke, D.; Baida, F.; Barchiesi, D.; Courjon, D. A theoretical model for the Inverse Scanning Tunneling Optical Microscope (ISTOM). *Opt. Commun.* **1995**, *114*, 470–80.

[241] Van Labeke, D.; Baida, F. I.; Vigoureux, J.-M. A theoretical study of near-field detection and exciation of surface plasmons. *Ultramicroscopy* **1998**, *71*, 351–59.

[242] Bouwkamp, C. Diffraction Theory. *Rep.Prog. Phys.* **1954**, *17*, 35–100.

[243] Hecht, B.; Sick, B.; Wild, U. P.; Deckert, V.; Zenobi, R.; Martin, O. J. F.; Pohl, D. W. Scanning near-field optical microscopy with aperture probes: fundamentals and applications. *J. Chem. Phys.* **2000**, *112*, 7761–74.

[244] Van Labeke, D.; Barchiesi, D.; Baida, F. Optical characterization of nanosources used in scanning near-field optical microscopy. *J. Opt. Soc. Am. A* **1995**, *12*, 695–703.

[245] Novotny, L.; Beversluis, M. R.; Youngworth, K. S.; Brown, T. G. Longitudinal Field Modes Probed by Single Molecules. *Phys. Rev. Lett.* **2001**, *86*, 5251–54.

[246] Georgi, C.; Hartmann, N.; Gokus, T.; Green, A. A.; Hersam, M. C.; Hartschuh, A. Photoinduced luminescence blinking and bleaching in individual single-walled carbon nanotubes. *ChemPhysChem* **2008**, *9*, 1460–64.

[247] Veerman, J. A.; Garcia-Parajo, M. F.; Kuipers, L.; Van Hulst, N. F. Single molecule mapping of the optical field distribution of probes for near-field microscopy. *J. Microsc.* **1999**, *194*, 477–82.

[248] Pyayt, A. L.; Wiley, B.; Xia, Y.; Chen, A.; Dalton, L. Integration of photonic and silver nanowire plasmonic waveguides. *Nat. Nanotechnol.* **2008**, *3*, 660–65.

[249] Davies, M.; Wochnik, A.; Feil, F.; Jung, C.; Bräuchle, C.; Scheu, C.; Michaelis, J. Synchronous Emission from Nanometric Silver Particles through Plasmonic Coupling on Silver Nanowires. *ACS Nano* **2012**, *6*, 6049–57.

[250] Fang, Y.; Li, Z.; Huang, Y.; Zhang, S.; Nordlander, P.; Halas, N. J.; Xu, H. Branched Silver Nanowires as Controllable Plasmon Routers. *Nano Lett.* **2010**, *10*, 1950–54.

[251] Wei, H.; Li, Z.; Tian, X.; Wang, Z.; Cong, F.; Liu, N.; Zhang, S.; Nordlander, P.; Halas, N. J.; Xu, H. Quantum Dot-Based Local Field Imaging Reveals Plasmon-Based Interferometric Logic in Silver Nanowire Networks. *Nano Lett.* **2011**, *11*, 471–75.

[252] Wei, H.; Wang, Z.; Tian, X.; Käll, M.; Xu, H. Cascaded logic gates in nanophotonic plasmon networks. *Nat. Commun.* **2011**, *2*, 387.

[253] Dickson, R. M.; Lyon, L. A. Unidirectional Plasmon Propagation in Metallic Nanowires. *J. Phys. Chem. B* **2000**, *104*, 6095–98.

[254] Falk, A. L.; Koppens, F. H. L.; Yu, C. L.; Kang, K.; Snapp, N. d.-L.; Akimov, A. V.; Jo, M.-H.; Lukin, M. D.; Park, H. Near-field electrical detection of optical plasmons and single-plasmon sources. *Nat. Phys.* **2009**, *5*, 475–79.

[255] Zhang, D. G.; Yuan, X.-C.; Bouhelier, A.; Wang, P.; Ming, H. Excitation of surface plasmon polaritons guided mode by Rhoadmine B molecules doped in a PMMA stripe. *Opt. Lett.* **2010**, *35*, 408–10.

[256] Massenot, S.; Grandidier, J.; Bouhelier, A.; Colas des Francs, G.; Markey, L.; Renger, J.; Gonzalez, M. U.; Quidant, R. Polymer-metal waveguides characterization by Fourier plane leakage radiation microscopy. *Appl. Phys. Lett.* **2007**, *91*, 243102.

[257] Holgersson, S.; Sedström, E. Experimentelle Untersuchungen über die Gitterstruktur einiger Metallegierungen. *Ann. Phys.* **1924**, *380*, 143–62.

[258] Wyckoff, R. W. G., Ed. *Crystal Structures*, 2nd ed.; Interscience Publishers, 1963; Vol. 1.

[259] Korte, K. E.; Skrabalak, S. E.; Xia, Y. Rapid synthesis of silver nanowires through a CuCl- or $CuCl_2$-mediated polyol process. *J. Mat. Chem.* **2008**, *18*, 437–41.

[260] Davey, W. P. Precision Measurements of the Lattics Constants of Twelve Common Metals. *Phys. Rev.* **1925**, *25*, 753–61.

[261] Bearden, J. X-Ray Wavelengths. *Rev. Mod. Phys.* **1967**, *39*, 78–127.

[262] Krause, M. O.; Oliver, J. H. Natural Widths of Atomic K and L Levels, $K\alpha$ X-Ray Lines and Several KLL Auger Lines. *J. Phys. Chem. Ref. Data* **1979**, *8*, 329–38.

[263] Curto, A. G.; Volpe, G.; Taminiau, T. H.; Kreuzer, M. P.; Quidant, R.; van Hulst, N. F. Unidirectional Emission of a Quantum Dot Coupled to a Nanoantenna. *Science* **2010**, *329*, 930–33.

[264] Dorfmüller, J.; Vogelgesang, R.; Khunsin, W.; Rockstuhl, C.; Etrich, C.; Kern, K. Plasmonic Nanowire Antennas: Experiment, Simulation, and Theory. *Nano Lett.* **2010**, *10*, 3596–603.

[265] Encina, E. R.; Coronado, E. A. Plasmonic Nanoantennas: Angular Scattering Properties of Multipole Resonances in Noble Metal Nanorods. *J. Phys. Chem. C* **2008**, *112*, 9586–94.

[266] Butz, T., Ed. *Fouriertransformation für Fußgänger*, 6th ed.; Vieweg+Teubner, 2009.

[267] Li, Q.; Qiu, M. Plasmonic wave propagation in silver nanowires: guiding modes or not? *Opt. Express* **2013**, *21*, 8587–95.

[268] Rai, P.; Hartmann, N.; Berthelot, J.; Colas-des Francs, G.; Hartschuh, A.; Bouhelier, A. In-plane remote photoluminescence excitation of carbon notube by propagating surface plasmon. *Opt. Lett.* **2012**, *37*, 4711–13.

[269] Zhu, W.; Wang, D.; Crozier, K. B. Direct Observation of Beamed Raman Scattering. *Nano Lett.* **2012**, *12*, 6235–43.

[270] Taminiau, T. H.; Karaveli, S.; van Hulst, N. F.; Zia, R. Quantifying the magnetic nature of light emission. *Nature Commun.* **2012**, *3*, 979.

[271] Karaveli, S.; Wang, S.; Xiao, G.; Zia, R. Time-Resolved Energy-Momentum Spectroscopy of Electric and Magnetic Dipole Transitions in Cr^{3+}:MgO. *ACS Nano* **2013**, *7*, 7165–72.

[272] Bonnand, C.; Bellessa, J.; Plenet, J. C. Properties of surface plasmons strongly coupled to excitons in an organic semiconductor near a metallic surface. *Phys. Rev. B* **2006**, *73*, 245330.

[273] Berrier, A.; Cools, R.; Arnold, C.; Offermans, P.; Crego-Calama, M.; Brongersma, S. H.; Gomez-Rivas, J. Active Control of the Strong Coupling Regime between Porphyrin Excitons and Surface Plasmon Polaritons. *ACS Nano* **2011**, *5*, 6226–32.

Acronyms

1D	one-dimensional
3D	three-dimensional
AFM	atomic force microscopy
APD	avalanche photo diode
ATR	attenuated total reflection
BFP	back focal plane
CCD	charge coupled device
ccp	cubic closest packing
CoMoCat	cobalt-molybdenum catalyst
EDX	energy-dispersive X-Ray
EELS	electron energy loss spectroscopy
ESA	excited state absorption
ETU	energy transfer upconversion
fcc	face centered cubic
FET	field effect transistor
FWHM	full width at half maximum
GSA	ground state absorption
HiPCO	high pressure carbon monoxide
IR	infrared

LED . . . . . light emitting diode

LSPP . . . . . localized surface plasmon polariton

NA . . . . . numerical aperture

NC . . . . . nanocrystal

NIR . . . . . near infrared

NW . . . . . nanowire

OLED . . . . . organic light emitting diode

PA . . . . . photon avalanche

PI . . . . . proportional-integral

PL . . . . . photoluminescence

PLL . . . . . phase-locked-loop

PSTM . . . . . photon scanning tunneling microscopy

PVP . . . . . polyvinylpyrrolidone

RBM . . . . . radial breathing mode

SC . . . . . sodium cholate

SDC . . . . . sodium deoxycholate

SDS . . . . . sodium dodecyl sulfate

SEM . . . . . scanning electron microscopy

SNOM . . . . . scanning near-field optical microscopy

SP . . . . . surface plasmon

SPCE . . . . . surface plasmon coupled emission

SPM . . . . . scanning probe microscopy

SPP . . . . . surface plasmon polariton

STM . . . . . scanning tunneling microscopy

STOM . . . . . scanning tunneling optical microscopy

SWCNT . . . . . single-walled carbon nanotube

TEM . . . . . transmission electron microscopy

TFA . . . . . tri fluor acetate

TM . . . . . transvere magnetic

UC . . . . . upconversion

VIS . . . . . visible

List of Figures

2.1 (a) Schematic of the charges and electromagnetic field lines of a SPP propagating on a metal/dielectric interface. (b) shows the exponential dependence of the field amplitude $|E_z|$ in the direction of z into the two different media. . . 6

2.2 Real part of SPP dispersion relation for a silver/air interface 7

2.3 Schematic of a metal/dielectric multilayer system considered for the calculation of the SPP dispersion relation in eq. 2.7 8

2.4 (a) SPP dispersion relations comparing the solution for a gold/air interface with the multilayer solutions for different glass coating thicknesses d_2. (b) Correlation of the real part of the plasmon wave-vector k'_{SPP} with the thicknesses of the metal film d_1 and the glass coating d_2. 10

2.5 (a) Calculated propagation length L_{D} over a range of wavelengths/frequencies for silver, gold and copper. (b) Dependency of the propagation length L_{D} at 1000 nm on the thickness of a gold film d_1 and the thickness of a glass cover layer ($\varepsilon_2 = 1.5^2$) d_2. 11

2.6 Schematic of the metal wire used for the calculation of the dispersion relation in eq. 2.19. 12

2.7 Comparison of SPP dispersion relations calculated for a silver/air interface, a multilayer system and a nanowire with the same metal thicknesses. 13

2.8 Illustration of the SPP dispersion for a silver/air interface, the light line k_0, the dispersion for light in glass k_{glass} and the maximum dispersion accessible with a high numerical oil immersion objective k_{max}. 14

2.9 SPP excitation schemes 15

2.10 ATR measurements in the (a) Otto and (b) Kretschmann configuration for different air gap sizes and gold film thicknesses. 16

2.11 Schematic of leakage radiation emission from a propagating SPP on a metal film into the substrate 18

2.12 Schematic of SPP detection via PSTM/STOM 19

3.1 (a) Schematic of radiated power by an emitter on an interface into different angular zones. (b) Schematic of the projection of angular emission by an imaging lens onto the BFP. 22

3.2 Schematic of the geometry used for the calculation of Fourier patterns from dipoles on an interface. 23

3.3 Calculated BFP patterns for dipoles on a glass/air interface with different orientations. . . . 25
3.4 Plot of the detection efficiency γ for an in-plane and a vertical dipole, as well as randomly oriented dipoles on a glass substrate detected with an index matched oil immersion microscope objective. . . . 26
3.5 (a) Reflection BFP pattern from a 20 nm gold film coated with 20 nm SiO_x and excited at 900 nm. (b) Cross section through the reflection pattern. . . . 27
3.6 (a) Schematic of a single dipole chain connected with a phase for the simulation of SPP propagation along a plasmonic nanowire. (b) Calculated BFP pattern for NW with a diameter of 50 nm and (c) 100 nm. . . . 28

4.1 Schematic of the unit cell in the graphene lattice for the three different types of SWCNTs. . . . 32
4.2 Schematic of the band structure of SWCNTs illustrating the different transitions polarized parallel (a) and perpendicular (b) to the nanotube axis. . . . 33
4.3 (a) PL spectra from three different individual nanotubes after optical excitation at 565 nm. (b) Combined Raman and PL spectrum from a (6,4) SWCNT. . . . 35
4.4 Crystal structure of (a) cubic α-$NaYF_4$ and hexagonal β-$NaYF_4$. . . . 36
4.5 Energy diagram of a simplified three level system to visualize three possible UC mechanisms:(a) ESA, (b) ETU and (c) PA. . . . 37
4.6 Energy diagram for ytterbium and erbium and the involved excitation, energy transfer and emission processes. . . . 38

5.1 Schematic of the optical setup. (a) Real-space imaging, scanning confocal detection and spectroscopy. (b) Fourier (BFP) imaging. . . . 42
5.2 Schematic of the beam path in order to image the BFP of a microscope objective. 43
5.3 Schematic of the aperture SNOM configuration . . . 44
5.4 (a) SEM micrograph of silver NWs. The scale bar represents 10 µm. (b). Detailed SEM micrograph of two silver NWs. The scale bar represents 100 nm. 47
5.5 Emission spectrum of $NaYF_4$ doped with 20 wt% yttrium and 2 wt% erbium. . 47

6.1 Confocal PL image of single SWCNTs together with corresponding Fourier space and real space images. . . . 50
6.2 Confocal PL images of SWCNTs on a dielectric/gold substrate for different excitation polarizations with the corresponding BFP patterns. . . . 51
6.3 Correlation between confocal SWCNT PL position (a), nanotube orientation from AFM topography (b) and corresponding BFP patterns (c), (d). . . . 52
6.4 Schematic of the sample geometry and coordinate system for the calculation of real and Fourier space images from a SWCNT single dipole situated on a spacer/gold film. . . . 53
6.5 Comparison of the modulus square of the numerical Fourier transform of the asymptotic plasmon field and a Lorentzian line shape function. . . . 54

6.6 Experimental (a) and theoretical (b) real space image rendered by a single in-plane dipole and dected by the CCD camera. The scale bar represents 4.0 µm in both images. 55
6.7 (a) Experimentally obtained Fourier plane pattern. (b) Fit of (a) according to eq. 6.2. (c) Residuum after subtraction (b)-(a) 56
6.8 Results for the plasmon emission angle θ_{SPP} (a) and the propagation length L_{S} (b) obtained from fitted SWCNT BFP patterns on spacer layers with different thicknesses d_2 together with theoretical values calculated according to eq. 2.9. . 56
6.9 Comparison between experimentally obtained and calculated Fourier patterns with different polarizations for a SWCNT deposited on glass and ona 25 nm gold film. 58

7.1 Real space and corresponding BFP patterns for an aperture probe 4 µm away from a 20 nm gold film (a), (b) and approached close to several nm (c), (d) to the surface. 62
7.2 (a),(c) real space images and (b),(d) BFP patterns for SPPs launched by an aperture probe, recorded with two different input polarizations. 63
7.3 Emission maps from a single SWCNT during an aperture probe scan for two different input polarizations (a) and (b) together with a BFP pattern of the same nanotube after confocal excitation. 65
7.4 Schematic of the multilayer sample system which is used for the calculations of the fields emitted by an aperture tip. 67
7.5 Calculated (a) intensity and (b) in-plane polarization for the field created in the metal air interface of a 20 nm gold film by the emission of an aperture probe . 68
7.6 Comparison between an experimental and calculated intensity profiles for the I_z and I_{xy} component of the field, emitted by an aperture probe. 69

8.1 (a) Overview and (b) magnified TEM images from a representative silver nanowire. (c) shows a electron diffraction pattern measured on the NW. 73
8.2 EDX spectra from the silver nanowire in fig. 8.1 (b) taken on the wire (black solid line, position I) and on the polymer layer (red dotted line, position II) divided into two energy ranges (a) and (b). 74
8.3 Distribution of (a) nanowire diameters D_{wire} and (b) polymer thicknesses d_{PVP} from 77 different silver NWs measured from TEM images. 74
8.4 (a) Confocal PL map of a representative sample area together with the corresponding topography data in (b) from silver NWs decorated with rare earth doped NC. 75
8.5 Back-focal plane PL emission pattern detected for a nanocrystal on glass. . . . 76
8.6 (a) Confocal PL map of a wire decorated with nanocrystals, together with corresponding BFP patterns recorded at different positions along the NW. . . . 76
8.7 (a) Schematic of the BFP imaging for randomly oriented dipoles together with an experimental (b) and a modeled BFP pattern. 78

8.8 Schematic of the formation of a BFP pattern for the leaky antenna resonator as described in eq. 8.7. 80
8.9 map of profiles through theoretical BFP pattern I_{NW} along the propagation direction $k_{\parallel}$ in dependency of the excitation position a, together with four complete calculated pattern for different excitation positions. 81
8.10 Calculated plasmon dispersion $k_{\mathrm{SPP}}(\omega)$ for a silver NW and the maximum detectable k-vector by a NA = 1.4 objective $k_{\mathrm{max}}(\omega)$ together with an underlying $\mathrm{sinc}\left(k_{\parallel}\right)$ pattern due to the finite emitter length. 82
8.11 (a)-(c) Experimentally obtained BFP patterns from a NW excited at three different positions together with best fit patterns (d)-(f) calculated according to eq. 8.11. 83
8.12 (a) Plot of the length extracted from the fringe distance in the BFP patterns L_{BFP} against the physical length measured by AFM L_{AFM} on the same nanowire. (b) The fitted k'_{SPP} is plotted against the thickness for each corresponding wire. 84

List of Publications

The following peer-reviewed papers have been published during the course of my PhD research and further activities:

N. Hartmann, F. Tantussi, G. Colas-des-Francs, A. Guggenmos, U. Kleineberg, A. Bouhelier, F. Fuso, M. Allegrini, A. Hartschuh "Mapping of propagating surface plasmons launched by a scanning source with single carbon nanotubes", **2013**, in preparation.

D. Piatkowski, N. Hartmann, M. Nyk, M. Olejnik, T. Mancabelli, S. Mackowski, A. Hartschuh "Silver Nanowires as Receiving-Radiating Antennas in Plasmon Enhanced Up-Conversion Processes", **2013**, in preparation

M. Handloser, T. Winzer, G. Piredda, N. Hartmann, A. Lombardo, A. Guggenmoos, R. Ciesielski, A. Comin, U. Kleineberg, A. C. Ferrari, E. Malic, A. Hartschuh "Controlling the coupled coherence and population dynamics in graphene using chirped laser pulses", **2013** in preparation.

N. Mauser, N. Hartmann, M. Hoffmann, J. Janik, A. Högele, A. Hartschuh, "Antenna-enhanced Optoelectronic Probing of Carbon Nanotubes", *Nature Commun.* **2013**, submitted

N. Hartmann, D. Piatkowski, R. Ciesielski, S. Mackowski, A. Hartschuh, "Radiation Channels Close to a Plasmonic Nanowire Visualized by Back Focal Plane Imaging", *ACS Nano* **2013**, *7*, 10257.

P. Rai, N. Hartmann, J. Berthelot, J. Arocas, G. Colas des Francs, A. Hartschuh, A. Bouhelier, "Electrical exciation of surface plasmons by an individual carbon nanotube transistor", *Phys. Rev. Lett.* **2013**, *111*, 026804.

P. Rai, N. Hartmann, J. Berthelot, G. Colas des Francs, A. Hartschuh, A. Bouhelier, "In-plane remote photoluminescence excitation of carbon nanotube by propagating surface plasmon", *Opt. Lett.* **2012**, *37*, 4711.

N. Hartmann, G. Piredda, J. Berthelot, G. Colas des Francs, A. Bouhelier, A. Hartschuh, "Launching Propagating Surface Plasmon Polaritons by a Single Carbon Nanotube Dipolar Emitter", *Nano Lett.* **2012**, *12*, 177.

M. Böhmler, N. Hartmann, C. Georgi, F. Hennrich, M. C. Hersam, A. Hartschuh, "Enhancing and Redirecting Carbon Nanotube Photoluminescence by an Optical Antenna", *Opt. Express* **2010**, *18*, 16443.

R. Appel, N. Hartmann, H. Mayr,"Scope and Limitations of Cyclopropanations with Sulfur Ylides", *J. Am. Chem. Soc.* **2010**, *132*, 17894.

H. Qian, P. T. Araujo, C. Georgi, T. Gokus, N. Hartmann, A. A. Green, A. Jorio, M. C. Hersam, L. Novotny, A. Hartschuh, "Visualizing the Local Optical Response of Semiconducting Carbon Nanotubes to DNA-wrapping", *Nano Lett.* **2008**, *8*, 2706.

C. Georgi, N. Hartmann, T. Gokus, A. A. Green, M. C. Hersam, A. Hartschuh, "Photo-induced luminescence blinking and bleaching in individual Single-Walled Carbon Nanotubes", *ChemPhysChem* **2008**, *9*, 1460.

List of Conferences

NFO12, San Sebastian (Spain), 03.09 - 06.09.2012
Poster: Coupling between excitons in carbon nanotubes and propagating surface plasmons

HBSM12, Tübingen (Germany), 27.08 - 30.08.2012
Poster: Coupling of Excitons in Carbon Nanotubes to Propagating Surface Plasmons

DPG Frühjahrstagung 2012, Berlin (Germany), 26.03. - 30.03.2012
Oral presentation: Coupling of Excitons in Carbon Nanotubes to Propagating Surface Plasmons

ANAP Meeting, Sønderborg (Denmark), 01.09 - 02.09.2011
Oral presentation: Exciting Surface Plasmons by Carbon Nanotube Photoluminescence

CRANN, Dublin (Ireland), 07.06.2011
Poster: Interfacing carbon nanotube photoluminescence to a plasmonic architecture

SPP5, Busan (South Korea), 15.05 - 20.05.2011
Oral presentation: Launching Surface Plasmons by Carbon Nanotube Photoluminescence

DPG Frühjahrstagung 2011, Dresden (Germany), 13.03. - 18.03.2011
Oral presentation: Launching Surface Plasmons by Carbon Nanotube Photoluminescence

Workshop on Carbon Nanotube Optics 2010, Niederstetten (Germany), 07.10. - 10.10.2010
Poster: Coupling of SWNT Photoluminescence to Surface Plasmons in Metallic Antennas and Metallic Thin Films

NFO11, Beijing (PR China), 29.08. - 02.09.2010
Poster: Coupling of Carbon Nanotube Photoluminescence to Surface Plasmons in Metallic Antennas and Metallic Thin Films

EMRS 2010 Spring Meeting, Strasbourg (France), 07.06. - 11.06.2010
Poster: Optical Antennas Enhance and Redirect Nanotube Photoluminescence

Workshop on Carbon Nanotube Optics 2009, Kleinwalsertal (Austria), 17.07. - 19.07.2009
Poster: Imaging of radiation patterns from SWNTs on substrates

Acknowledgements

First and foremost I want to thank my doctoral advisor **Prof. Dr. Achim Hartschuh** for giving me the opportunity to work in his group and the continuous support and encouragement. His scientific enthusiasm and his excellent way of explaining always motivated to dive into and explore new fields and ideas. Further, I want to thank him for giving me the opportunity to present the results of my work on various workshops and conferences.

I want to thank **Dr. Alexandre Bouhelier** for his support as the second reviewer of my thesis as well as the great atmosphere and dedication during the joint project E^2-Plas.

I also want to thank **Prof. Dr. Maria Allegrini**, **Dr. Padmabh Rai** and **Dr. Johann Berthelot** for the pleasant time we shared during the joint experiments, discussions and efforts in the E^2-Plas project. In this context my special thanks go out to **Dr. Francesco Tantussi** for the great working atmosphere and effort during the realization of the aperture SNOM SPP excitation and further.

I thank **Dr. Dawid Piatkowski** for the collaboration and the great time during the joint experiment on plasmonic nanowires coupled to rare-earth doped nanocrystals and beyond.

In regards to TEM measurements, I thank **Dr. Angela Wochnik** for her expertise and patience during the analysis of many silver nanowires.

For the supply of excellent gold film samples with added spacer layers I thank **Alexander Guggenmos**.

All former and current group members **Alexandre**, **Alberto**, **Amit**, **Giovanni**, **Harald**, **Hayk**, **Huihong**, **Julia**, **Kevin**, **Matthias**, **Miriam**, **Nina**, **Paulo**, **Richard**, **Tobia**, **Tobias** and **Xian**, I want to thank for the great atmosphere, the friendships, the discussions and activities on and off campus.

A special mention goes to **Dr. Carsten Georgi**. I am very grateful for the time I was allowed to spend with him and learn from his experience and knowledge. My thoughts are with his family and friends.

Besonders möchte ich mich bei meiner **Familie**, meinen Eltern und meiner Schwester für die ständige Unterstützung, Anerkennung und Ermutigungen auf dem gesamten Weg bedanken.

最要感谢的是你，晓文。如果没有你的理解、陪伴和支持，我就不可能顺利地完成这篇论文!